Local magnetometry measurements of selected superconductors

Zuzana Medvecka

Communauté
UNIVERSITÉ Grenoble Alpes

UNIVERZITA PAVLA JOZEFA ŠAFÁRIKA V KOŠICIACH

THÈSE

Pour obtenir le grade de

DOCTEUR DE LA COMMUNAUTE UNIVERSITE GRENOBLE ALPES

préparée dans le cadre d'une cotutelle entre la Communauté Université Grenoble Alpes et Pavol Jozef Šafárik University in Košice

Spécialité : **Physique de matière condensée & rayonnement**

Arrêté ministériel : le 6 janvier 2005 - 7 août 2006

Présentée par

Zuzana MEDVECKÁ

Thèse dirigée par **Thierry KLEIN** et **Zuzana VARGAEŠTOKOVÁ**
préparée au sein des **Institute Néel, Grenoble** et **Centre of Low Temperature Physics, Košice**

Etudes magnétiques locales des supraconducteurs exotiques

Thèse soutenue publiquement le **31.08.2017**
devant le jury composé de :

prof. Ing. Martin ORENDÁČ
Professeur à FS PJŠU, Président
RNDr. Zdeněk JANŮ
Directeur de recherche à FZÚ AV ČR, v. v. i., Rapporteur
doc. RNDr. Martin MOŠKO, DrSc.
Directeur de recherche à IEE SAS, Rapporteur
Dr. Klaus HASSELBACH
Directeur de recherche à UGA, Membre
Dr. Hervé CERCELLIER
Maître de conférences à UGA, Membre
Doc. RNDr. Karol FLACHBART
Directeur de recherche à IEP SAS, Membre

Acknowledgement

In the first place, I would like to thank to both of my supervisors, Zuzana Vargaeštoková and Thierry Klein, for the help and guidance they offered me not just in the work but in the everyday life. Also my big thank you goes to the whole department of Centre of low temperature physics in Košice and the MagSup research group at the Institut Néel in Grenoble. In the last but not the least place, I would like to thank to my friends and family for their support.

Abstrakt

Predmetom tejto práce bolo detailné štúdium supravodivého materiálu Cu_xTiSe_2. Pomocou lokálnej Hallovskej magnetometrie boli študované monokryštály s rôznou koncentráciou medi, od poddopovanej až po predopovanú oblasť fázového diagramu. Ako prvé sme zostrojili profily magnetického poľa, aby bolo možné určiť, kedy preniknú do vzorky prvé supravodivé víry. Výsledný tvar dómu daných profilov indikoval nízky počet záchytných centier vo vzorkách. Ďalšou analýzou týchto profilov sme zistili, že hlavný vplyv na prienik vírov do supravodiča majú geometrické bariéry, čo nám ďalej umožnilo získať hodnoty dolného kritického magnetického poľa H_{c1}. Následne sme určili teplotnú závislosť $H_{c1}(T)$ a našli sme dobrú zhodu s teoretickou krivkou pre dve energetické medzery, napriek tomu, že prítomnosť druhej malej medzery nekoreluje s elektrónovou štruktúrou Cu_xTiSe_2. Pomocou výsledkov meraní tepelnej kapacity, ktoré boli predtým uskutočnené na našich vzorkách, sme z Hallovskej magnetometrie získali závislosť kondenzačnej energie na dopovaní a zistili sme, že má netriviálny priebeh. Navyše, experimenty, ktoré sme robili pri rôznych orientáciách magnetického poľa, odhalili prítomnosť takzvaného lock-in efektu, kedy supravodivé víry ostávajú zachytené pozdĺž smeru vrstevnatej štruktúry aj pre magnetické pole odklonené od tohto smeru. Experimentálne sme určili orientáciu vírov, ktorú sme následne popísali pomocou modelu, ktorý berie do úvahy prítomnosť dodatočnej vrstevnatej štruktúry, kde je supravodivosť aspoň čiastočne potlačená. Lock-in efekt bol analyzovaný v troch rôznych vzorkách. Ukázali sme, že sila lock-in efektu nezávisí od dopovania, aj keď tento efekt môže byť prekrytý silnými demagnetizačnými javmi vo veľmi tenkých vzorkách. Vysoká hodnota sily lock-in efektu zároveň poukazuje na to, že supravodivosť je takmer úplne potlačená na neznámej vrstevnatej štruktúre. Jej pôvod nevychádza z vnútornej štruktúry Cu_xTiSe_2, ale predpokladáme, že by mohol súvisieť s nedávnym objavom prítomnosti doménových stien vo vlnách nábojovej hustoty, ktoré by mohli indukovať priestorové modulovanie supravodivého parametra usporiadania.

Kľúčové slová:
Supravodiče, horné a dolné kritické magnetické pole, supravodivé víry, hallovské senzory, lokálna magnetizácia, susceptibilita, demagnetizačný faktor, magnetický profil vzorky.

Résumé

Le sujet de ce travail a été une étude détaillée du supraconducteur Cu_xTiSe_2. Des échantillons avec différentes teneurs en cuivre x, ont été étudiés par magnétométrie locale à sonde de Hall. Nous avons tout d'abord construit les profils de champ magnétique dans les échantillons pour déterminer quand les premiers vortex pénètrent dans l'échantillon. La forme en dôme des profils a indiqué que le piègeage est très faible et que la pénétration des vortex est principalement régie par des barrières géométriques, ce qui nous a permis de déterminer le champ critique inférieur, H_{c1}. Un bon accord entre la théorie et $H_{c1}(T)$ a été obtenu en utilisant un modèle à deux gaps, même si l'origine du plus petit de ces gaps ne peutêtre liée à la structure électronique de Cu_xTiSe_2. En combinant ces mesures avec des mesures de chaleur spécifique effectuées précédemment sur ces échantillons, nous avons obtenu un comportement non trivial de l'énergie de condensation. En outre, les mesures effectuées pour diverses orientations du champ magnétique ont révélé la présence d'un effet de "lock-in" dans Cu_xTiSe_2, montrant que les vortex restent piégés le long d'une structure en couches même pour les champs magnétiques inclinés. L'orientation des vortices a été déterminée expérimentalement et a pu être bien décrite par un modèle tenant compte de la présence d'une "sur-structure" dans laquelle la supraconductivité est - au moins - partiellement détruite. Cet effet de lock-n a été analysé sur trois échantillons et nous avons montré que la force de piégeage est indépendante du dopage du cuivre. La nature de cette sur-structure est encore inconnue mais pourrait être liée à l'observation récente de parois de domaine des ondes de densité de charge, qui pourraient induire de fortes variations du paramètre d'ordre supraconducteur.

Mots clés:

Superconducteurs, sondes de Hall, le champ critiques inférieur et supérieur

Abstract

The subject of this work was a detailed study of superconducting Cu_xTiSe_2. Samples with various copper content x, from underdoped to overdoped regions of the phase diagram, were investigated by local Hall probe magnetometry. At first, we constructed the magnetic field profiles in the samples to determine when the first vortices penetrate into the sample. The observed dome-like shape of the profiles indicated that pinning is very small and that the vortex penetration is primarily governed by geometrical barriers, hence enabling us to determine the lower critical field, H_{c1}. A good agreement between theory and the $H_{c1}(T)$ data was obtained by using a model with two energy gaps, even though the origin of the smaller energy gap in Cu_xTiSe_2 cannot be related to its electronic structure. Combining those measurements with heat capacity measurements previously performed on these samples, we obtained a non trivial condensation energy. Moreover, measurements performed for various orientations of the magnetic field revealed the presence of a lock-in effect in Cu_xTiSe_2, when superconducting vortices are trapped along a layered structure even for tilted magnetic fields. The orientation of the vortices was experimentally determined and could be well described by a model considering the presence of an additional layered structure in which superconductivity is at least partially suppressed. The lock-in effect was analysed in three different samples and we have shown that the strength of the lock-in is independent of the copper doping, even though this effect can be masked by strong demagnetisation effects in very thin samples. The strength of this lock-in effect indicates that the superconductivity is strongly suppressed on certain layered structure. The nature of this "extrinsic" pinning structure is still unknown but might be related to the recent observation of charge density waves domain walls, which may induce strong variations of the superconducting order parameter.

Keywords:

Superconductors, Hall probes, upper and lower critical field

Contents

Introduction and motivation

In many unconventional systems, the superconductivity emerges in the proximity of another magnetic or electronic instability. The interplay between superconductivity and these other ordered states is in the centre of the research in modern solid state physics. Cu_xTiSe_2 belongs to transition metal dichalcogenides that are known to exhibit the presence of superconductivity and charge density waves (CDW) [1], as displays the electronic phase diagram of Cu_xTiSe_2 (*Temperature vs. copper doping*) [2]. CDW are already present in pure $1T$-$TiSe_2$ below ~ 200 K. With higher copper doping, CDW are suppressed and superconductivity appears creating a dome in the phase diagram of Cu_xTiSe_2. The phase diagram indicates that the CDW state could disappear completely at the copper concentration, where superconductivity reaches maximum critical temperature. It was proposed that this could be the location of a quantum critical point in the phase diagram where a phase transition occurs at absolute zero [3]. However, recent results of X-ray measurements [4] showed that this is not the case. They observed that domain walls or stacking faults appear in the compound and the CDW state does not disappear but changes its character from commensurate to incommensurate and persists along the superconducting dome up to the highest copper concentration. The periodicity of this structure is very similar to the extent of the coherence length in the c direction. Together with the fact that the incommensurate phase emerges at the same concentration as superconductivity, it suggests that the CDW state might affect the superconductivity in Cu_xTiSe_2.

In this work I present the results of local Hall probe magnetometry measurements performed on single crystals of Cu_xTiSe_2 with different copper content. The first chapter contains a short introduction to superconductivity and selected facts about this phenomenon that are going to be used throughout this work. The second chapter is concerned with the theoretical overview on vortex lattice behaviour in various orientations of magnetic field in layered materials. In the third chapter I describe the phenomenon of charge density waves and the possible mechanism of its origin.

Then I mention some of the results of the studies that were already performed on transition metal dichalcogenides and more specifically on $1T$-$TiSe_2$ under pressure and intercalated by copper atoms. The fourth chapter introduces the local Hall probe magnetometry technique and the important aspects of the analysis of the data obtained by local Hall probe measurements. The last two chapters are presenting our results obtained by investigating Cu_xTiSe_2 single crystals of different copper content and geometry. In the fifth chapter I analyse magnetic field profiles on three selected samples and the temperature dependencies of lower critical field. At the end of the chapter, there is a discussion about the doping dependence of critical fields. In the sixth chapter, I present the results of local Hall probe magnetometry measurements in magnetic field applied at different orientations. The data revealed the presence of the lock-in effect and were fit using model of Blatter, which was modified to be applicable to our case. Then I present the comparison of the lock-in effect on three samples of different copper content. In the end of the chapter six I conclude the results we obtained in the local Hall probe magnetometry study of superconducting Cu_xTiSe_2.

Chapter 1

Superconductivity

The history of superconductivity began when H. K. Onnes in 1911 measured the resistance of materials at low temperatures. He observed that the electrical resistivity in studied pure metals dropped to zero, when the temperature was decreased below certain value. The new group of materials was named superconductors, as they are able to conduct electrical current without any resistance. However, superconductor is not just an ideal conductor but at certain conditions it may behave as an ideal diamagnet. In this so-called Meissner state, supercurrents are produced in the sample, acting against the external magnetic field and shielding the interior of the superconductor.

One of the critical parameters for superconductivity is temperature but it can be also suppressed by high enough magnetic field. There are two main types of superconductors, depending on their response to external magnetic field. Type I superconductors are in the Meissner state until, at a certain magnetic field, the whole sample switches to the normal state at once. On the other hand, type II superconductors pass to the normal state gradually and let the magnetic field partially penetrate into their interior. Most of the pure and clean superconducting elements belong to the type I group, while alloys and chemical compounds (including high temperature superconductors) belong to type II group.

An example of the phase diagram (magnetic field H versus temperature T) for a type II superconductor is displayed in Fig.1.1. While the type I materials are characteristic only by one critical magnetic field, in type II there are two main critical fields. Up to the lower critical field, H_{c1}, the superconductor remains in the Meissner state and behaves as a perfect diamagnet. Above H_{c1}, magnetic field starts to penetrate into the sample in the form of vortices containing one quantum of magnetic flux, ϕ_0. When the field reaches the value of upper critical field, H_{c2}, the whole sample is in

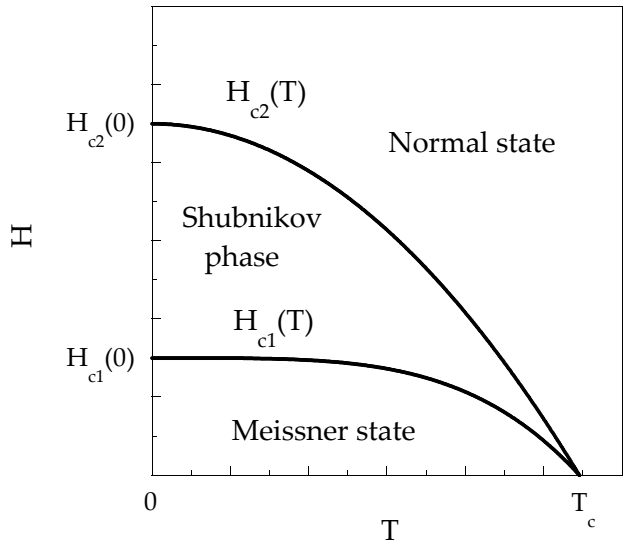

Figure 1.1: Phase diagram of magnetic field H and temperature T for type II superconductors. H_{c1} is the lower critical field above which vortices start to penetrate into the superconductor. Above the upper critical field, H_{c2}, the superconductor switches to the normal state. T_c represents the critical temperature of superconductor in zero magnetic field.

the normal state. With increasing temperature, H_{c1} and H_{c2} decrease as the superconductivity is gradually suppressed, until at $T = T_c$ both of the critical fields go to zero.

1.1 Thermodynamic properties of superconductors

Now we are going to derive the basic thermodynamic properties assuming that we have a type I superconductor. At first, we define the density of Gibbs free energy per unit of volume, g, in homogeneous magnetic field as

$$g = F(T, B) - BH, \tag{1.1}$$

where B is the induction of the magnetic field in the sample and $F(T, B)$ is the Helmoltz free energy density depending on B and T. dF accounts for the work per unit of volume HdB done by the field source to create the magnetic field and magnetize the body of the sample, and $-SdT$, which is the change of the internal energy density of the body, given as the product of entropy S per unit of volume and temperature

change dT. Then for dF we have

$$dF = HdB - SdT. \tag{1.2}$$

For the thermodynamic property characterizing the state of the superconductor, we can take the Gibbs free energy density per unit of volume associated solely with the body, G, given by $G = g - g_V$, where $g_V = -\mu_0 H^2/2$ describes the energy density of magnetic field in a vacuum without the presence of a body. G and its infinitesimally small increase at constant temperature then are

$$G = F - BH + \frac{\mu_0 H^2}{2} \tag{1.3}$$

and

$$dG = HdB - BdH - HdB + \mu_0 HdH = -\mu_0 MdH, \tag{1.4}$$

where $M = B/\mu_0 - H$ is the magnetisation per unit of volume of the superconducting sample. The equilibrium state of the superconductor is characterised by the minimum in the Gibbs free energy. In type I materials, the superconductivity lasts until the field reaches certain critical field H_c. For $H < H_c$, the Gibbs energy density in the superconducting state is lower than in the normal state, $G_S < G_N$, and vice versa, for fields above H_c, $G_S > G_N$. Then at $H = H_c$, the Gibbs energy densities of the superconducting and normal state have to be equal, $G_S(H_c) = G_N(H_c)$. When we decrease the field from H_c to certain H_0, the energy of the superconductor also decreases from the normal value by ΔG equal to

$$\Delta G = G_N - G_S = -\mu_0 \int_{H_0}^{H_c} MdH = \mu_0 \frac{H_0^2 - H_c^2}{2}. \tag{1.5}$$

The maximum energy gain is obtained when we decrease the field from H_c to zero field and we get

$$G_N - G_{S,0} = \frac{\mu_0 H_c^2}{2}. \tag{1.6}$$

From this equation we see that H_c is a direct measure of how much is the superconducting state energetically favourable compared to the normal state. Therefore, H_c is called the thermodynamic critical field.

From Gibbs free energy density we can obtain the entropy difference of normal and superconducting state as

$$\Delta S = S_S - S_N = -\left(\frac{d\Delta G}{dT}\right)_H = \mu_0 H_c \frac{dH_c}{dT}. \tag{1.7}$$

Experiments showed that $H_c(T)$ monotonously decreases with increasing temperature, thus $(dH/dT) < 0$ for $T < T_c$. Then from eq.1.7 it follows that $S_S < S_N$, meaning that the superconducting state is more ordered than the normal one. We know that at the temperature of the phase transition, the critical field goes to zero, $H_c(T_c) = 0$. Then from eq.1.7 we get $S_S(T_c) = S_N(T_c)$ and therefore the transition from superconducting to normal state is classified as the second order phase transition at $T = T_c$. Below T_c the entropies S_S and S_N differ. When the transition occurs by applying the magnetic field at constant temperature, the transition to normal state is accompanied by entropy change and it is classified as the first order phase transition.

From entropy S we can obtain the volumetric heat capacity C as

$$C = T\left(\frac{dS}{dT}\right)_H . \tag{1.8}$$

The difference of the volumetric heat capacity in the normal and superconducting state is then given by

$$\Delta C = C_S - C_N = T\left(\frac{d\Delta S}{dT}\right)_H = \mu_0 T\left[\left(\frac{dH_c}{dT}\right)^2 + H_c\frac{d^2H_c}{d^2T}\right]_H . \tag{1.9}$$

At $T = T_c$ this expression simplifies because $H_c(T_c) = 0$ and we obtain so-called Rotgers formula

$$\Delta C(T_c) = \mu_0 T_c\left(\frac{dH_c}{dT}\right)^2_{T=T_c} . \tag{1.10}$$

This expression states that there exists a discontinuity in the heat capacity at $T = T_c$ and also gives its height, which can be experimentally measured.

1.2 The London equations

The first model to describe the behaviour of a superconductor in magnetic field, was the two-fluid model of the brothers F. and H. London [5]. Within this model all of the free electrons in the superconductor can be divided into two groups. They may be either in superconducting state with the density n_S or in normal state with the density n_N. The total electron density is always conserved, $n = n_S + n_N$. Above T_c, there are no superconducting electrons and the total density is equal to $n = n_N$. On the other hand, at $T = 0$ K all of the free electrons become superconducting and $n = n_S$. With increasing temperature, n_S gradually decreases as some of the superconducting electrons become normal and n_N increases. In the London model, it is assumed that the electrical and magnetic field are low enough not to affect the density of states.

The first of the London equations is obtained by writing the second Newtons law for superconducting electrons in an electric field E

$$m\frac{dv_S}{dt} = eE, \tag{1.11}$$

where m is the electron mass, v_S is the superfluid velocity and e is the electron charge. It is assumed that n_N and n_S are constant in space and time. Taking the density of the supercurrent to be $J_S = n_S\ e\ v_S$, we get from the previous formula the first London equation

$$E = \frac{m}{n_S e^2}\frac{dJ_S}{dt}. \tag{1.12}$$

In stationary case, when $dJ_S/dt = 0$, the formula states that there is no electrical field inside the superconductor. The second London equation defines the relation between the supercurrent and the magnetic field in superconductor. Now, we substitute the Maxwell equations into eq.1.12 and integrate over time. After setting the integration constant to zero, as proposed in the London theory, we obtain the second London equation

$$H + \lambda^2 \operatorname{rot}\operatorname{rot} H = 0, \tag{1.13}$$

where λ is the London penetration depth given as

$$\lambda^2 = \frac{m}{\mu_0\ n_S\ e^2}. \tag{1.14}$$

From the second London equation used in one-dimensional case, we can find that the magnetic field penetrates into the superconductor but its amplitude falls off exponentially with increasing distance from the surface y as $H = H_0 e^{-y/\lambda}$, where H_0 is the value of magnetic field at the surface. λ is an important material property of a superconducting material, defining the length scale on which the supercurrents shield the external magnetic field to $1/e$ of its value at the surface. Since λ depends on the superfluid density, it is also temperature dependent.

1.3 Ginzburg-Landau theory

The first phenomenological theory of superconductivity was proposed by V. L. Ginzburg and L. D. Landau [6]. Opposite to the London model, it takes into account that the superconducting state is more ordered than normal one. Ginzburg-Landau theory studies the superconductivity within the Landau model of the phase transitions and

takes the quantum mechanical wave function $\psi(r)$ of the electronic superfluid as the order parameter.

Landau theory is based on the assumption that the Gibbs free energy density can be expanded into powers of ψ as

$$G_S = G_N + \lambda\psi + \alpha\psi^2 + \gamma\psi^3 + (\beta/2)\psi^4. \tag{1.15}$$

This approximation is valid only for small values of ψ, thus close to T_c. Taking into account that in normal state $G_S = G_N$, parameter λ in the expansion is set to zero dismissing the linear term in the equation. Then we can also exclude parameter γ because otherwise G_S would change with the sign and phase of ψ. For superconductors this would mean that the equilibrium state would depend on the direction of the current, which should not be the case in order to preserve the symmetry of phase and time. In magnetic field given by H and vector potential A, additional elements are added to the Gibbs energy in eq.1.15, and so the kinetic energy of the superconducting electrons and energy of the magnetic field inside the superconductor. When we consider the Gibbs free energy density related only to the body, we get

$$G_{S,H} = F_N + \alpha|\psi|^2 + \frac{\beta}{2}|\psi|^4 + \frac{1}{4m}|-i\hbar\nabla\psi - 2eA\psi|^2 - BH + \frac{B^2}{2\mu_0}. \tag{1.16}$$

To find the equilibrium state we integrate $G_{S,H}$ through the volume of the superconductor and find its minimal value with respect to $\psi(r)$ and $A(r)$, supposing that these are independent functions. As solution, we get two Ginzburg-Landau equations

$$\xi^2(i\nabla + \frac{A}{\phi_0})^2\psi - \psi + \psi|\psi|^2 = 0 \tag{1.17}$$

and

$$J_s = \frac{|\psi|^2}{\lambda^2}\left(\frac{\phi_0}{2\pi}\nabla\varphi - A\right), \tag{1.18}$$

where

$$\xi = \frac{\hbar}{(4m|\alpha|)^{1/2}} \tag{1.19}$$

is the coherence length giving a characteristic scale on which the spatial variation of ψ occurs. While at low temperatures ξ does not vary much, going closer to T_c, ξ increases with temperature as $(T_c - T)^{-1/2}$, diverging at T_c to infinity. From GL theory introducing ξ, another characteristic material property of superconductors, the thermodynamic critical field H_c can be written as

$$H_c = \frac{\phi_0}{\mu_0 2\pi\sqrt{2}\lambda\xi}. \tag{1.20}$$

1.4 Bardeen-Cooper-Schrieffer theory

The results of the Ginzburg-Landau phenomenological theory cannot be used on the microscopical scale and do not explain the origin of superconductivity. Discovery of the isotopic effect [7] was the first clue suggesting that superconductivity is related to electron-phonon interaction. If we take isotopes of the same superconductor with different atomic masses, we find that their critical temperature T_c obeys the law

$$T_c M^{\alpha} = const., \tag{1.21}$$

which is a dependence characteristic for the energy of phonons. The origin of superconductivity was explained for the first time by J. Bardeen, L. N. Cooper and J. R. Schrieffer (BCS) [8]. They predicted the existence of an attractive electron-electron interaction mediated by phonons. If this interaction is retarded against the Coulomb repulsion, it may lead to effectively coupled electrons and be responsible for the emerging superconducting state. Imagine we have a single electron in the material at $T = 0$ K, which locally increases the distribution of negative charge as it moves in the ion lattice. The local increase of negative charge attracts the positively charged ions in the lattice, which start to move towards it. Due to higher mass, the ions move much slower than the electrons, thus remaining in the movement even when the electron causing the uneven charge distribution is already gone. The redistribution of positive ions induces a local increase of positive charge that attracts another electron. As a result, the two electrons are coupled through their interaction with the crystal lattice. Such a bound state of two electrons is called a Cooper pair. Only the electrons that can shift into a new state may participate in the interaction, therefore they have to come from the close proximity of the Fermi surface. As the electrons are coupled Cooper pairs by a certain energy 2Δ, an energy gap of this size appears in the electronic structure at the Fermi surface.

An important parameter for superconductors is a so-called coupling ratio, which is the ratio of energy gap value at 0 K, Δ_0, critical temperature, T_c, and the Boltzmann constant, k_B. Its value resulting from the BCS theory calculated for an isotropic superconductor with weakly coupled electrons is

$$\frac{2\Delta_0}{k_B T_c} = 3.52. \tag{1.22}$$

This value was experimentally confirmed in many of the classical low temperature superconductors.

From the BCS theory, we can get the relation for H_c at 0 K. The difference of energy densities of normal and superconducting state can be expressed by the density of states at the Fermi surface $g(E_F)$ and $\Delta(0)$ as

$$E_S - E_N \sim -g(E_F)\Delta_0 \frac{\Delta_0}{2}. \tag{1.23}$$

In this expression $g(E_F)\Delta_0$ is the total number of electrons per unit of volume that participate in superconductivity and $\Delta_0/2$ is the binding energy per each electron in the Cooper pair. If we compare it with the condensation energy density from eq.1.6, we get the expression for $H_c(0)$:

$$H_c(0) = \Delta_0\sqrt{g(E_F)/\mu_0}. \tag{1.24}$$

Opposite to the Ginzburg-Landau theory, the BCS theory describes the thermodynamic critical field in terms of the basic material superconducting properties representing its electronic spectrum and electron-phonon interaction.

1.5 Superconducting vortices in type II superconductors

The ratio of the two characteristic lengths, the penetration depth and the coherence length gives the so-called Ginzburg-Landau parameter

$$\kappa = \frac{\lambda}{\xi} \tag{1.25}$$

As λ and ξ determine the scale of variation of H and ψ, parameter κ represents the effect of magnetic field on the order parameter. For type I superconductors, $\kappa << 1$ (or $\lambda << \xi$). The external magnetic field is shielded inside the sample by the supercurrents on the length much smaller than ξ (see Fig.1.2-$Left$). The order parameter ψ is affected by field only on a small length and the superconductivity is suppressed only when the field reaches H_c. On the other hand for type II superconductors, field affects the order parameter on much larger scale as $\lambda >> \xi$. Let us now analyse the effect of magnetic field on the order parameter by studying the surface energy of the interface of normal metal and superconductor (N-S), σ_{NS}, which is given by

$$\sigma_{NS} = \int_{-\infty}^{\infty} (G_S - G_N)dx. \tag{1.26}$$

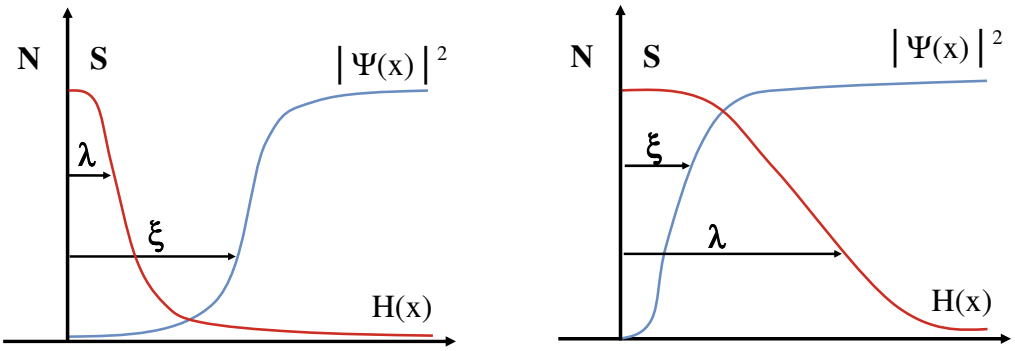

Figure 1.2: Spatial variation of the order parameter ψ and magnetic field H in type I (left) and type II (right) superconductors.

By using the Ginzburg-Landau equation (eq.1.16) and after certain editing, we can get

$$\sigma_{NS} \approx H_c^2 \int_{-\infty}^{\infty} \left[\xi^2 \left(\frac{d\psi}{dx} \right)^2 + \frac{H(H - H_c)}{2H_c^2} \right] dx. \tag{1.27}$$

By assuming that ψ changes from 1 to 0 exponentially going from superconducting to normal state, and that the field also decreases exponentially according to the London theory, σ_{NS} can be evaluated as the sum of two components

$$\sigma_1 \sim \frac{\xi H_c^2}{\mu_0} \quad \text{and} \quad \sigma_2 \sim -\frac{\lambda H_c^2}{2\mu_0}. \tag{1.28}$$

For type I superconductor where $\lambda << \xi$, the main influence comes from σ_1 and the total surface energy is always positive. To destroy superconductivity, a work $\mu_0 H_c^2/2$ has to be done to shift the N-S border by the distance of ξ. This barrier is overcome only when the magnetic field reaches H_c. Thus the type I superconductors do not allow magnetic field in their interior. In type II superconductors, the main influence on the interface energy has σ_2. As $\lambda >> \xi$, the field penetrates deep into the superconductor, far behind ξ where superconductivity still exists. In this region, electrons are still coupled in the Cooper pairs and have smaller energy than the normal electrons, resulting in the negative σ_{NS}. Therefore, for type II superconductors, it may be energetically favourable to let the magnetic field inside their interior. This happens in the form of quantized superconducting vortices despite that their formation costs some energy.

To find out why is the magnetic flux quantized in the superconductors, we take into account the wave character of the superconducting electrons and construct the quantum generalization of the second London equation. The wave function of a Cooper

pair in the superfluid condensate can be written as $\psi(r) = (n_s/2)^{1/2} e^{i\varphi(r)}$, where φ is the phase of the wave function and ψ was normalized to account that the density of electron pairs is $n_s/2$. From quantum mechanics, the momentum p of a particle with mass $2m$ and charge $2e$ in magnetic field is given by

$$p = \hbar \nabla \varphi = 2mv_S + 2eA, \tag{1.29}$$

where $\hbar$ is the Planck constant, v_S is the particle velocity and A is the vector potential of the magnetic field. Using the formula 1.14 and 1.29, we get for the density of the supercurrent

$$J_s = n_S \; e \; v_S = \frac{1}{\mu_0 \lambda^2} \left(\frac{\phi_0}{2\pi} \Delta\varphi - A \right), \tag{1.30}$$

with $\phi_0 = h/(2e)$. Now, we assume that there is a cylindrical superconductor with a hole inside. We apply magnetic field in the normal state and then begin to decrease the temperature below T_c. The sample becomes superconducting expelling the field from its interior, however some field remains in the hole inside the cylinder. To calculate the trapped magnetic flux ϕ, we integrate the vector potential A along the closed curve far from the superconductor at a distance larger than λ, where the supercurrents are zero. With the use of equation 1.14 and 1.30, we get

$$\phi = \oint A dl = \frac{\phi_0}{2\pi} \oint \nabla\varphi dl. \tag{1.31}$$

As the wave function of superconducting electrons has to be continuous, its phase may change along the curve only by the value of 2π. The result of the integral then is $2\pi n$, where n is an integer number and for the total flux we get $\phi = n\phi_0$. This means that the total flux have to be integer multiple of ϕ_0, which is the quantum of magnetic flux with the value $\phi_0 = 2.0678 \; 10^{-15}$ Tm^2.

Each superconducting vortex has a core in the normal state of size ξ, carrying one quantum of magnetic flux ϕ_0. Multiple flux quanta in one vortex would be energetically unfavourable and they would split spontaneously into collections of fundamental vortices. The field is shielded from the core by supercurrents and this area has the characteristic dimension of λ (see sketch in Fig.1.3).

The superconducting vortex is an object, which can move inside the superconductor and sustain electro-magnetic interactions. Interaction of two vortices is repulsive due to the direction of the supercurrents flowing around the normal cores, which is also the reason why vortex is repelled from the surface of the superconductor, where

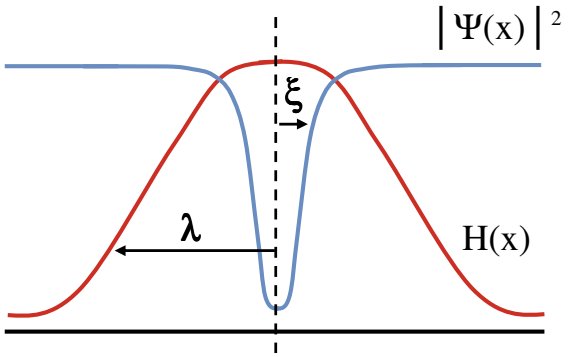

Figure 1.3: Sketch of the spatial variation of magnetic field $H(r)$ and order parameter $\xi(r)$ in the superconducting vortex. Coherence length ξ determines the size of the normal vortex core. Penetration depth λ is the length to which the field from the core penetrates into the superconductor.

supercurrents flow (see Fig.1.4). Vortices may interact also with different type of defects that are present in smaller or larger amount in any real sample. This interaction is attractive, as vortex may save part of its core energy by settling on the defect, where the superconducting order parameter is disturbed. The attractive force causes that the vortex gets pinned or trapped at the spot, which is called a pinning centre.

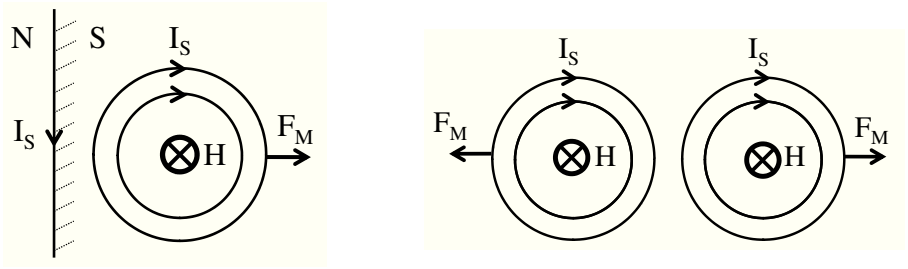

Figure 1.4: Repulsive interaction of vortex with the sample surface (*Left*) and two superconducting vortices (*Right*).

1.6 Different types of superconductivity

BCS theory considers superconductors, which are due to the symmetry of their order parameter called $s-$wave superconductors characterized by one isotropic energy gap. BCS theory sets the lower limit of the coupling ratio for the weakly coupled Cooper pairs (eq.1.22), but not the upper limit. One of the way how to determine the coupling ratio for a given superconductor is to experimentally obtain the temperature depen-

dence of the penetration length, $\lambda(T)$. In case that we neglect a small temperature dependence of κ, from BCS theory we can obtain the temperature dependence of the superfluid density directly related to the penetration depth through eq.1.14. For $\lambda(T)$ we get

$$\frac{\lambda^{-2}(T)}{\lambda^{-2}(0)} = 1 - 2\int_{\Delta(T)}^{\infty} \frac{\partial f}{\partial E} \frac{E}{\sqrt{E^2 - \Delta^2(T)}}\, dE, \tag{1.32}$$

where $\Delta(T)$ is the temperature dependent superconducting energy gap, f is the Fermi function $f = [1 + exp(E/k_BT)]^{-1}$ and the integration is done over energy counted from the chemical potential [9]. The temperature dependence of the energy gap can be approximated by [10]

$$\Delta(T) = \Delta_0\ 1.76\ \tanh[1.82\ (1.018\ [(T_c/T) - 1])^{0.51}]. \tag{1.33}$$

The only parameter in the model is the coupling ratio $2\Delta/k_BT_c$. Formula 1.32 is used in the clean limit cases, when the coherence length defining the dimension of the Cooper pair is smaller than the mean free path, l. In the opposite case, when $\xi >> l$, the superconductor is in the dirty limit and both ξ and λ are affected by electron scattering. In the dirty limit for $\lambda(T)$ according to ref.[9] follows

$$\frac{\lambda(0)}{\lambda(T)} = \frac{\Delta(T)}{\Delta(0)} \tanh\left[\frac{\Delta(T)}{2k_BT}\right]. \tag{1.34}$$

A model curves of $\lambda(T)$ normalized to λ obtained at 0 K, $\lambda(0)$, for selected coupling ratio values are compared for the case of clean and dirty limit in Fig.1.5. In general the curves saturate with $T \to 0$ K and for $T \to T_c$ the temperature dependence of λ is almost linear. The difference between $\lambda(T)$ in clean and dirty limit is significant for smaller coupling ratios but it is almost negligible already for $2\Delta/(k_BT_c) = 4.5$. Coupling ratio smaller than 3.52 indicates that the compound is not a classical $s-$wave superconductor. Most of the unconventional superconductors do not follow the BCS model, as for example they may experience different symmetry of the order parameter (e.g. d-wave high temperature YBaCuO [11]) or they might have multiple superconducting energy gaps at the Fermi surface (e.g. MgB_2 [12]). The temperature dependence $\lambda(T)$ of a multi-gap superconductors can, however, be very well approximated just by assuming that the superfluid density is the sum of two independent superfluid densities [13]

$$n_S = w\ n_{S1} + (1 - w)\ n_{S2}, \tag{1.35}$$

where $w \leq 1$ is the Fermi surface weight of the reduced gap. Therefore, $\lambda(T)$ for a multigap superconductor can be obtained by weighted sum of $\lambda_1(T)$ and $\lambda_2(T)$, each

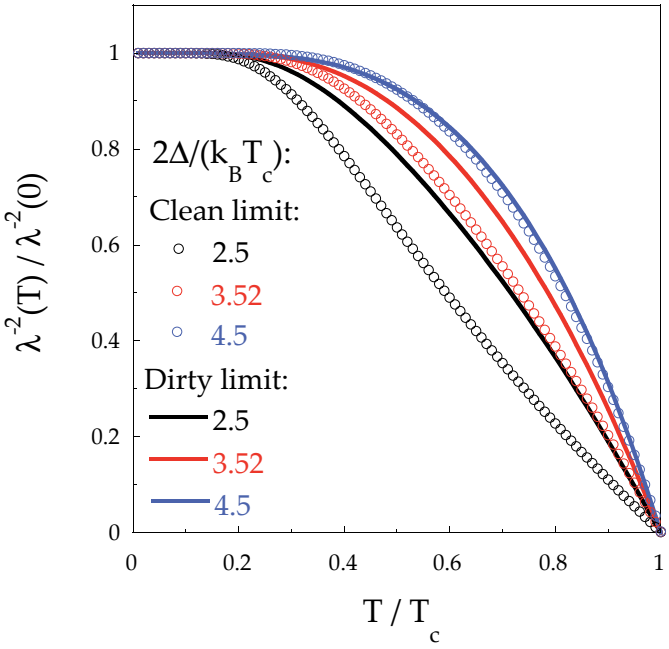

Figure 1.5: Comparison of the temperature dependence of the penetration depth $\lambda(T)$ normalized to $\lambda(0)$ in clean (open points) and dirty (thick lines) limit, constructed for different coupling ratios.

for a different coupling ratio corresponding to the gap size, giving

$$\lambda = w\ \lambda_1(\Delta_1) + (1-w)\ \lambda_2(\Delta_2). \tag{1.36}$$

Chapter 2

Vortex structure in layered superconductors

Various groups of superconductors of recent interest have a layered structure where normal and superconducting sheets alternate. This sandwich design gives rise to anisotropic features in both normal and superconducting state. Their material properties do not change within the layers but may differ significantly from their properties perpendicular to the planes (in the c direction). This ab versus c anisotropy itself is for example responsible for non-trivial behaviour of superconducting samples in magnetic field. For example, an anisotropic sample will always orient so that to have ab planes parallel with the external field [14].

Besides anisotropy, the alternating normal-superconducting structure might have a significant influence on the response of superconductor in a magnetic field. The layered superconducting materials can be divided into two distinct groups, depending on the ratio between the coherence length in c direction, ξ_c, and the interlayer distance, s [15]. If $\xi_c >> s$, the wave function of superconducting electrons spreads across few layers in the material and the superconducting order parameter is only weakly modulated along the c direction (Fig.2.6-*Right*). The layered structure is irrelevant and the superconductor is considered to be anisotropic but uniform. Such a system can be well described by 3D anisotropic Ginzburg-Landau model introducing a phenomenological mass tensor. On the other hand, if $\xi_c << s$, wave functions of superconducting electrons overlap only weakly between the planes (Fig.2.6-$Left$). The order parameter is large only in the superconducting planes and falls down to almost zero on the normal sheets between them. This case is treated by Lawrence-Doniach (LD) model that theoretically describes it as superconducting layers weakly coupled via Josephson

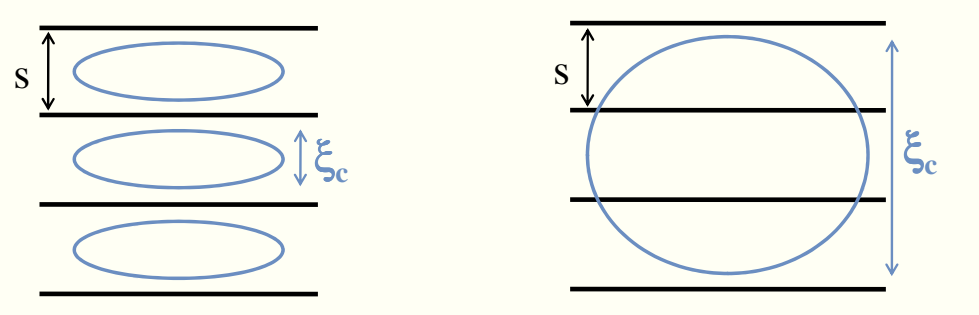

Figure 2.6: Superconducting vortices in layered materials. *Left* - Coherence length in c direction, ξ_c, is smaller than the interlayer distance s, $\xi_c < s$. *Right* - Case for $\xi_c > s$.

tunnelling [16]. It is possible that in one material both scenarios occur, since ξ_c is temperature dependent. With increasing T, ξ_c becomes larger than s and such material switches from quasi two-dimensional with weakly coupled layers to three-dimensional uniform anisotropic superconductor. This dimensional crossover is observed for example in high temperature superconductors LaSrCuO[17] and YBaCuO[18], or quasi two dimensional low temperature composites Nb/Cu[19] or Nb/Ge[20].

In the following chapter we discuss some interesting results of the mentioned models and corresponding theories regarding the anisotropic superconductors. Firstly, we mention the 3D Ginzburg-Landau model for uniform anisotropic superconductors and 3D London model, which is used in general to find out about the vortex structure. Then we discuss the Lawrence-Doniach model for superconductors where the alternating superconducting and normal layers play an important role. Next, we discuss the Blatter model accounting for a layered structure present in the material which does not have to be of an intrinsic origin. One of the features of both Lawrence-Doniach and Blatter model is the lock-in effect.

2.1 3D anisotropic Ginzburg-Landau model

Most of simple superconducting materials (e.g. Sn, Pb, Nb, Al) has crystallographic structure close to cubic one. Their critical temperature of superconducting state is low and the electronic bands are wide with small effective mass of conducting electrons. Coherence length is bigger than the inter-atomic distance, thus the crystallographic structure of the material is not affecting superconductivity and the BCS isotropic theory gives an accurate description for most of the materials. In layered supercon-

ductors, such as intercalated transition metal dichalcogenides, the layered structure affects their electronic properties. Neighbouring planes are coupled to each other by weak Van der Waals interactions and electrons move freely in the ab direction. On the other hand, the overlap of electronic wave functions between the layers is small thus motion between the planes is characterized by a narrow band (for a summary see [21]).

The 3D anisotropic Ginzburg-Landau (GL) theory describes properties of superconducting and normal electrons by introducing into the basic GL equations the inverse effective mass tensor. For uniaxial layered materials some of the directions are equal and it is sufficient to consider two main directions in the Fermi surface. Then the mass tensor has only two elements: m in the ab planes and M for the c direction. The value of upper critical field in the two distinct directions is then obtained from linearised GL equations with the effective mass tensor:

$$H_{c2}^{c} = \frac{\phi_0}{2\pi\xi_{ab}^2}, \tag{2.1}$$

$$H_{c2}^{ab} = \frac{\phi_0}{2\pi\xi_{ab}\xi_c}. \tag{2.2}$$

As the coherence length $\xi_i \propto m_i^{-1/2}$ (see chapter 1, eq.1.19), from the previous formula we get

$$\Gamma_{H_{c2}} = \frac{H_{c2}^{ab}}{H_{c2}^{c}} = \frac{\xi_c}{\xi_{ab}} = \sqrt{\frac{M}{m}} = \Gamma \tag{2.3}$$

2.2 3D anisotropic London model

Now we are going to analyse the vortex structure of the anisotropic superconductor. Assuming that the spatial variation of ψ in GL expansion (eq.1.16) is small and the vortex core contribution may be neglected, we obtain the London functional for the free energy

$$F \approx \int [H^2 + \lambda_{ij}^2 (rotH)^2] dV, \tag{2.4}$$

where λ_{ij} is related to the effective mass tensor as

$$\lambda_{ij}^{-2} \approx \frac{\Psi^2 e^2}{m_{ij}}. \tag{2.5}$$

This model was thoroughly studied by many authors but we present here the results for the lower critical fields in field applied parallel with ab planes, H_{c1}^{ab}, and in magnetic

field parallel with c axis, H_{c1}^c, presented by Clem in his review [22]:

$$\mu_0 H_{c1}^c = \frac{\phi_0}{4\pi\lambda_{ab}^2}[\ln\kappa_c + \alpha(\kappa_c)], \quad \kappa_c = \frac{\lambda_{ab}}{\xi_{ab}}, \tag{2.6}$$

$$\mu_0 H_{c1}^{ab} = \frac{\phi_0}{4\pi\lambda_{ab}\lambda_c}[\ln\kappa_{ab} + \alpha(\kappa_{ab})], \quad \kappa_{ab} = \frac{\lambda_c}{\xi_{ab}}, \tag{2.7}$$

where parameter α depends on the small core contribution. Brandt in reference [23] numerically obtained results for $\alpha(\kappa)$ that are valid for wide range of Ginzburg-Landau parameters and magnetic fields ranging from H_{c1} to H_{c2}:

$$\alpha(\kappa) = 0.5 + \frac{1+\ln 2}{2\kappa - \sqrt{2} + 2}\,, \tag{2.8}$$

where λ_{ab} and λ_c are the penetration depth values in the ab planes and parallel with the c direction, respectively. Typical values of α are around 0.1 and for superconductors with large κ do not affect significantly the resulting value of H_{c1} in eq.2.6 and 2.7. Ratio of λ_c and λ_{ab} gives the anisotropy Γ_λ, which is equal to $\Gamma_{H_{c2}}$ but not equal to the ratio of lower critical fields $\Gamma_{H_{c1}}$ as

$$\Gamma_\lambda = \frac{\lambda_c}{\lambda_{ab}} = \frac{H_{c1}^c}{H_{c1}^{ab}}\,\frac{\ln\kappa_c + \alpha(\kappa_c)}{\ln\kappa_{ab} + \alpha(\kappa_{ab})} \approx \frac{H_{c1}^c}{H_{c1}^{ab}} = \Gamma_{H_{c1}} \tag{2.9}$$

Next, we are going to study the vortex structure of anisotropic superconductor for various field orientations. The free energy of a vortex deflected from the ab direction by angle θ_B is given by

$$F(\theta_B) = \left(\frac{\phi_0}{4\pi\lambda_{ab}}\right)^2 \varepsilon(\theta_B)\ln\frac{\kappa_c}{|\varepsilon(\theta_B)|^{1/2}}\,, \tag{2.10}$$

where $\varepsilon(\theta_B)$ describes the angular scaling function $\varepsilon(\theta_B) = (\Gamma^{-2}\cos^2\theta_B + \sin^2\theta_B)^{1/2}$ [24]. For fields close to H_{c1} we neglect the vortex interactions and for an arbitrary orientation of magnetic field H tilted by angle θ_H from ab planes we get the expression for Gibbs energy

$$G(\theta_B) = F(\theta_B) - BH\cos(\theta_B - \theta_H)\,. \tag{2.11}$$

From minimizing G with respect to θ_B we obtain the optimal value θ_0. By setting $G(\theta_0) = 0$, we obtain the relations for dependence of H_{c1} on the orientation of magnetic

field at $H = H_{c1}$

$$H_{c1}^2(\theta_H)\left(\frac{\cos^2\theta_H}{H_{c1}^{ab\,2}} + \frac{\sin^2\theta_H}{H_{c1}^{c\ 2}}\right) = 1\ , \tag{2.12}$$

and at $H = H_{c1}$ we get

$$\Gamma^2 = \frac{\tan\theta_H}{\tan\theta_B} \tag{2.13}$$

From this equation follows that if the superconductor is isotropic (see $\Gamma = 1$ in Fig.2.7), vortices are always aligned with the magnetic field and for any orientation $\theta_B = \theta_H$. On the other hand, for anisotropic superconductor (e.g. $\Gamma = 10$ in Fig.2.7), it is energetically favourable for vortices to enter the sample oriented close to, but not parallel with, ab direction when θ_H is close to the ab planes. With increasing θ_H vortices stay oriented almost parallel with the ab planes until θ_H approaches 90° and vortices finally tilt to the field orientation, $\theta_B = \theta_H$.

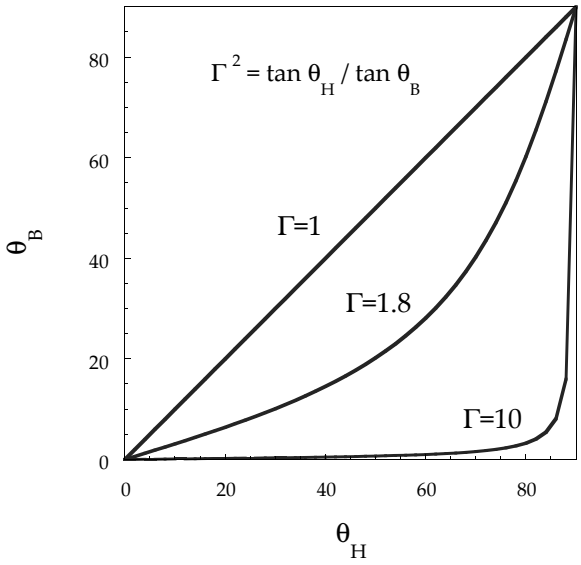

Figure 2.7: Angular dependence of vortex orientation on the direction of magnetic field for different anisotropy values at $H = H_{c1}$. 0° is the in-plane direction and 90° is parallel with the c direction.

Sudbo *et al.* in ref.[24] calculated that the 3D anisotropic London model can have two solutions for certain range of magnetic fields, Ginzburg-Landau parameters κ and anisotropies Γ. In case of isotropic superconductor, the Gibbs free energy function has always only one minimum while for anisotropic case it can have two as it is shown in the Fig.2.8 for $\kappa = 10$ and $\Gamma = \sqrt{200}$. This means that there exist vortices with

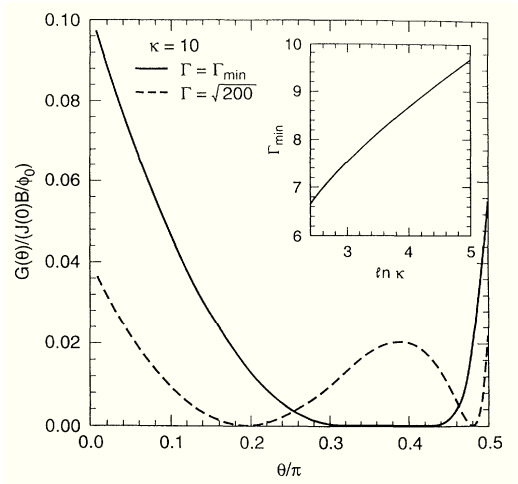

Figure 2.8: Gibbs energy G as a function of vortex orientation for $\kappa = 10$ and different anisotropy values [24]. Γ_{min} describes the lowest value of anisotropy for which G function has only one minimum.

two different orientations for given field. Some of the vortices are oriented almost parallel with the *ab* planes while the others are tilted closer to the field direction and their combination resembles by its shape a staircase structure. It is important to note that the Gibbs energy has never minimum at 0° and vortices are never aligned exactly parallel with the *ab* direction. Such a coexistence of two different vortex lattices was proposed as a possible explanation of chains of flux lines observed by Bitter decoration technique in $Bi_{2.2}Sr_2Ca_{0.8}Cu_2O_8$ [25].

2.3 Lawrence-Doniach model

Many of the anisotropic superconductors consist of 2D layers where the superconductivity primarily resides, stacked along the c direction alternating with sheets in normal state. Due to the high anisotropy, the coherence length along c direction is smaller than interlayer distance. Between the layers, the overlap of superconducting electron wave function is small and the singular sheets are bounded together only by weak Josephson coupling. According to the Lawrence-Doniach (LD) model treating such samples, vortex core fits between the planes where the superconducting order parameter is small and the presence of vortex does not require any additional suppression of superconductivity. In magnetic field parallel with the *ab* planes, the vortex is described as to have "a pancake" shape with normal core being absent, resembling a Josephson vortex [16]. The free energy of this single vortex is obtained from LD

functional presuming that $\xi_c << d$.

Vortex system in such a superconductor was theoretically analysed by Feinberg [26] and Bulaevskii [27] using the 3D London equations. The resulting vortex structure depends on the angle and amplitude of applied field (θ_H, H), see Fig.2.9 for schematic phase diagram of vortex structure. When condition $\tan\theta_B > \Gamma$ is fulfilled, vortices have straight effective cores, while for $\tan\theta_B < \Gamma$ they create the staircase structure, which consists of kinks composed of Josephson vortices and 2D cores in the layers. When magnetic field approaches the ab plane orientation the kinks disappear and vortices get locked parallel with the ab direction with their cores centred between the planes.

This so-called lock-in state is energetically more favourable when the gain on condensation energy is larger than the loss for not being aligned in the field direction. With increasing field amplitude, the energy gain decreases and when the field reaches critical value $H = H_L$, the lock-in state collapses. For a given angle, the maximum amplitude of H_L is limited by lower critical field in the c direction, such that

$$H_L \sin\theta_H < H_{c1}^c. \tag{2.14}$$

When the component of magnetic field reaches the critical value in the c direction, $H\sin\theta_H = H_{c1}$, vortices start to penetrate into the superconductor also along the c

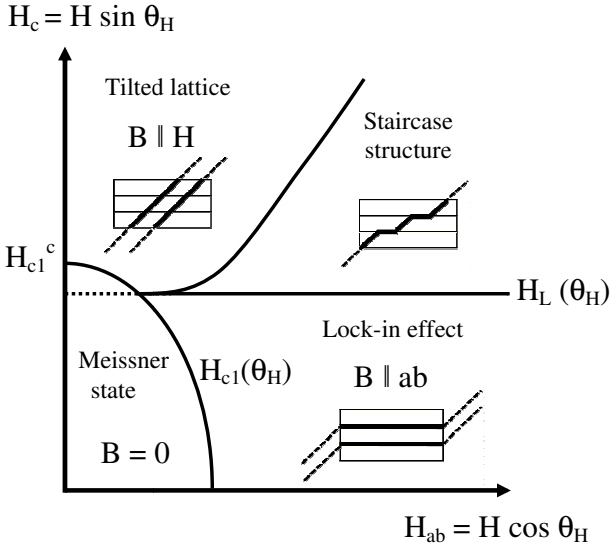

Figure 2.9: Example of a phase diagram of vortex structure in anisotropic superconductors with Meissner state, lock-in state, staircase structure and tilted vortex lattice.

direction and the lock-in state becomes unstable. For H_L it follows that

$$H_L = \lambda H_{c1}^c / \sin\theta_H, \tag{2.15}$$

where parameter λ defines the strength of the lock-in effect, ranging from 0 for no effect to 1 for the strongest possible one. λ depends on the intrinsic pinning responsible for the locking of vortices between the planes. In Lawrence-Doniach model it is approximately equal to ratio of interlayer distance and coherence length along c direction, $\lambda \sim d/\xi_c$ [16].

The intrinsic lock-in effect was experimentally observed by different techniques. The locking of vortices parallel with the planes can manifest itself as an intrinsic pinning or a large barrier for vortex motion normal to the layers [28]. As H_L is the highest for orientations close to the layers, this behaviour is usually observed in field orientations close to the *ab* planes. Deviations in torque measurements observed on YBCO were also interpreted as being due to the lock-in effect [29, 30]. Analysis of this data showed that at small angles close to planes direction, a transition from 3D to 2D behaviour occurred, as Lawrence-Doniach model was better to fit the data than the Ginzburg-Landau model. The strength of the intrinsic lock-in effect obtained from these torque measurements was $\lambda \sim 0.5$. Another experiment confirming the presence of lock-in effect, was done by Mansky *et al.* [15] by ac and dc susceptibility measurements. The studied superconductor was an organic compound (BEDT-TTF)$_2$Cu(SCN)$_2$ with $\Gamma \sim$20 and ratio $d/\xi_c \sim$5. The screening of the ac field was reduced when vortices became locked parallel with the *ab* direction and could move freely in the planes. When the lock-in state collapsed, the vortex lines pierced through the layers and their motion rapidly decreased. The measurements were done for different temperatures showing that the lock-in field H_L and lower critical field H_{c1}^c are decreasing with increasing temperature with the same rate. As the result, the strength of the lock-in effect was found to be constant with temperature, being around $\lambda \sim 0.47$.

2.4 Vortex trapping on twinning planes

Vortex lock-in effect is not limited only to the layered superconductors where vortices can fit their cores between the layers. Blatter *et al.* in ref.[31] proposed a model describing the vortex trapping on a periodic array of twin boundaries, which would also result in the lock-in effect. In this model, the layered structure of superconductor

plays no role. The model postulates that in the material exists a periodic array of twinning planes, where superconductivity is at least partially suppressed and the planes thus serve as a pinning space for the vortices. Such a layered structure allows a vortex in tilted magnetic field to deform its shape and lower its energy. As proposed in the sketch in Fig.2.10, the vortex will create a staircase structure with the core of length r partially laying in the twinning plane. On one hand the vortex saves energy by having part of the core pinned in the plane but loose on the elastic deformation. The gain can be expressed in terms of reduced vortex line energy per length, ε_{TP}, times the length of the core lying on the twinning plane r. With $\varepsilon_l(\theta_B)$ being the regular line tension per unit length depending on the orientation of magnetic induction in the sample, θ_B, the total energy balance of deformed vortex can be expressed following the sketch in Fig.2.10 as

$$E'(r, \theta_B) = (r + s - t)\varepsilon_l - r\varepsilon_{TP} \ . \tag{2.16}$$

By using approximations for small angles, the optimal value of r at fixed angle θ_B can be found as

$$r \approx (\theta_B) = d_{TP}\left[\frac{1}{\theta_B} - \frac{1}{\theta_t}\right] f(\theta_t - \theta_B) \ , \tag{2.17}$$

where d_{TP} is the distance between the twinning planes, f is a certain function depending on the difference of θ_t and θ_B, and θ_t is the critical angle below which the vortex starts to deform to a staircase structure, given as

$$\theta_t = \left(\frac{2\ \varepsilon_{TP}}{\varepsilon_l}\right)^{1/2} . \tag{2.18}$$

Considering small vortex density n, the energy contribution due to the twinning planes

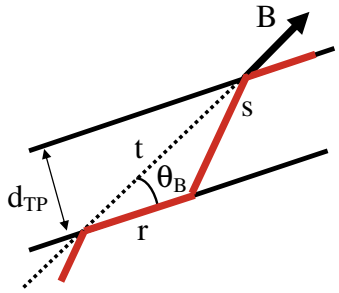

Figure 2.10: Sketch of the accommodation of an individual vortex line to an array of twinning planes [31].

per unit length is given as

$$E(\theta_B) = \frac{n}{t}\, E'[r(\theta_B), \theta_B] \approx -\frac{1}{2}\, \varepsilon_l\, n\, (\theta_t - \theta_B)^2\, f(\theta_t - \theta_B)\ . \tag{2.19}$$

The total density of Gibbs free energy of the vortex system in magnetic field tilted by angle θ_H from the planes direction thus is

$$\begin{aligned} g = {} & \frac{B^2}{2\mu_0} + \frac{\phi_0 B \varepsilon_l}{2(4\pi\lambda)^2} \ln\left[\frac{H_{c2}^c}{\varepsilon_l B}\right] \\ & -\frac{B}{\phi_0}\, \frac{\varepsilon_l}{2}\, (\theta_t - \theta_B)^2\, f(\theta_t - \theta_B) \\ & -BH\cos(\theta_B - \theta_H)\ . \end{aligned} \tag{2.20}$$

The first element in g is related to the increasing number of vortices with magnetic field, the second one describes the energy of supercurrents, the third one is the formula concerning the energy gain from pinning on the twinning planes, and the last one defines the energy of vortex in magnetic field tilted by angle θ_H from the plane direction. After assuming that the line tension ε_l is constant for the approximation of small angles, we can find the minimum of g with respect to θ_B and obtain the field dependence of orientation of internal magnetic induction for a given orientation of applied field,

$$\frac{\theta_B}{\theta_H} \approx \begin{cases} 0 & , \theta_H < \theta_L \\ 1 - \dfrac{\theta_L}{\theta_H} & , \theta_L < \theta_H < \theta_t \\ 1 - \dfrac{\theta_L}{\theta_t} & \\ 1 & , \theta_t < \theta_H \end{cases}$$

where θ_L is the lock-in angle given by

$$\theta_L = \frac{4\pi\varepsilon_l}{\phi_0 H}\, \theta_t. \tag{2.21}$$

In this model, the strength of the lock-in effect depends on the relative suppression of the core energy in the twinning plane to the regular line tension, $\lambda \sim \sqrt{\varepsilon_{TP}/\varepsilon_l}$. As an example, by using the results of decoration experiments of Dolan *et al.* on YBaCuO [32], Blatter evaluated $\lambda \sim 2 \cdot 10^{-3}$.

Chapter 3

Cu_xTiSe_2

3.1 Charge density waves

Charge density waves (CDW) are periodic longitudinal modulations in the density of conduction electrons. Depending on their origin, CDW may be accompanied by the distortions in atomic lattice. This phenomenon was discovered in quasi 2D electronic systems more than 40 years ago but due to its complexity it is still in the centre of recent research.

The first one to predict the existence of CDW was R. E. Peierls, when he discovered an instability in the electronic configuration of one-dimensional metal. Let us consider the case of a material with half-filled conduction band (see Fig.3.11). At Peierls transition, certain energy is spent to move the ions in the crystal from their equilibrium position and the lattice constant changes from a to $2a$. Subsequently, the borders of the first Brillouin zone shift from $k = \pi/a$ to $k = \pi/2a$ and the conduction electrons with wave vector $k \sim \pi/2a$ scatter at the first Brillouin zone. The electron scattering leads to opening of the energy gap at the Fermi level and softening of the phonon modes around $q = \pi/a$. Due to the energy gap, the conduction electrons shift to lower energy levels and their total energy decreases. The Peierls transition may also occur in the other way around, when atoms shift to new positions due to the irregular distribution of electron charge, which creates uneven electric potential. Periodic lattice distortion and charge density waves appear simultaneously and different theories of the origin of CDW try to identify which one is the cause of the other.

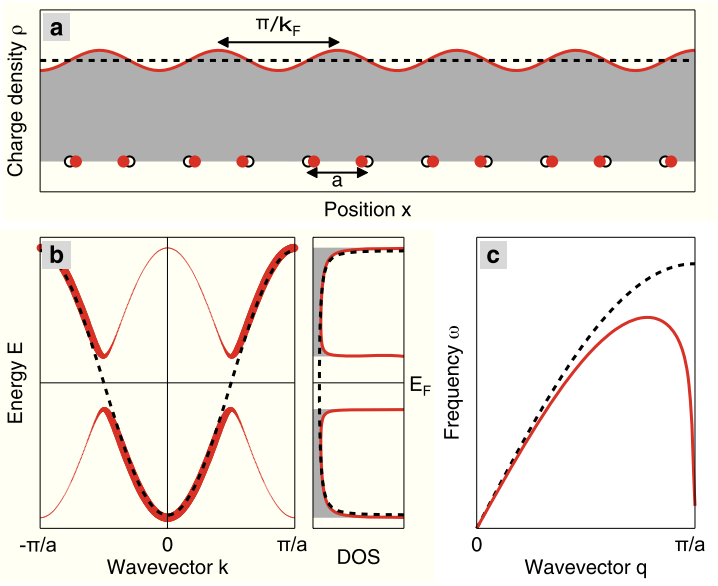

Figure 3.11: Peierls instability of a metal with a half filled conduction band, schematic view. a.) Charge density waves accompanied by distortion of lattice atoms from their equilibrium position. b.) The electron spectra of the metal before (dashed black line) and after Peierls transition (solid red line). c.) Dispersion of acoustic phonons before (dashed black line) and after (solid red line) the Peierls transition, [1].

3.2 Formation of CDW

The energy associated with the lattice distortion is given by

$$dE_{lattice} = \frac{1}{2} M \omega_q^2 u_q^2, \tag{3.1}$$

where M is the ionic mass and u_q is the static displacement of the phonon mode with wave vector q and frequency ω_q. The displacement of ions in the lattice sets up a potential v_q due to which the change of total band energy of the electron system is

$$dE_{band} = -|v_q|\chi_0(q), \tag{3.2}$$

with $\chi(q)$ being the non-interacting electronic susceptibility defined as

$$\chi(q) = \frac{1}{L} \sum_k \frac{f_{\epsilon_k+q} - f_{\epsilon_k}}{\epsilon_k - \epsilon_{k+q}}. \tag{3.3}$$

In this definition, f is the Fermi function and L is the length of the atomic chain. To maintain this state stable, the gain must at least compensate for the energy spent to

move atoms in the lattice, $\partial E_{band} + \partial E_{lattice} < 0$ for a certain phonon mode. From eq.3.3 follows that χ is the direct measure of the band energy gain due to the lattice distortion. To have large χ value, one needs a large numerator $f_{k+q} - f_k$, a small denominator $\varepsilon_k - \varepsilon_{k+q}$ and high density of states to have many such q-coupled states. One of the possible mechanism of CDW formation is thus so-called nesting, which occurs if there exists parallel parts on the Fermi surface that are symmetric by a translational vector and provide large contribution to χ [33]. The electrons from the Fermi surface scatter between the symmetric positions and charge density waves appear. In one dimension, the condition is perfectly fulfilled, as the Fermi surface can be represented by infinitely extended sheets normal to Fermi vectors k_F and $-k_F$. Consequently χ diverges at $q_0 = 2k_F$ and the phonon mode q_0 is completely softened ($\omega(q_0) \rightarrow 0$). In two-dimensional case, the Fermi surface of nearly free electrons is circular and the condition is satisfied for only one q at a time. However, if the dispersion of quasi-particles around the Fermi surface is anisotropic, the circle might be deformed with flat parts fulfilling the condition for large χ. The resulting energy gain from nesting and CDW formation will depend on the size and curvature of the parallel segments of Fermi surface. Another possibility is that there exists saddle points on the Fermi surface with increased density of states that can be connected by a vector q. A strong electron-phonon interaction is also important for CDW formation, so that the energy flow between electron and lattice system is available.

Another mechanism of CDW is the direct Jahn-Teller effect proposed in 1977 by H. P. Hughes [34]. This model is based on the fact that the energy of $d_{z^2}-$ electrons can be lowered if the compound goes through a structural transformation. The Jahn-Teller effect occurs if the energy loss from structural change is outmatched by gain from lowering electron energy levels. However, d-electrons in the lower states are electrostatically less stable. Compounds with full d-band (e.g. MoS_2) may acquire more energy from the structural transformation than the elements of V.B group that have usually only one d-electron in the valence band. IV.B group elements with empty d-band would not gain energy by such a structural transformation thus the Jahn-Teller effect is not probable for them at normal conditions. However, the electron structure can be modified by doping or intercalation and the empty d-bands might be filled which would increase the possibility for structural transformation. Beside direct Jahn-Teller effect there exists also so-called indirect one when the lowering of energy levels of occupied valence band is mediated by electron-hole coupling [35]. Periodic lattice distortion leads to the degeneration of unoccupied conduction band, which

then pushes down the energy of occupied valence band and lowers the total energy.

Another example of CDW mechanism is the transition of a semiconductor with indirect gap to an excitonic insulator [36], which occurs due to electron-electron Coulomb interaction. The schematic transformation of electron spectra is displayed in Fig.3.12. The valence band of the semiconductor is filled with electrons and has a maximum at $k = 0$. The conduction band is filled with holes and has minimum at $k = \pi/a$. In such a system, electrons and holes can create coupled pairs, so-called excitons with binding energy, E_b. The transition to excitonic insulator occurs if the energy of the gap decreases and becomes comparable with the exciton energy E_b. The electronic system will be unstable and excitons will form spontaneously. The electrons and holes will be coupled in quasi particles, which leads to opening of a large energy gap in the spectra and the new state is called excitonic insulator. Similar is the case of semimetal with small indirect overlap of valence and conduction bands. Lowering of the overlap leads to smaller amount of charge carriers, which will also reduce the screening of Coulomb interaction. This enables the outbreak of excitons and the semimetal becomes insulating. In general, the formation of an excitonic insulator is followed by modifications in the band structure, might (e.g. in $1T$-$TiSe_2$ [37]) or might not (e.g. Ta_2SiNe_5 [38]) lead to the lattice distortion and appearance of charge density waves.

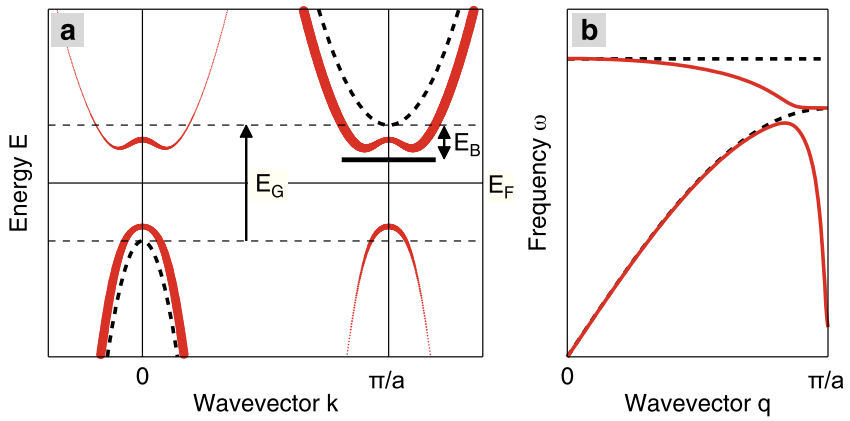

Figure 3.12: Excitonic insulator instability of a semiconductor with a small indirect gap, schematic view. a.) Electronic band dispersion in normal (dashed black line) and excitonic state (solid red line). b.) Exciton and phonon dispersions in normal (dashed black line) and excitonic state (solid red line). [1]

3.3 Transition metal dichalcogenides

Cu_xTiSe_2 is obtained by copper intercalation between the layers of $1T$-$TiSe_2$, which belongs to the group of transition metal dichalcogenides (TMD) known for their quasi-two-dimensional character. Depending on their composition, they can be semiconductors (e.g. MoS_2, WS_2), semimetals (e.g. WTe_2, $TiSe_2$) or true metals (e.g. NbS_2, VSe_2). At low temperatures some of them become superconducting, with properties similar to other unconventional superconductors. For example, some of them are multiple gap superconductors as MgB_2 or have an energy gap with pseudogap features, which are often seen in pnictides or cuprates.

Each layer of bulk TMD is composed of a mixture where per one transition metal atom M (e.g. Ti, Ta, Nb) there are two chalcogenide atoms X_2 (S, Se, Te). In each layer, M and X atoms are connected by strong in-plane covalent bonds creating a hexagonal lattice. Individual MX_2 layers are coupled together by weak Van der Waals forces. Depending on mutual orientation of the neighbouring layers, chalcogenides surrounding metal atom may create two distinct coordinations, either octahedral or trigonal prismatic. These two structures can alternate along the c axis in various order, creating variety of structural polytypes with diverse electronic properties. Two most common polytypes of TMD are $1T$ and $2H$ where the figure represents number of layers in one unit cell and the letter describes symmetry of the structure (Fig.3.13). In $1T$ polytype, identical octahedral layers repeat with trigonal symmetry while poly-

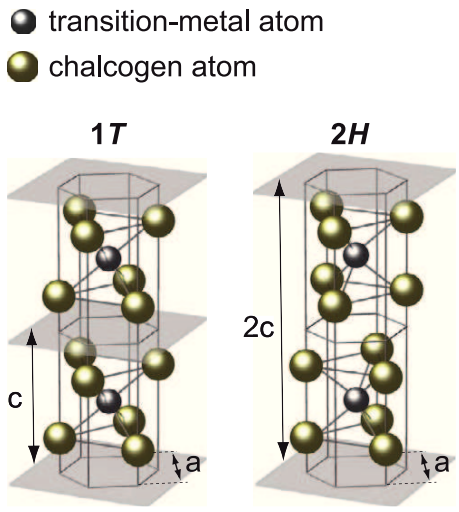

Figure 3.13: Structure of octahedral $1T$ and trigonal prismatic $2H$ polytypes of transition metal dichalcogenides.[1]

type $2H$ has hexagonal symmetry and consists of two layers in the trigonal prismatic configuration.

Electronic properties of these two polytypes are in general very different. In pristine $1T$ compounds, superconductivity has never been observed at ambient pressure but CDW were often seen close to room temperature. As CDW state is accompanied by an energy gap opening in the electron spectra, these materials are semimetals or semiconductors at standard conditions. Regarding the $2H$ polytype compounds, they are known to have more complicated Fermi surface where dual ordering is possible and superconductivity and CDW may coexist (see [1, 39] for review).

Among all the pristine TMD, $2H$-$NbSe_2$ has the highest critical temperature of superconducting transition with $T_c = 7.2$ K at ambient pressure. It is a multi-gap superconductor with two distinct gaps localized on two different sheets of Fermi surface [40, 41]. Below $T_{CDW} = 35$ K, CDW state appears with characteristic wave vector incommensurate with the crystal lattice [42]. The angle-resolved photoemission spectroscopy (ARPES) showed that the CDW energy gap in $2H$-$NbSe_2$ does not close at T_{CDW} but was also observed well above this temperature in the normal state [43], which is a feature characteristic for pseudogap. When hydrostatic pressure is applied to $NbSe_2$, the CDW state is suppressed (T_{CDW} decreases linearly with pressure) while superconducting T_c is even slightly enhanced up to 8 K [44]. According to [45], it seems that the phonon acoustic mode that drives CDW transition in $2H$-$NbSe_2$ barely contributes to superconductivity that would explain the insensitivity of T_c to suppression of CDW state. Seemingly similar system is $2H$-NbS_2 with $T_c = 5.8$ K and two superconducting energy gaps, each located on different sheet of Fermi surface. Recent measurements on this compound showed a strong softening of the phonon modes in some directions, however, no CDW state has ever been observed here [46].

Most of the TMD do exhibit the presence of CDW and superconductivity. Layered structure and two-dimensional character make them suitable for intercalation of atoms or organic molecules between the layers of MX_2, which can tune their electronic properties and so the presence of the two ordered states. Upon intercalation, electrons are transferred from the intercalant to electron bands of the TMD. As a result, the CDW state is suppressed and the generated compounds often show high anisotropy in both superconducting and normal properties.

Superconductivity usually coexists with incommensurate CDW (ICDW) when the characteristic wave vector of CDW is not integer multiple to the crystal lattice wave vector. The appearance of superconductivity with commensurate CDW (CCDW)

phase is relatively rare. $1T$-TaS_2 was the first reported pristine TMD where superconductivity was introduced by pressure [47]. Incommensurate CDW state is observed in the system already at standard conditions and at lower temperatures it passes to commensurate phase. By applying the hydrostatic pressure, the CCDW state is destabilized already below 1 GPa but CDW remains present in the system in incommensurate phase, which is suppressed more slowly with pressure. At around 3 GPa, superconductivity emerges and for certain pressure range it coexists with ICDW state. Superconductivity can be introduced into $1T$-TaS_2 also by replacing sulphur atoms with selenium [48]. For different Se concentrations, the CDW state exists in commensurate or incommensurate configuration but the superconducting state appears in $1T$-$TaS_{2-x}Se_x$ only along with the ICDW phase. On the other hand, one well known example of TMD where superconductivity coexist with CCDW phase, is $2H$-$TaSe_2$ [49]. Its critical temperature is quite small ($T_c = 0.2$ K), however by irradiating the sample it can be increased up to 2 K [50]. The irradiation introduces disorder into the CDW state, which suggests that the resultant increase of T_c might be also connected with the incommensuration of the CDW.

3.4 CDW and superconductivity in $1T$-$TiSe_2$

At ambient conditions, $1T$-$TiSe_2$ is a semiconductor or semimetal with small indirect gap. Below $T \sim 200$ K [51], it undergoes second order phase transition to CDW state that is accompanied by lattice distortion in Se-Ti-Se layer (Fig.3.14-*Left*). The characteristic CDW wave vectors are commensurate with the crystal lattice, with wavelength $2a \times 2a \times 2c$, where a and c are the lattice constants. The schematic Fermi surface of $1T$-$TiSe_2$ is displayed in the Fig.3.14-*Right*. The relevant electronic states here are the Se $4p$ valence band with the highest energy located in the centre of the Brillouin zone (point Γ) and the Ti $3d$ conduction band with minimum at the zone edges (point L).

The mechanism of CDW formation in this system was thoroughly studied. Nesting on the Fermi surface can be excluded due to different size and anisotropy of Se and Ti Fermi surface pockets. Analysis of the ARPES measurements showed that the $p-d$ band interaction stays behind the CDW formation in this system [1]. In the commensurate CDW phase, Γ and L points of reciprocal lattice become equivalent and since the gap between the bands is small enough, the p and d band states interact. Consequently, band hybridisation occurs lowering the energy of the occupied p states

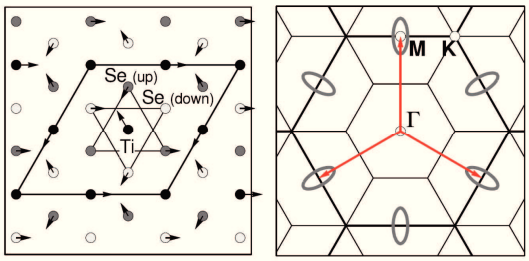

Figure 3.14: Schematic real-space unite cells (*Left*) and Brillouin zones (*Right*) for commensurate CDW lattice of $1T$-$TiSe_2$. Small black arrows show atomic distortions (size not to scale) and long red arrows indicate 3 characteristic CDW wave vectors [1].

and making the CDW state stable.

However, it is still not clear what is the type of interaction between the bands. Phonon mediated interaction would favour Jahn-Teller instability and the driving force of CDW would be the lattice distortion. On the other hand, Coulomb interaction between p holes and d electrons leads to an excitonic insulator scenario. In that case, the instability leading to CDW formation would be primarily electronic and the lattice distortion would be the consequence of electron-phonon coupling present in this system. Both models could qualitatively explain the CDW formation but the strong electron-electron interaction in $1T$-$TiSe_2$ favours the Jahn-Teller effect. Nevertheless, the calculations of ARPES spectra from tight-binding model [1] showed that the experimentally observed amplitude of atom displacement in $1T$-$TiSe_2$ is not high enough to cause opening of such a big energy gap as observed. Further, the low carrier densities in the bands result in weak screening of Coulomb interaction between $4p$ holes and $3d$ electrons, so that the electron-hole coupling may also play a significant role [52]. The excitonic contributions thus cannot be excluded and it is possible that both mechanisms, Jahn-Teller instability and excitonic insulator, coexist or even cooperate on CDW formation in $1T$-$TiSe_2$ [53].

Similarly to other TMD, the superconductivity can be introduced into $1T$-$TiSe_2$ by applying hydrostatic pressure [54]. Kusmartseva *et. al.*, based on their resistivity measurements in pressures up to 10 GPa, constructed the phase diagram shown in Fig.3.15. With increasing pressure, T_{CDW} decreases and at 2 GPa superconducting state appears. Its critical temperature T_c reaches maximum of 1.8 K at 3 GPa and decreases with further pressure applied, resulting in a dome shape of the superconduct-

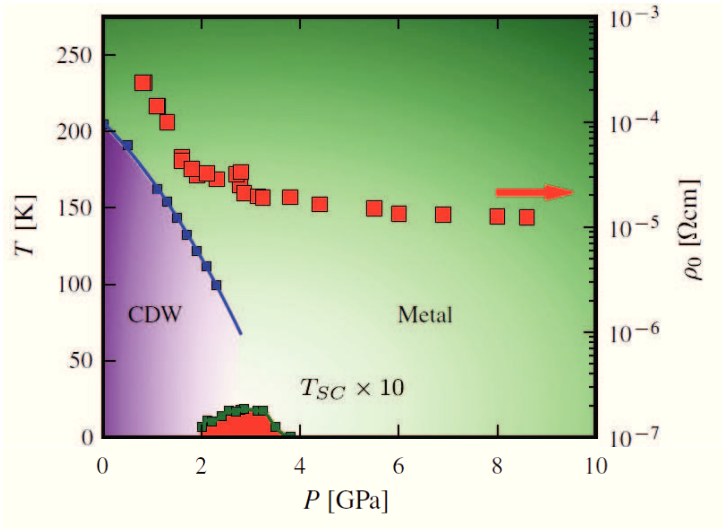

Figure 3.15: Pressure-temperature phase diagram of $1T$-$TiSe_2$ constructed from resistivity measurements. Blue and green points of CDW and SC transition, respectively, are relate to the left temperature axis. Right axis represent the residual resistivity values in logarithmic scale. [54]

ing phase in the diagram. Applied hydrostatic pressure increases the concentration of electrons and holes in the bands and increases their overlap in energy. This reduces the possibility of Jahn-Teller instability or excitonic phase and consequently the CDW state is suppressed. Whether the appearance of superconductivity is directly related to CDW suppression is not clear.

3.5 Phase diagram of Cu_xTiSe_2

Beside hydrostatic pressure, the superconductivity can be generated in $1T$-$TiSe_2$ by intercalation of copper between $TiSe_2$ layers. Morosan *et al.* performed a complex study on polycrystalline samples of Cu_xTiSe_2 with different copper concentration x [2]. From resistivity and magnetic susceptibility measurements, they determined the transition temperatures to CDW and SC state on various samples. The resulting $T(x)$ electronic phase diagram in Fig.3.16 resembles the one obtained by Kusmartseva *et al.* for $1T$-$TiSe_2$ under pressure in Fig.3.15. With increasing copper concentration, the CDW state diminishes and from $x = 0.04$ the superconducting phase develops. The maximum critical temperature $T_c = 4.15$ K is reached at $x = 0.08$. Above this concentration, T_c decreases creating a dome in the phase diagram. Solubility limit

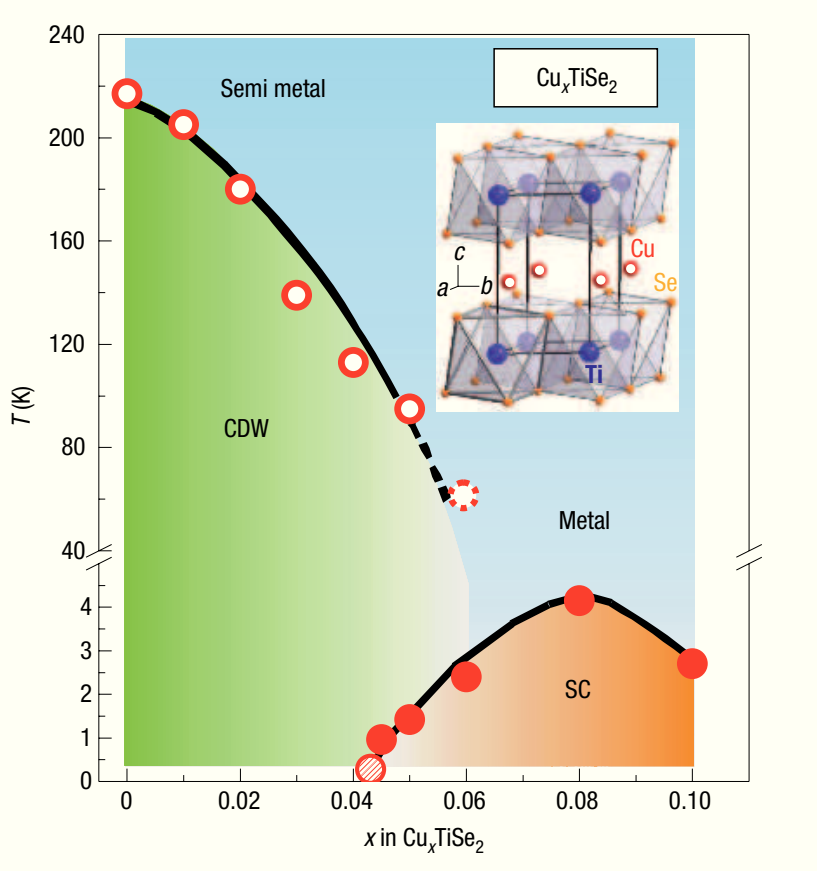

Figure 3.16: Temperature vs. copper doping electronic phase diagram of Cu_xTiSe_2. Inset: Schematic crystal structure of Cu_xTiSe_2. [2]

for copper in Cu_xTiSe_2 is reached at $x = 0.11$ when the expansion of the elementary cell stops and the lattice constants become stable. The optimal doping for superconductivity in Cu_xTiSe_2 is thus $x = 0.08$ when samples reach the maximum critical temperature. At this concentration, Morosan *et al.* did not observe the CDW state anymore, which suggested that the suppression of CDW might be related to the development of SC phase. On the other hand, some claim that the SC dome might be a direct result of the doping [55]. At first, T_c is enhanced when copper donates electrons into the conduction band but when the copper concentration is higher than $x > 0.08$, scattering effects become more relevant and T_c decreases. However, the closing of SC dome observed in pristine $1T$-$TiSe_2$ under pressure cannot be explained by such a doping-induced disorder [54].

Some relate the location of SC dome in the phase diagram of Cu_xTiSe_2 to the possible presence of quantum critical point (QCP), where a phase transition at 0 K should occur [3]. The phase diagram of TaS_3 under pressure in ref.[56] also shows sim-

ilar suppression of CDW phase and appearance of SC dome. The location of quantum critical point was determined here by extrapolation of $T_{CDW}(p)$ dependence to zero temperature. The QCP was located where superconductivity reaches maximum critical temperature. Similarly, from the phase diagram of Cu_xTiSe_2 it is tempting to expect that the $T_{CDW}(x)$ goes to zero somewhere around $x = 0.08$ and the QCP is thus located close to the optimal doping in the centre of the SC dome.

The recent experiments on Cu_xTiSe_2 by Kogar *et al.* [4], however disproved the presence of a QCP here. The group studied the commensuration of CDW state by X-ray diffraction. Figure 3.17-*Left* displays the diffraction peaks for atom lattice (Bragg peaks) and for CDW, in samples with different copper doping x. Opposite to what was previously expected, they found that the CDW state is not suppressed for higher copper doping but the CDW diffraction peaks were observed even in the sample with the highest x. The data also show that from $x > 0.05$, when superconductivity emerges in the system, a small δ shift between Bragg and CDW peaks appears, which signifies that the CDW state becomes incommensurate with the crystal lattice. The size of the shift in the reciprocal spectra corresponds to 22 unit cells. From the results of the measurements, they constructed a new phase diagram displayed in Fig.3.17-*Right*. The plot shows the incommensurate CDW phase present above the whole superconducting dome with its critical temperature T_{CDW} being al-

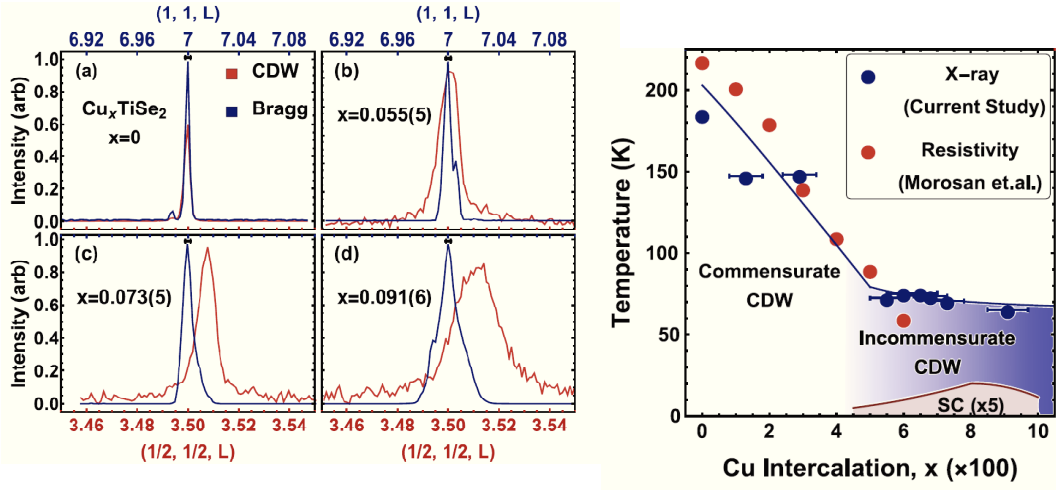

Figure 3.17: *Left* - Comparison of Bragg peaks and CDW superlattice peaks for Cu_xTiSe_2 samples with various copper doping. *Right* - Electronic phase diagram for Cu_xTiSe_2 showing the coexistence of incommensurate charge density waves state and superconductivity. [4]

most constant with copper doping. The existence of the incommensurate phase in Cu_xTiSe_2 was attributed to the presence of periodic CDW domain walls or stacking faults along the c direction (or L vector in reciprocal lattice), which are already known to cause a slight incommensurability in CDW vector in $1T$-TaS_2 [57]. In Cu_xTiSe_2, the periodicity of the structure (given by the δ shift) interestingly corresponds to the coherence length in the c direction. Together with the fact that the superconducting phase appears coincidently with incommensurate CDW phase, these results point to the relation between superconductivity and incommensurate CDW in Cu_xTiSe_2.

The effect of doping on the electronic structure is different from its response to hydrostatic pressure, even though the phase diagrams of $T(x)$ (Fig.3.16) and $T(p)$ (Fig.3.15) of Cu_xTiSe_2 and $1T$-$TiSe_2$ resemble each other. Hydrostatic pressure acts by shifting the whole electronic bands and increases their energy overlap while doping only moves the chemical potential. The ARPES experiment on pure $1T$-$TiSe_2$ [55] showed that Se $4p$ band is partially empty and Ti $3d$ band is only thermally occupied at room temperatures. Upon copper doping, electrons quickly fill the partially empty Se $4p$ band and most of the carriers are then introduced into the Ti $3d$ conduction band. The filled Se $4p$ band then lays below Fermi level and does not contribute to superconductivity [58]. This shifting of chemical potential results in the collapse of Jahn-Teller instability or the electron-hole condensate and disrupts the CDW phase.

3.6 Superconductivity in Cu_xTiSe_2

Despite its simple electronic structure, the nature of superconductivity in Cu_xTiSe_2 remains unclear. Some of the studies declare it to be a single gap s-wave superconductor while others reveal its non-trivial behaviour in superconducting state. To the first group belong the heat conductivity, κ, measurements by the group of Li *et al.* [58]. They examined a single crystal of $Cu_{0.06}TiSe_2$ from the under-doped (i.e. doping lower than optimal) region of the phase diagram yet not far from the optimal doping. The experiments were performed at temperatures as low as 50 mK allowing for the precise extrapolation of the heat conductivity $\kappa(T)$ to 0 K and determination of its residual linear term, κ_0. From the measurements in zero magnetic field, they observed that the linear term κ_0/T goes to zero, which is a clear sign of classical s-wave superconductivity with isotropic energy gap in every direction. In case of unconventional superconductors with nodes in the gap, the quasi particles from the ungapped parts of the Fermi surface contribute to heat conductivity and κ_0/T is non-zero. From the

measurements in magnetic field (see Fig.3.18), they obtained the field dependence of normalized κ_0/T in $Cu_{0.06}TiSe_2$ and compared it with similar data for the d-wave superconductor Tl2201, the clean s-wave superconductor Nb, the dirty s-wave superconducting alloy InBi and the multiband s-wave superconductor $NbSe_2$. From the comparison of the overall behaviour of these curves they concluded that $Cu_{0.06}TiSe_2$ is most likely a dirty single-gap s-wave superconductor such as InBi with exponential increase of the signal at low fields and a roughly linear behaviour at higher fields.

The heat capacity measurements by Morosan *et. al.* [2] on an optimally doped sample with highest T_c also speak in favour of conventional superconductivity. From extrapolation of temperature dependence of the heat capacity to 0 K, they obtained the value of Sommerfeld coefficient $\gamma = 4.3$ mJ mol^{-1}K^{-2}. Small γ value together with $T_c = 4.1$ K place $Cu_{0.08}TiSe_2$ among the conventional superconductors [59]. From the entropy conservation law, they determined the hight of the jump in the heat capacity at $T = T_c$ to be $\Delta C/\gamma T_c = 1.68$, which is slightly enhanced compared to 1.49 in the weak-coupling limit calculated within the BCS theory for classical s-wave superconductor.

The heat capacity measurements on Cu_xTiSe_2 samples with different doping were performed by Kačmarčík *et al.* [60]. The samples were from underdoped, through

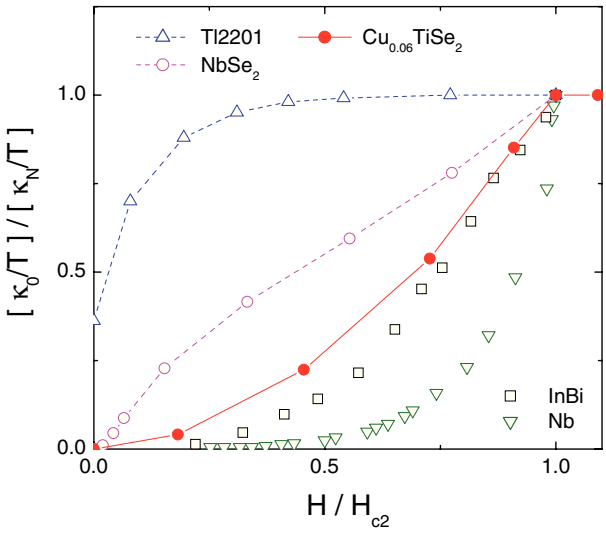

Figure 3.18: Field dependence of the normalized residual linear term of heat conductivity, κ_0/T, of $Cu_{0.06}TiSe_2$. For comparison similar data are shown for clean s-wave superconductor Nb, dirty s-wave superconducting alloy InBi, multiband s-wave superconductor $NbSe_2$ and d-wave superconductor Tl-2201. [58]

optimally doped to slightly overdoped region thus covering all parts of the phase diagram. Figure 3.19 displays the temperature dependencies of electronic heat capacity $\Delta C/T$ which is the difference of the heat capacity in superconducting C_s and normal state C_n divided by temperature, $\Delta C/T = C_s/T - C_n/T$. The plot displays the data for four samples with different copper content in a temperature scale normalized to T_c of each sample. The data are rescaled to have the same hight of the jump at the transition temperature so that it is possible to compare the behaviour of $\Delta C/T$ for different samples. The result is that all the curves follow the same behaviour without any significant differences in the overall temperature dependence meaning it is independent of copper doping. Further, from this data they extracted the information about C_{es} which is the electronic heat capacity in superconducting state. Divided by temperature T and Sommerfeld coefficient γ_n, it is displayed by the blue open circles in Fig.3.20 for one of the samples. The temperature dependence of $C_{es}/\gamma_n T$ can be described by a so-called α model based on the BCS theory with the only fitting parameter being the superconducting coupling ratio $2\Delta/k_B T_c$, where Δ is the energy gap at 0 K and k_B is the Boltzmann constant. This model can be also adjusted for two-gap or anisotropic-gap superconductor. The best agreement between the data and model was found for a single gap fit with coupling ratio $2\Delta/k_B T_c = 3.7$, which

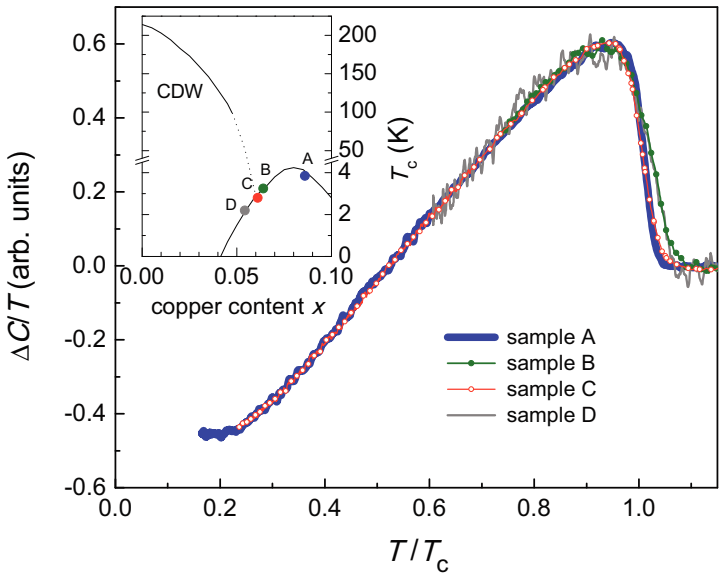

Figure 3.19: Temperature dependence of $\Delta C/T$ (see text for explanation) of four samples of Cu_xTiSe_2 with different copper doping in a temperature scale normalized to T_c of each sample. The inset shows the phase diagram obtained in ref.[2] (lines), with added four samples measured by Kačmarčík *et al.* [60] (full circles).

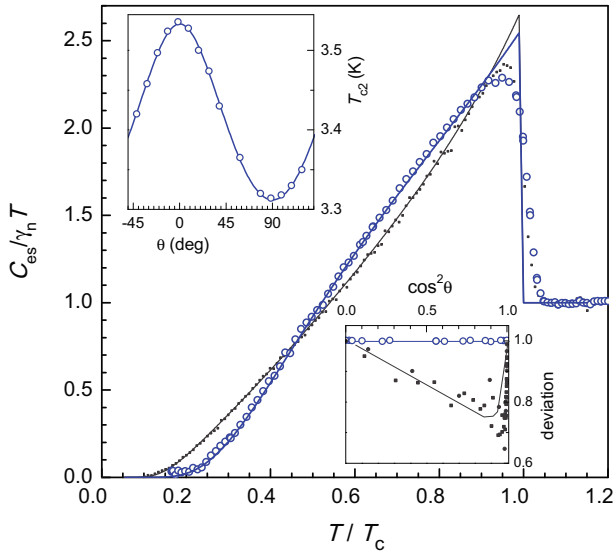

Figure 3.20: Electronic heat capacity in superconducting state for $Cu_{0.086}TiSe_2$ (blue circles) with single-gap α-model for $2\Delta/k_BT_c = 3.7$ (thick line), and data for NbS_2 (black points) [61] with corresponding two-gap model (thin line). The upper inset frame shows the angular dependence of T_c for $Cu_{0.086}TiSe_2$ (blue circles) and the lower inset its deviation function from GL anisotropic model for s-wave superconductor compared to deviation function obtained for NbS_2 (black points). [60]

is slightly higher than 3.52 calculated within the BCS theory. The figure also shows for comparison data of the two-gap superconductor NbS_2 (black solid symbols) [61]. Despite that the relative hight of the jump in the heat capacity is the same for the two materials, they differ in the overall behaviour, most significantly at the lowest temperatures. For NbS_2 the heat capacity begins to increase at lower temperatures due to the presence of smaller energy gap while higher thermal excitations are needed for quasiparticles to overcome the energy gap in Cu_xTiSe_2.

Kačmarčík *et al.* also performed the heat capacity measurements of Cu_xTiSe_2 in fixed magnetic field H at different field orientations. They determined the angular dependence of $T_{c2}(H, \theta)$ (open points in the upper inset of Fig.3.20) and compared it with the GL-model prediction for anisotropic single gap s-wave superconductor (blue curve). The data very well follow the theoretical curve and opposite to the data for NbS_2 show no deviation from the model (lower inset of Fig.3.20). From the measurements in magnetic field, they also determined the anisotropy of upper

critical field H_{c2} as the ratio of H_{c2} in field parallel with the ab planes and in the c direction, $\Gamma_{H_{c2}} = H_{c2}^{ab}/H_{c2}^{c}$. The anisotropy was found to range from 1.7 to 1.9 for different samples and to be temperature independent. This is a sign of single gap superconductivity in Cu_xTiSe_2 since the anisotropy in a multi-gap superconductor is temperature dependent (such as in MgB_2[62]).

Hillier *et al.* [63] studied close to optimally doped sample $Cu_{0.06}TiSe_2$ by muon spin rotation (μSR) permitting the direct measurement of penetration depth λ. The temperature dependence of λ can be described by a model equation for density of states 1.32 where the only parameter is again the coupling ratio $2\Delta/k_BT_c$. Hillier *et al.* found the best fit with their data for $2\Delta/k_BT_c = 2.5$, much less than 3.52 which is the lowest value given by BCS theory for the weak coupling limit. Such a small coupling ratio is found in multiple gaps systems as MgB_2 or $NbSe_2$ [12, 13], however Hillier *et al.* did not comment on that, claiming that Cu_xTiSe_2 is a single gap s-wave superconductor in the weak coupling limit.

μSR measurements on Cu_xTiSe_2 samples with different copper concentration were done also by the group of Zaberchik *et. al.* [64]. For three studied samples from underdoped to optimally doped part of the phase diagram they observed that the muon relaxation saturated at low temperatures. This indicates that the Fermi surface is fully gapped regardless of the copper doping giving s-wave character of superconductivity in Cu_xTiSe_2. Further, they determined the temperature dependence of λ and found it shows evolution with concentration x, see Fig.3.21. The $\lambda(T)$ for optimally doped sample could be described by a model curve for classical s-wave superconductor with $2\Delta/k_BT_c = 3.52$. On the other hand, the data for underdoped samples fits better with model curves with smaller coupling ratios, $2\Delta/k_BT_c = 3$ and 2.8 for sample with $x = 0.057$ and $x = 0.044$, respectively. Their μSR measurements confirmed the s-wave character of superconductivity in Cu_xTiSe_2 but point to either one anisotropic gap or multigap superconductivity evolving with copper doping.

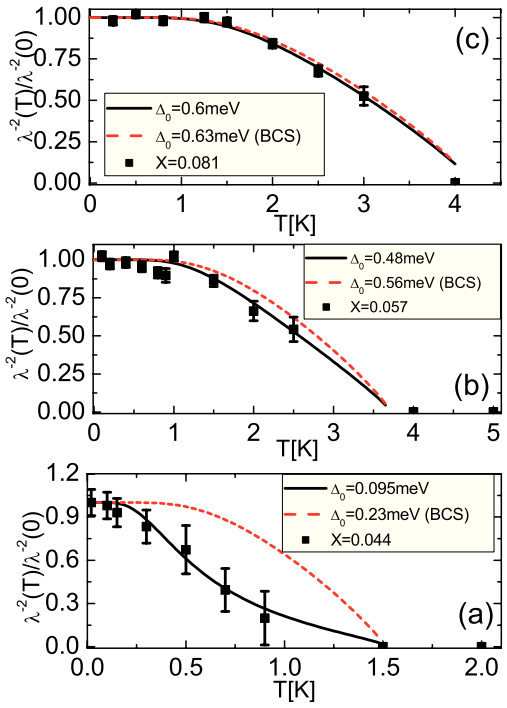

Figure 3.21: Temperature dependence of penetration depth λ for three samples of Cu_xTiSe_2 with different copper doping x. Red dashed curves represent the fit for classical s-wave superconductor and thick black lines show the best fit with the data obtained by adjusting the values of energy gaps in the model. [64]

Chapter 4

Local Hall probe magnetometry

4.1 Experiment

As was already mentioned, the magnetic field has a strong influence on superconductivity and the response of a sample to magnetic field provides an important information about its characteristic superconducting properties. The magnetic field penetrates into type II superconductors in form of vortices with quantized magnetic flux. These objects can experience various interactions within the sample. Therefore their distribution in general is not homogeneous and just to measure the average value of induction in a sample is not sufficient. Bulk magnetisation measurements on superconductors therefore lead to significant under- or overestimation of the parameters characterizing their properties. Local magnetic field measurements are therefore necessary to determine correctly properties of superconductor in a magnetic field.

Local Hall probe magnetometry uses miniature Hall probes situated in close proximity to the sample. If there exists a non-zero magnetic field normal to the probe surface H, then when we apply a current I, a Hall voltage V_{Hall} is generated across the probe perpendicular to I. The size of V_{Hall} depends only on the current we apply and the local magnetic field. An important parameter characterising a Hall probe is its sensitivity s defined as $s = \Delta V_{Hall}/(I\mu_0\Delta H) = [\Omega/\mathrm{T}]$, where ΔV_{Hall} is the change in the Hall voltage induced in the probe by a change in the local magnetic field ΔH. To be able to use a Hall probe in an experiment, it is important that the dependence of the Hall voltage on magnetic field is a linear function meaning that the sensitivity is field independent. In that case, it is possible to directly relate the measured Hall voltage to local magnetic field through the coefficient s.

Sensitivity depends on the number of charge carriers but their mobility is an im-

portant parameter for the low temperature measurements. Small carrier mobility causes high resistance, which is proportional to the power dissipation during the measurements. As the experiments are performed at low temperatures in vacuum, the cooling power is not very large and even a small dissipated energy can cause overheating. Possible consequences could be incorrect determination of sample temperature, damaging of the delicate wiring or malfunctioning of the experimental set-up. The power can be reduced by using of small electrical current for the measurement but this leads to the decrease of the signal amplitude. We used Hall probes patterned into an epitaxial heterostructure of GaAs/AlGaAs, which is a 2D electron gas material with high electron mobility. The Hall probes were manufactured in the group of Dr. Vladimír Cambel at the Institute of Electrical Engineering, SAS in Bratislava. Their sensitivity was around $\sim 1000\ \Omega/\mathrm{T}$, constant for the range of magnetic fields we used for measurements, changing less than 2% up to 1000 G.

In the experiments, we used a line of 7 Hall probes, each with the active area of $10 \times 10\ \mu\mathrm{m}^2$ (a scheme shown in Fig.4.22-*Left*). Depending on the used line of probes, the distance between the centres of neighbouring probes was either 25 or 35 μm. The sensitivity was slightly changing from probe to probe, with temperature and time, therefore it was important to determine s for each measurement. To record a response of the studied superconductor to applied magnetic field, the sample was placed on top of the Hall probes and cooled down in zero magnetic field. Then we applied an external field H_a and recorded the Hall voltage on every probe. The external field was generated by a superconducting horizontal coil magnet, which allows us to perform the measurements for different orientations of magnetic field simply by turning the probe. The measured signal $V_{Hall}(H_a)$ was converted to magnetic induction B through the

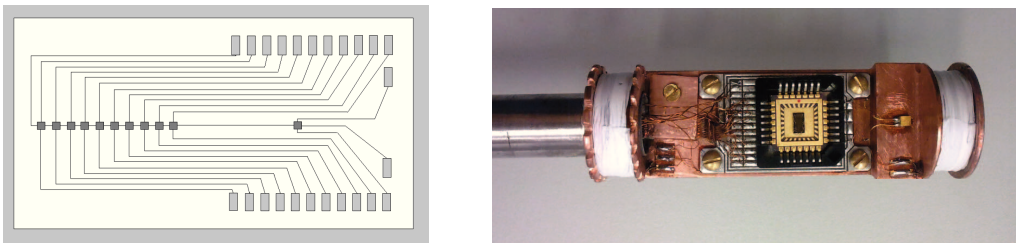

Figure 4.22: *Left* - Scheme of the line of 10 Hall probes (small squares) evenly distributed along the line and contacts used for passing current and for Hall voltage measurement. *Right* - The Hall probes with a sample placed above is inserted into the black chip matrix built in a probe used for low temperature measurements.

probe sensitivity and current I passing through the probe, $B(H_a) = V_{Hall}(H_a)/(Is)$.

An example of a field dependence of a signal measured on the probe below the superconducting sample, $V_{Hall}(H_a)$, is shown in Fig.4.23. At first, the field was increased from 0 G to ~ 40 G and the signal was recorded. At zero magnetic field, one would expect that $V_{Hall} = 0$ but the Hall voltage measurements are always accompanied by an offset on the order of millivolts. This non-zero offset might be caused by a small misalignment of the contacts on the probe through which we measure the Hall voltage. For the smallest applied fields, the superconducting sample is in the Meissner state. The magnetic induction in the sample is zero but the V_{Hall} signal as measured, shows a small increase with the applied field. This is caused by the non-zero distance between the probe and the sample, when certain portion of the applied field is picked up by the Hall probe. The signal we obtain is not given just by the field induction in the sample but depends also on the relative position of the probe to the sample. The shielding of magnetic field is most effective on the Hall probe that is located close to centre of the sample (see probe on position 1 in Fig.4.24), therefore large part of the V_{Hall} signal comes from the field induction and by removing the first linear increase from the data, we do not not introduce notable error. For Hall probes located further from the centre, the shielding by the sample is less effective (position of the Hall probe

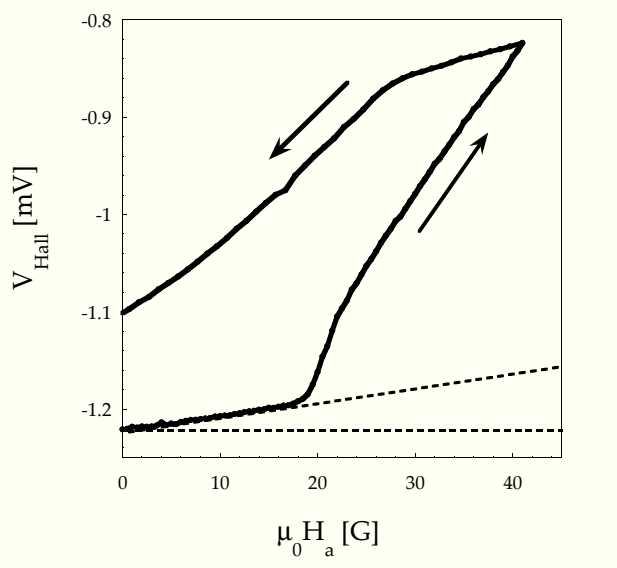

Figure 4.23: Field dependence of V_{Hall} measured at the Hall probe below a superconducting sample, through the contacts perpendicular to current $I = 50$ μA passing through the probe. The signal shows an offset at $H_a = 0$ and a small linear increase in the signal where we expect to observe the Meissner state.

2 in Fig.4.24). Removing the linear slope from the data, means removing a large part of the signal, which introduces significant error. For a quantitative analysis, we should therefore only use probes located close to the sample centre where the shielding of the external field is substantial. Even though the slope removing from the data obtained closer to the edges introduces error, they can still be used for a qualitative analysis.

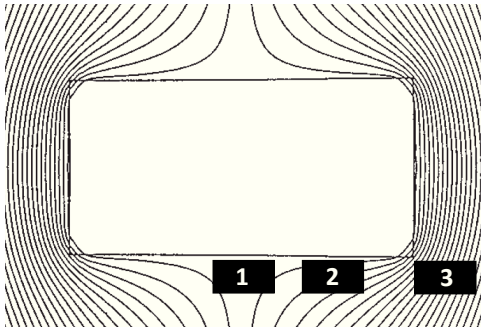

Figure 4.24: Scheme of the superconductor in a magnetic field with the Hall probes measuring the field induction in the sample.

Data in Fig.4.23 were measured on the probe in the centre of the sample. The offset was accounted for and the signal was recalculated through the probe sensitivity to field induction. After the subtraction of the linear slope, we get the $B(H_a)$ curve shown in Fig.4.25, which now displays zero signal at low magnetic fields. When the applied field reaches the value of penetration field H_p, first magnetic flux starts to enter into the superconductor. The Hall probe below the sample senses the magnetic field from the vortices and a sharp increase appears in the $B(H_a)$ signal. From the active area of the probe S, we can recalculate how much of magnetic flux passes through the probe ($\phi = B \cdot S$) and since each vortex contains exactly one quantum of magnetic flux, $\phi_0 = 2.0678 \cdot 10^{-15}$ Tm^2, B can be directly related to the number of vortices recorded by the probe, $N = \phi/\phi_0$. The increase of 1 G in B signal measured by the probe with $S = 100$ μm^2 is equivalent to 5 vortices. With increasing magnetic field more and more vortices enter the sample until at the upper critical field H_{c2} the superconductor passes to the normal state. Then the induction in the sample equals to the applied field and the $B_(H_a)$ curve in Fig.4.25 will merge with the straight line showing $B = H_a$ signal.

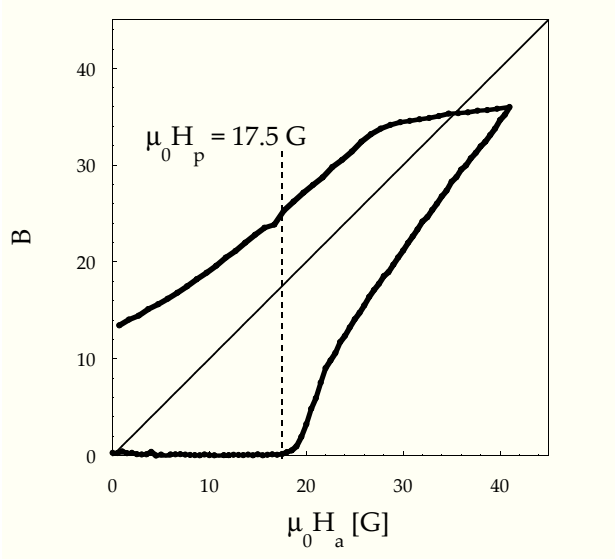

Figure 4.25: Black curve shows the data from Fig.4.23 after removing the first linear increase. Thin black line represents the signal $B = \mu_0 H_a$.

4.1.1 Demagnetisation effects

For the measurements in low magnetic fields, the demagnetisation effects have to be always taken into account. When a superconductor is in the Meissner state, it repels the magnetic field from its interior and the field lines deform around the sample. This deformation causes that the field at the sample surface has higher value than the applied field, $H > H_a$. The case of an ellipsoid sample in magnetic field is displayed in Fig.4.26. In this case, the deformation of field lines around the sample is uniform and the field at the surface can be calculated as the sum of applied field and

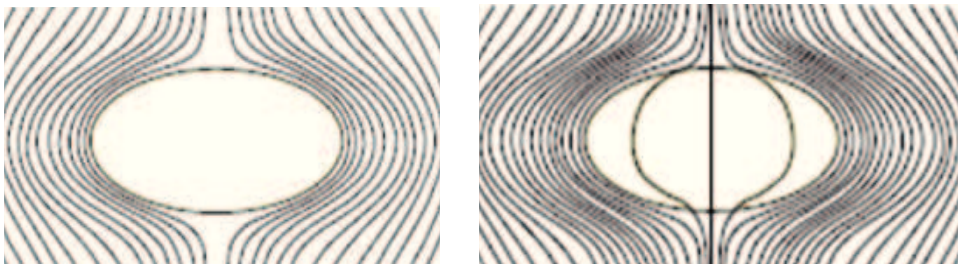

Figure 4.26: Magnetic field lines deform around a superconducting sample in Meissner state. For elliptical cross-section the deformation is homogeneous and the field at the surface has the same value everywhere (*Left*). When field at the sample surface reaches critical value, vortices start to enter into the superconductor (*Right*).

demagnetisation field:

$$H = H_a + H_d, \tag{4.1}$$

where $H_d = -NM$, with N being the demagnetisation factor ranging from 0 to 1 depending on dimensions of the ellipsoid, and M is the magnetisation, which in Meissner state equals to $M = -H$. When magnetic field at the sample surface reaches the value of lower critical field, $H = H_{c1}$, vortices start to enter into the superconductor (Fig.4.26-*Right*). At this point, the value of applied field is taken to be the so-called penetration field, H_p, and $M = -H_{c1}$. From $H = H_a + H_d$ we then obtain the relation between the penetration field H_p and the lower critical field H_{c1} by

$$H_{c1} = H_p + NH_{c1}$$

$$H_{c1} = \frac{H_p}{1-N}. \tag{4.2}$$

4.1.2 Geometrical barriers

Deformation of magnetic field around the sample is homogeneous only for an ellipsoid or a sphere. Real samples never have such an ideal shape but in many cases it might be well approximated to these two ideal types. However, the case of samples with rectangular cross-section with corners is more complicated as the field deformation around the sample varies a lot at the surface. The deformation of field lines is most significant at the corners of the rectangular cross-section. Here the field at the surface reaches the critical value of H_{c1} first and tilted field lines start to enter into the

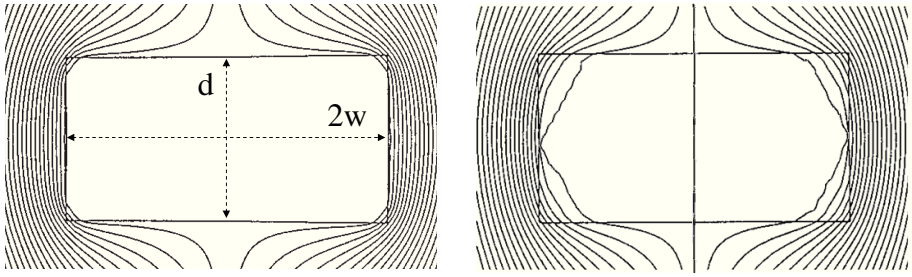

Figure 4.27: Magnetic field lines deforming around the sample with rectangular cross section in Meissner state (*Left*). Field penetrates first through the sample corners where the deformation is highest. With field increased to $H_a = H_p$, the areas at the corners where field is present merge and the first vortex enters the sample (*Right*). [65]

superconductor through the corners (Fig.4.27-*Left*). With increasing field, the tilted vortices spread further from the corners to the sample centre and equatorial part. When the top and bottom regions of the tilted vortices meet in the middle of the sample edge, the first whole vortex finally enters the sample (see Fig.4.27-*Right*). This is the value of applied field which should be taken for the penetration field H_p. The corners of the sample thus serve as the geometrical barrier for vortices to enter into the sample. Zeldov *et al.*[66] and Brandt [65] studied this special case in detail and found that H_p can be then related to H_{c1} as

$$H_{c1} = \frac{H_p}{\tanh\sqrt{\beta\dfrac{d}{2w}}}, \tag{4.3}$$

where $d/2w$ is the thickness over width ratio of the sample cross-section (see Fig.4.27-*Left*) and parameter β is ranging from 0.36 if the third sample dimension is much bigger than d or $2w$, to $\beta = 0.67$ if the sample shape resembles a flat disk [65]. The two cases of ellipsoid and sample with rectangular cross-section are quite different and neglecting of the geometrical barriers leads to high overestimation of H_{c1} what is more significant for samples with $d/2w << 1$ (see Fig.4.28).

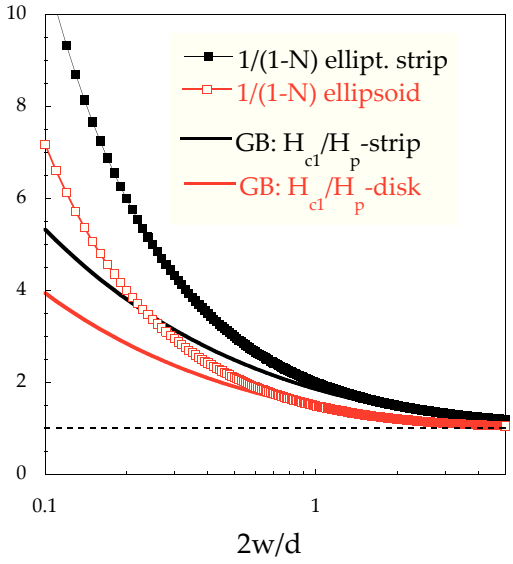

Figure 4.28: The corrections of H_{c1}/H_p depending on the thickness to width of the cross-section ratio, $d/2w$, for an ellipsoid (red open squares), infinite sample with rectangular cross-section, compared to corrections for geometrical barriers for a long strip (black curve) and a short disk (red curve).

4.2 Field profiles

The fixed position of Hall probes in line enables us to study the distribution of magnetic field in the superconducting sample. Fig.4.29 displays an examples of $B(H_a)$ signals obtained from each probe in the line, on positions numbered from 1 to 7. Probes located below the sample show screening of the applied magnetic field (positions 3 to 7) while probes situated outside the sample (positions 1 and 2) display higher B signal than the applied field (represented by the dashed black curve). This is caused by the deformation of field lines around the superconducting sample due to which they become more densely distributed and the field close to the sample has effectively higher value than H_a (see position 3 in Fig.4.24).

From $B(H_a)$ curves taken at different positions below the sample, we can construct one dimensional profile of magnetic field in the sample at certain applied field. In these measurements, the pitch between two probes was 35 μm, thus the probe position in the line, X, gives us the relative length scale in the multiple of 35 μm. To construct a field profile, $B(X)$, for certain applied field, we take the value of B at the chosen

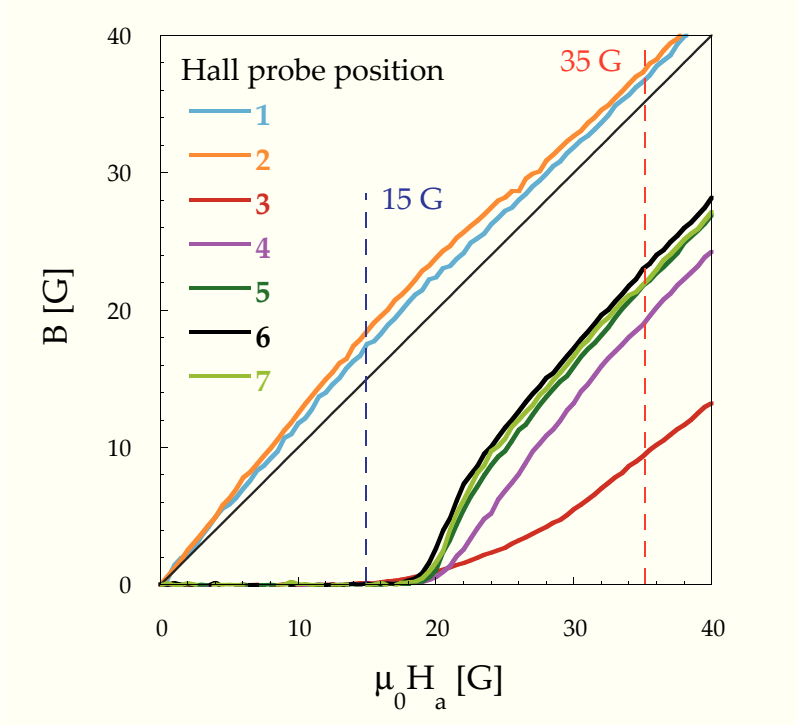

Figure 4.29: Field dependencies of induction B measured at 7 Hall probes seated next to each other. Probes on positions 1 and 2 were located outside the superconducting sample, while probes 3 to 7 lied below it.

H_a from measurement on each Hall probe in the line. As an example, two profiles at different applied fields are shown in Fig.4.30. Blue colour data correspond to $\mu_0 H_a = 15$ G, while red points were taken at $\mu_0 H_a = 35$ G. At 15 G, the sample is still in the Meissner state and only probes 1 and 2 outside the sample show presence of the magnetic field. The second profile was constructed for applied field 35 G, a field higher than H_p, and the superconducting vortices are already present in the sample causing non-zero signals on the positions 3 to 7. This profile reveals that the vortices concentrate in the centre of the sample as the signal is increasing going further from the edge to its centre, from position 3 moving to positions 6 and 7 located at the centre of the sample.

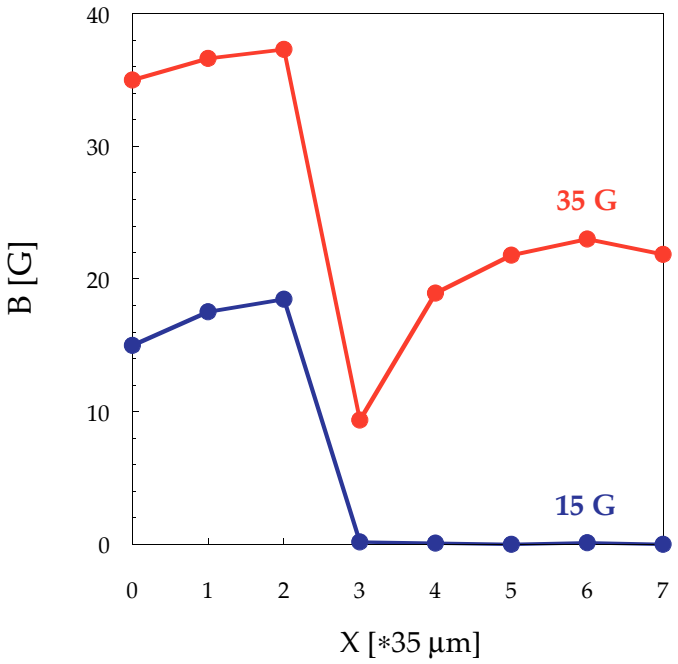

Figure 4.30: Field profiles at 15 and 35 G constructed from the data in Fig.4.29. X defines the Hall probe position in the line and gives us the length scale in the multiple of 35 μm.

Sometimes the measured sample is bigger than the line of the Hall probes, as was also this case. To obtain a full profile, we have to shift the sample along the line and record partial profiles at different sample versus probes positions. The complete profile through the whole sample is then obtained by superimposing all the partial measurements. An example of complete field profiles through the whole sample is shown in Fig.4.31. As three overlapping partial profiles were used to construct it, some of the Hall probe positions are no longer integer numbers.

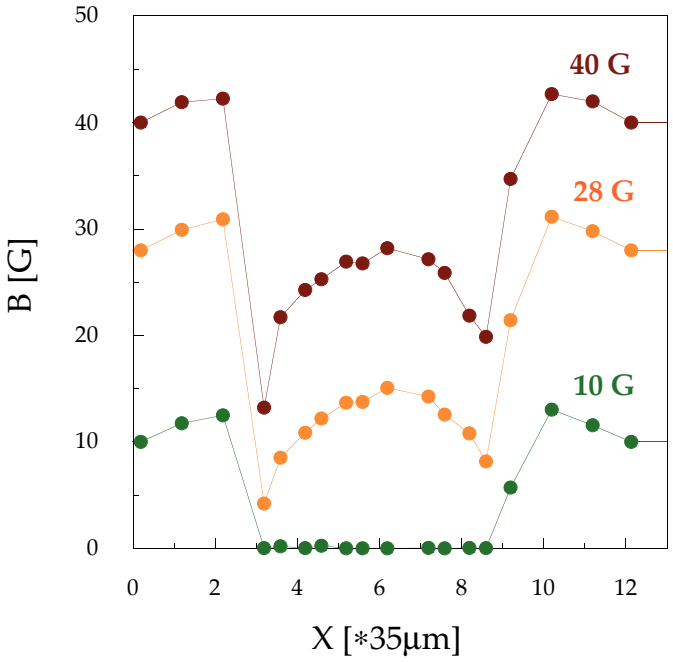

Figure 4.31: Field profiles $B(X)$ of magnetic field in the sample and around for applied field 10, 28 and 40 G. Full dots represent the measured data and thin lines are guidelines to the eyes.

4.2.1 Effect of pinning on field profiles

The shape of the field profile gives us primarily information about the place where the first vortices in the sample accumulate, which is the correct location to measure the penetration field H_p. There are two main possible shapes of the field profiles depending of the pinning present in the sample. A pinning centre might be an impurity or a defect in the structure where superconductivity is at least partially suppressed and vortex interactions with it is attractive. Vortex entering sample is repelled from the surface, therefore if there are no pinning sites in the sample, the vortex jumps to sample centre. Following vortices also accumulate in the centre, which results into the dome shape of field profile (e.g. Fig.4.31). If on the other hand, the pinning in the sample is strong, as soon as vortices enter the sample they get pinned, which stops them from further propagation. With higher applied field, more vortices enter the sample and get trapped on pinning sites. This way vortices finally reach also the centre of the sample and the resulting field profile will have the shape of the letter "V" (e.g. Fig.4.32). This way the field profile gives us qualitative information about the pinning in the sample and help us to detect the first vortices in the sample, which

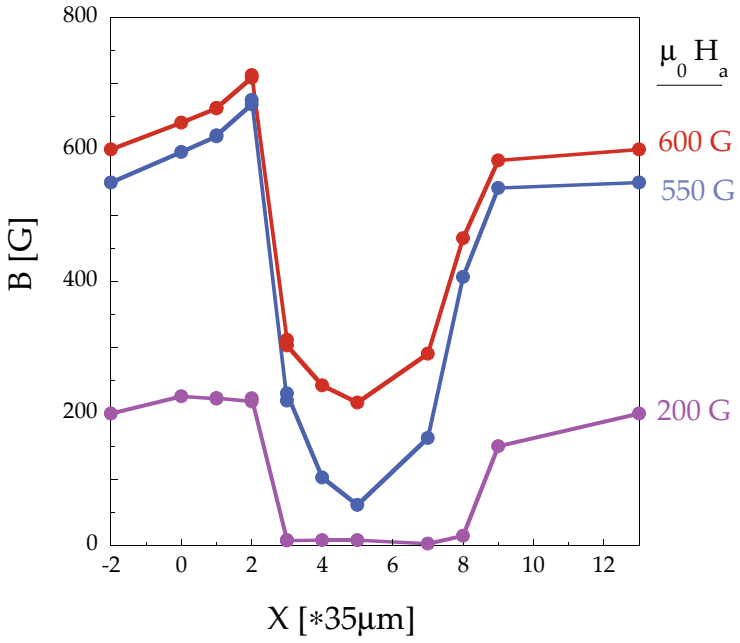

Figure 4.32: Example of "V" shaped field profiles $B(X)$ at different applied fields obtained from measurements on superconducting sample. Hall probes on positions from $X = -3$ to $X \sim 8$ are located below the sample.

is in the centre for low pinning samples and close to the edge for samples with the "V" shape profile where pinning is stronger.

4.2.2 Geometrical versus Bean-Livingston barriers

The vortex penetration into the sample can be also affected by its interaction with the surface. C. P. Bean and J. D. Livingston discovered that the sample surface itself may act as a pinning site and create a barrier preventing vortex entrance into the sample [67]. The screening super-current always flows tangential to the surface and its normal component has to be zero. To fulfil this condition during the vortex entry, we can imagine that a virtual vortex appears outside the sample with opposite circulation (Fig.4.33). As a result, the real vortex is attracted to its mirror image and is prevented from entering the sample. The smoother is the surface of the sample, the clearer is the mirror image and the stronger would be this so-called Bean-Livingston barrier (BLB). If however the roughness of the surface is comparable with the penetration depth λ, then the image is blurred and BLB becomes irrelevant. Bean and Livingston found that the vortex overcomes the surface barrier only when the magnetic field reaches

the thermodynamic critical field H_c. Thus the measured penetration field H_p is not related to H_{c1} but to H_c.

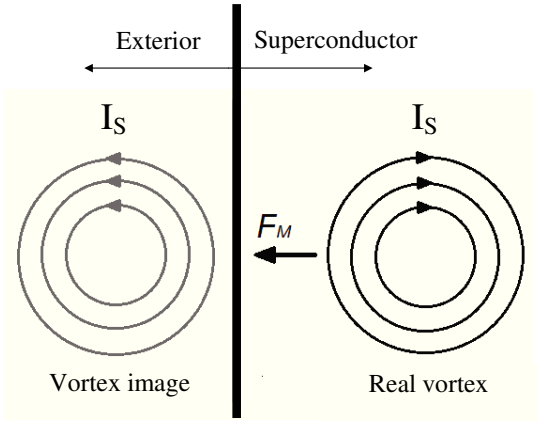

Figure 4.33: Schematic view of Bean-Livingston barrier as an antivortex appearing above the sample surface when a real vortex enters the sample.

It is therefore necessary to know whether the BLB plays a significant role in the vortex penetration into the sample or they can be neglected, otherwise we do not know whether H_p can be related to H_{c1} or to H_c. Brandt *et al.* in [68] considered two distinct cases. If the surface BLB is negligible, vortices overcome it already at small fields and when field at the surface reaches H_{c1}, the process will continue as expected for geometrical barriers. The magnetic field penetrates at first the corners of the sample and later the first vortex jumps into its centre. If however the BLB is strong, magnetic field cannot enter the sample through the corners until it reaches the value of H_c, which is much higher than H_{c1}. At H_c the geometrical barriers are already overcome and the vortex would directly jump into the centre of the sample. The main difference between these two scenarios thus is, whether the field appears at the corners before the vortex jumps into the sample centre or not. The detailed look on the field profiles give us the answer to this question.

Chapter 5

Critical fields in Cu_xTiSe_2

In the following chapter, I present and discuss our results of local Hall probe magnetometry measurements on different Cu_xTiSe_2 samples. The first part of this chapter concerns the study of field profiles obtained on three different samples. In the second part, I analyse the temperature dependence of lower critical field. The last part of this chapter contains a study of evolution of critical fields with the critical temperature T_c in Cu_xTiSe_2 and consistency checks of different experimental techniques. In this chapter, all of our measurements were performed in magnetic field oriented parallel with the c direction of the samples.

The studied samples were single crystals of Cu_xTiSe_2 with different copper content, x, which was determined by energy dispersive X-ray spectroscopy (EDX). The critical temperatures of superconducting transition, T_c, were obtained from the heat capacity measurements. The specific values of x and T_c for each sample are displayed in Fig.5.34 [69], constructed on the bases of the phase diagram by Morosan *et al.* [2]. The studied samples were from underdoped to overdoped region ($0.04 < x < 0.1$), thus allowing us to study the superconducting state in Cu_xTiSe_2 over a large part of the superconducting dome. The samples were prepared by the iodine gas transport method [70] by three different research groups. Samples A, B, C and D were prepared in the group of Dr. Goran Karapetrov from Drexel University in Philadelphia, samples E and F by Dr. Helmuth Berger from Ecole Polytechnique Fédérale in Lausanne, and sample F was grown by Dr. Florence Lévy-Bertrand and Bastien Michon from Institute Néel in Grenoble.

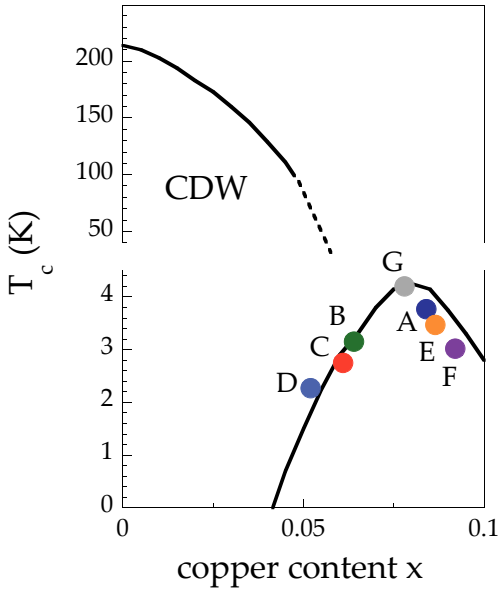

x	Label	T_c (K)
0.052	D	2.3
0.061	C	2.8
0.064	B	3.2
0.075	G	4.1
0.084	A	3.8
0.086	E	3.5
0.092	F	3.0

Figure 5.34: *Left* - Phase diagram of Cu_xTiSe_2 showing critical temperatures of transition to superconducting state T_c and copper content x of samples studied in this work (coloured full circles) [69]. Thick black lines represent results obtained by Morosan *et al.* in [2]. *Right* - Table summarizing the obtained x and T_c values for all the samples.

5.1 Field profiles

At first, I present the profiles of magnetic field obtained from measurements on three selected samples. The field profiles are necessary for correct determination of the lower critical field value H_{c1} (see also chapter 4).

5.1.1 Sample B - model by Zeldov

Sample B is of a platelet-like shape, with length, width and hight of $250\times250\times50$ μm^3. Fig.5.35-*Top* displays its scanning electron microscope (SEM) image and the red line represents the site along which we obtained the field profiles. The sample had to be shifted three times along the Hall probe line to obtain the whole profile. The temperature at which we measured was 1.6 K, which is about 50% of the critical temperature. The construction of the field profiles was explained in the previous chapter and this sample was used as an example. Now let us concentrate on the shape of the profiles displayed in Fig.5.35. The centre of the sample is located at the position $X = 0$ and its edges lie close to $X = -3$ and $X = 3$. The first linear slope

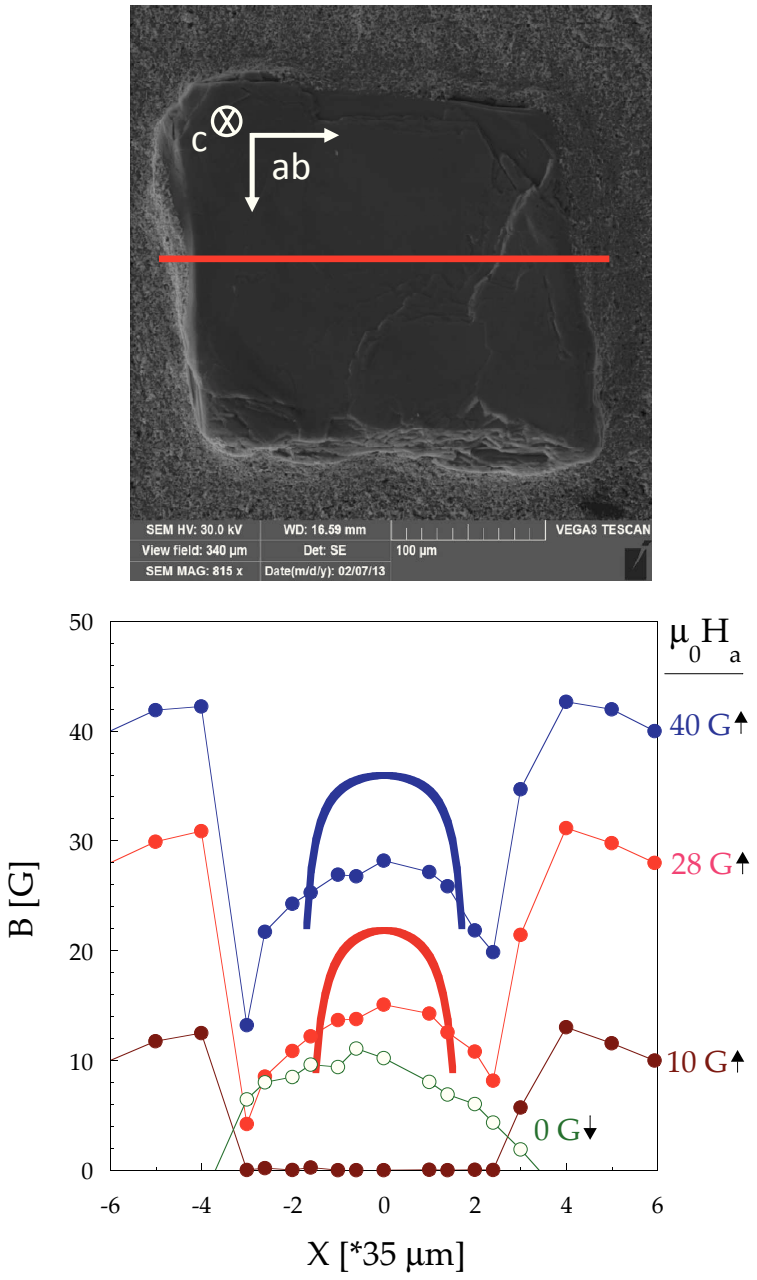

Figure 5.35: *Top* - SEM image of the sample B with the red line showing the site along which the field profiles were measured. *Bottom* - Field profiles $B(X)$ of $Cu_{0.064}TiSe_2$ (sample B). The full circles display data measured in increasing applied magnetic field, while the open circles show data obtained when the field was decreased back to zero. Thin lines connecting the points are shown just to guide the eye. Thick lines show the expected flux in the sample calculated from model by Zeldov *et. al* [66] for samples with geometrical barriers and no pinning.

was removed from the data measured at positions -2 to 2 but not close to the sample edges at positions -3 and 3, where it would introduce significant errors (see discussion in chapter 4). For the lowest magnetic fields, the sample was in the Meissner state and the magnetic field was shielded from the probes below the sample. For $H_a > 17.5$ G, which was H_p in this case, vortices concentrate in the centre and the overall shape of the profiles is a dome growing with increasing applied field. As was mentioned in chapter 4, dome shape of the field profiles is a sign that the pinning in the sample is small.

The sample B has a rectangular cross-section. In such a case the geometrical barriers play an important role for vortex penetration into the sample and therefore, we decided to describe it by the model by Zeldov *et. al* [66] for samples with no pinning and geometrical barriers. With the use of model, knowing the dimensions of the sample and the penetration field H_p, one can estimate magnetic flux density inside the sample $B(X)$ for any given value of applied field H_a:

$$B(X) = H_a \sqrt{\frac{b^2 - X^2}{w^2 - X^2}},$$

where

$$b = w \sqrt{1 - \left(\frac{H_p}{H_a}\right)^2}, \tag{5.1}$$

where w is the half of the sample length and X goes from $-w$ to w, being $X = 0$ in the sample centre. When we constructed the model curves, we found that the flux density in the centre of the dome is expected to be higher than what we obtained from the measurements. Also the model curves were concentrated more in the centre while we obtained a dome spreading across the whole sample. The main reason for this discrepancy is a finite but small pinning present in the sample, while model accounts for zero pinning. As some of the vortices get pinned in the sample, they cannot propagate into its centre, which results into smaller height of the dome and wider dome shape (for profiles at different applied field at sample B see ref.[71]). The non-zero pinning in the sample is confirmed also by the profile obtained when the field was decreased back to 0 G (open circles profile in Fig.5.35-*Bottom*). It clearly shows that some of the vortices remained trapped in the sample. The remanent value of about 10 G, taken from the probe in the centre, over half of the sample width 125 μm, corresponds to the critical current density of ~ 650 A/cm^2, which is a value similar to what was obtained in high quality single crystals of MgB_2 [72].

5.1.2 Sample E - Geometrical barriers vs. Bean-Livingston barrier

In the previous case it was assumed that geometrical barriers are important for vortex entry but we did not exclude the Bean-Livingston barriers. As was already mentioned in the previous chapter, section 4.2.2, according to Brandt *et al.* in [68] from the field profiles it can be determined whether the geometrical barriers or Bean-Livingston barrier play more significant role in vortex penetration into the sample. If we observe magnetic field at the sample edges before appearance of a dome in the centre then geometrical barriers prevail and H_p we measure is related to H_{c1}. In the next part of the chapter, I present the measurements on sample E where we also analysed the vortex distribution close to the sample edges.

Sample E, with its copper concentration x=0.086 and critical temperature T_c = 3.5 K, is from the overdoped part of the phase diagram. Its length and width are 400×1000 μm^2 but its thickness is varying from ≈ 50 μm at the left side to ≈ 30 μm at the right edge of the sample. The complete field profiles through the sample E were constructed from three partial profiles across the sample. The first linear slope was subtracted from $B(H_a)$ data measured on all of the Hall probes located below the sample. As was mentioned in the previous chapter, removing of the slope introduces quantitative error into the data if done on probes located further from the sample centre, however we can still qualitatively analyse the data and study the vortex distribution close to the sample edges.

The field profiles are displayed in Fig.5.36-*Top*. For smallest applied field (e.g. see the profile for 10 G), the sample shielded the magnetic field from its interior and from the Hall probes on the positions 4 to 14 below the sample. When field exceeds certain critical value, a dome, similar to the one observed in sample B, appears in the field distribution $B(X)$. However, in this sample the maximum of the dome is slightly shifted from the centre of the sample to the right side, to position $X = 11$. This is caused by the thickness variation, as the right side of the sample is slightly thinner than the left side. The difference in thickness leads to a non-uniform distribution of Meissner currents around the sample, therefore the equilibrium position for vortices inside the sample shifts to the right part of the sample.

The field profiles also show that at the sample edges (positions 4, 5 and 14), non-zero B appears even before the formation of the dome in the sample. If we compare the $B(H_a)$ data from the individual probes displayed in Fig.5.36-*Bottom*, we see that

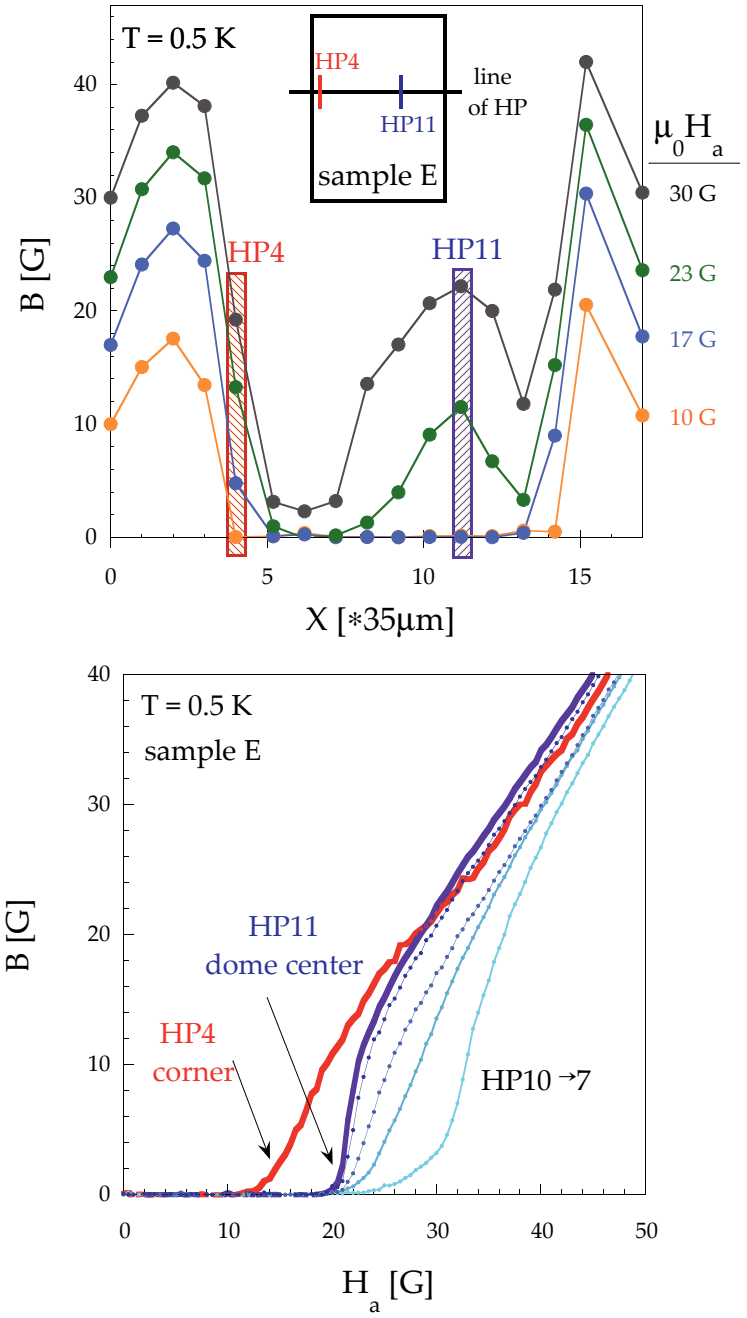

Figure 5.36: *Top* - Magnetic field profiles measured at $T = 0.5$ K in and around sample E for an increasing field. Red and blue box mark the evolution of B signal close to the edge (HP4) and at the centre of the dome (HP11). *Inset* - Sketch of the probe position relative to the sample. *Bottom* - $B(H_a)$ dependencies measured by probes at different positions below the sample at $T = 0.5$ K. Red thick line was measured close to the sample edge and thick blue curve was obtained on the probe located at the centre of the dome in the field profile (see the red and blue box positions in the *Top* figure).[69]

the increase in $B(H_a)$ signal begins at Hall probe close to the sample edge (HP4) sooner than on the probe where the maximum of the dome is located (HP11). This is the partial field penetration through the corners of the sample, which proves that the Bean-Livingston barriers are negligible in the sample. Therefore, the first penetration field in the sample determined at the probe located below the maximum of the dome at position 11, can be related through eq.4.3 to the lower critical field H_{c1}.

5.1.3 Sample A with surface irregularity

At last, I present here the magnetic field profiles measured on sample A with $x = 0.084$. A sharp step-like defect can be observed at the top right part of the sample surface, see its SEM image in Fig.5.37. The dimensions of the sample are $\sim 500 \times 500$ μm^2 with the thickness on the top edge of the sample being 35 μm and 50 μm at the bottom edge. At first, we constructed the field profiles crossing this step along the red line P1 displayed in Fig.5.37. Due to the sample dimensions, 6 partial measurements were needed to cover the whole sample. The resulting profiles are not a single dome shaped but resemble combination of two domes of different heights. At first, a dome is created in the right part of the sample (see pale blue profile in Fig.5.38). With increasing field, another smaller dome starts to shape in the left part of the sample

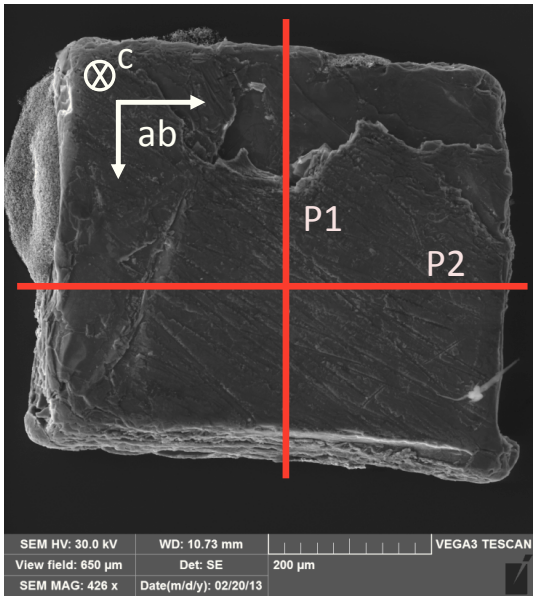

Figure 5.37: SEM image of sample A with a sharp step visible in the top right part of the sample surface. Red lines represent the positions of two sets of field profiles measured on this sample.

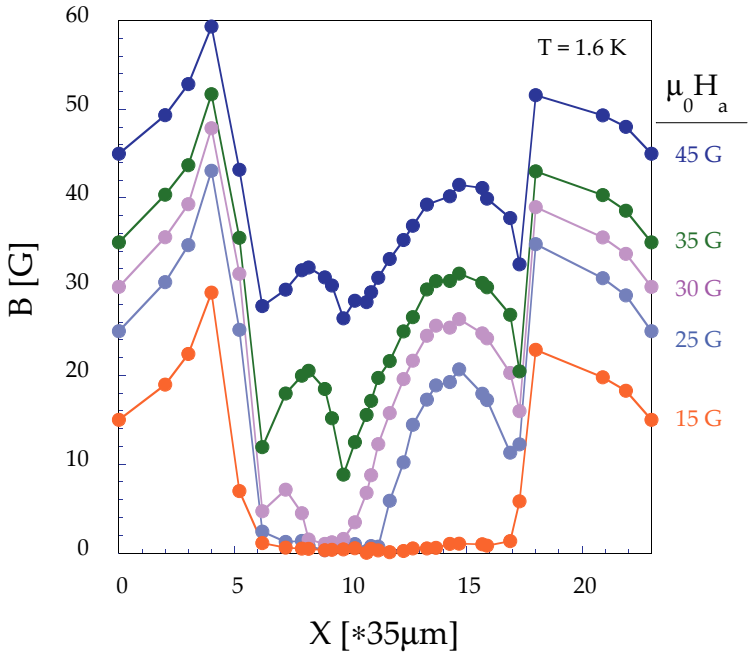

Figure 5.38: Magnetic field profiles measured on sample A at $T = 1.6$ K in different increasing applied magnetic fields.

(see green profile in Fig.5.38). The two dome shape can be related to the sharp step at the sample surface, which acts as a barrier preventing vortices to move further into the centre. The uneven thickness of the sample also causes that the field penetrates into to sample sooner at the thinner right part where the field lines are more deformed. Vortices entering the sample cannot pass through the step barrier, so they create a dome in the right part of the sample. With increasing applied field, vortices start to penetrate also through the left edge of the sample, forming a dome in the left part of the sample.

To prove that the double-dome shape of the profiles is really connected to the surface irregularity, we constructed another profile on the same sample, this time along the line far from the location of the step, indicated as P2 in Fig.5.37. The resulting profiles displayed in Fig.5.39 have again the dome-shape proving that the surface defect acts as a large barrier for vortex propagation. H_p values for this sample were then measured at the centre of the dome at $X = 10$ at the line position P2.

The field profiles were constructed for all of the studied single crystals of Cu_xTiSe_2. We found that the pinning in the samples is small proving their high quality and further analysis of the profiles showed that the vortex penetration processes are dominated by the geometrical barriers. For each of the studied samples, we determined

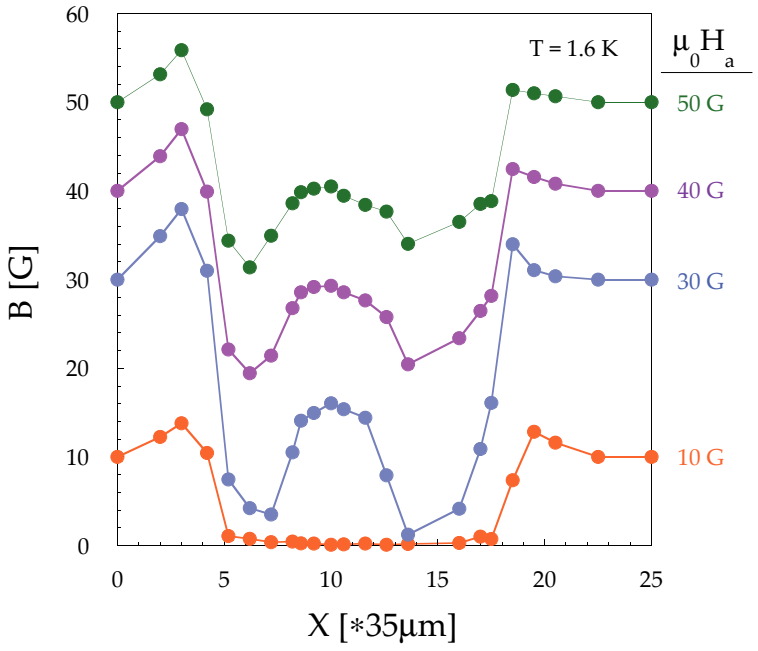

Figure 5.39: Magnetic field profiles in sample E, measured at the site given by red line P2 in Fig.5.37 at $T = 1.6$ K.

the correct location to measure H_p, which was always in close proximity of the sample centre.

5.2 Temperature dependence

After we had properly analysed the field profiles, we performed the measurements at different temperatures. Before each measurement the sample was cooled down in zero magnetic field to a given temperature. Then the applied magnetic field was increased to certain maximum value and decreased back to 0 G. Figure 5.40 displays an example of the $B(H_a)$ curves measured at selected temperatures on sample E. The data were obtained on the Hall probe on position 11 in the field profile displayed in Fig.5.36, where the maximum of the dome was located. The initial linear slope, caused by non-zero distance between sample and Hall probe, was removed before further analysis (see discussion in section 4.1). From the $B(H_a)$ curves taken at different temperatures, we determined the value of penetration field and obtained the temperature dependence of $H_p(T)$.

The behaviour of $H_p(T)$ on six samples of Cu_xTiSe_2 with different copper doping is compared in Fig.5.41. $H_p(T)$ dependencies displayed here are normalized to $H_p(0)$,

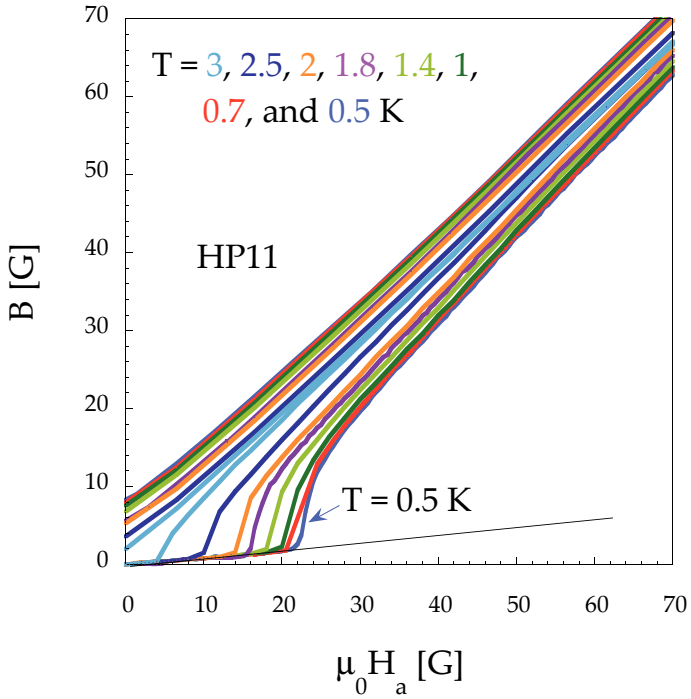

Figure 5.40: Magnetic field dependencies of induction B measured on sample E at the indicated temperatures. $B(H_a, T)$ were obtained on a Hall probe with location $X = 11$ where the maximum of the dome in the field profile was found (see field profiles in Fig.5.36). [69]

which is the value of penetration field extrapolated to 0 K. The temperature scale on horizontal axis is also normalized to the value of the critical temperature. In this scaling, we compared $H_p(T)/H_p(0)$ for all of the samples and found that they follow the same behaviour over the whole temperature range independent of the copper doping in Cu_xTiSe_2.

Due to the geometrical barriers, H_p can be recalculated to H_{c1} through a factor depending only on the sample geometry (see eq.4.3), therefore

$$\frac{H_p(T)}{H_p(0)} = \frac{H_{c1}(T)}{H_{c1}(0)}. \tag{5.2}$$

As was mentioned in section 1.6, $H_{c1}(T)$ can be described by the temperature dependence of superfluid density with the theoretical curves, where the only parameter is the coupling ratio $2\Delta/k_BT_c$. From BCS theory, for classical s-wave single gap superconductor, the ratio is 3.52 in the weak coupling limit. At first, we assumed that the samples are in the clean limit, since the pinning in the samples was small. When we compared the measured data with the BCS curve with coupling ratio 3.7, obtained

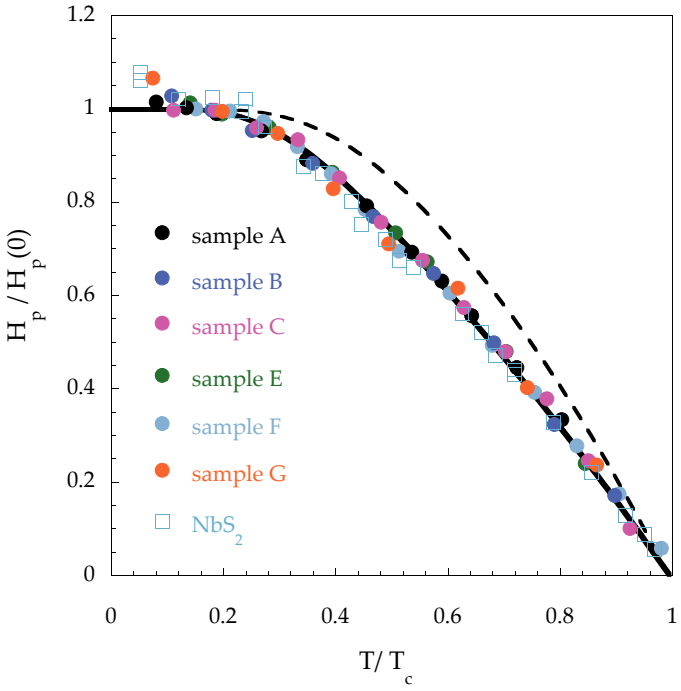

Figure 5.41: Temperature dependencies of $H_p(T)/H_p(0)$ for 6 samples of Cu_xTiSe_2 with different copper doping. Black dashed curve shows the model curve for $2\Delta/k_BT_c = 3.7$ from BCS theory in the clean limit. The data we obtained, do not follow this behaviour but are better described with a two-gap model where $\Delta_1/k_BT_c \sim 2.4$ and $\Delta_2/k_BT_c \sim 3.7$ with similar weights. [69]

in heat capacity measurements [60] (dashed line in Fig.5.41), we found discrepancy, as the theoretical curve showed higher values than what we observed. Using the BCS model for a superconductor in the dirty limit would only lead to higher deviation of the curve from the measured data. Much better agreement between the theory and the data is found for a two-gap fit with $2\Delta_1/k_BT_c = 3.7$ and $2\Delta_2/\kappa_BT_c = 2.4$ with similar weights (see eq.1.36).

The presence of small energy gap was also confirmed by the tunnel diode oscillator (TDO) measurements done in the group of Dr. P. Rodière from Institute Néel in Grenoble [69]. The TDO technique measures the resonant frequency of a circuit of a superconducting sample introduced in a coil of inductance L, biased by a tunnel diode oscillator. The variation of penetration depth introduces a shift in the resonant frequency, which can be directly related to λ through certain calibration constant. From measurements at different temperatures they obtained dependence of $\lambda(T)$ which could be well described by a standard exponential law attesting for

the presence of a fully opened superconducting gap. In sample A, the coupling ratio was found to be $2\Delta/k_BT_c \sim 2.4$ and similar ratios were obtained for samples B ($2\Delta/k_BT_c \sim 2.5$), C ($2\Delta/k_BT_c \sim 2.8$) and G ($2\Delta/k_BT_c \sim 2.4$). These TDO measurements were performed only at very low temperatures where the influence of small energy gap is stronger than of the large gap, therefore in the $\lambda(T)$ dependence they could only identify the energy gap with the smaller coupling ratio.

To some extent, these findings of the second smaller energy gap agrees with the μSR measurement of Zaberchik *et. al* [64]. They also observed 2 energy gaps, however only in samples from the underdoped region. In samples with higher copper doping, the coupling ratio increased and the two energy scales merged for optimal doping. Contrary to this, we observe that the two energy gaps are present in all of the studied samples form underdoped to overdoped region.

However, these observation of small gap are in contrast with the results of the heat capacity measurements performed on our samples by Dr. J. Kačmarčík *et al.* [60, 73, 69]. They found that the coupling ratio value was $2\Delta/k_BT_c \sim 3.7$, which is in a very poor agreement with the TDO measurements (see Fig.5.42). The main

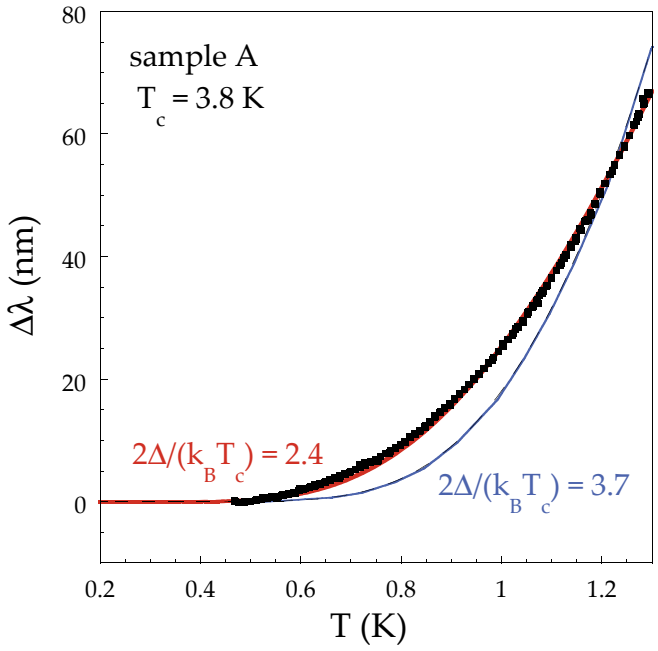

Figure 5.42: Temperature dependence of the London penetration depth obtained from the TDO measurements on sample A. $\lambda(T)$ can be well described by the standard exponential law with $2\Delta/(k_BT_c) \sim 2.4$, while it shows clear discrepancy with the curve for $2\Delta/k_BT_c = 3.7$. [69]

difference between the two techniques is that the TDO is probing the surface of the sample while AC calorimetry measures the heat capacity of a bulk. However, this cannot explain the discrepancy since the two energy gaps were also observed by our Hall probe magnetometry, which probes the bulk properties. Another reason for this disagreement may lay in directional sensitivity of different techniques. On one hand, the magnetic measurements were sensitive to the gap structure in ab direction, as by Hall probe magnetometry we studied $H_{c1}^{c} \sim 1/\lambda_{ab}$ and TDO measurements were also sensitive to λ_{ab}. On the other, the heat capacity is probing all the directions in the k-space. Another difference is that TDO and Hall probe magnetometry are more sensitive to the light electronic bands (as $\lambda \sim 1/m^*$), while heat capacity is more sensitive to heavy electron bands ($\gamma \sim m^*$). To achieve consistency between these measurements, the effective mass should change significantly over the Fermi surface. However, the simple electronic structure and the study of the Fermi surface by ARPES measurements do not validate that.

Also the temperature dependence of H_p is very similar to the one previously observed in other $2H$ dichalcogenides $NbSe_2$ or NbS_2. However, the presence of two gaps was related there to the presence of two different sheets on the Fermi surface and was confirmed by different experimental techniques such as tunneling spectroscopy or heat capacity measurements. This is not the case of Cu_xTiSe_2, since its Fermi surface does not indicate the presence of the second energy gap, which suggests that it might not be related to the electronic structure.

5.3 Critical fields

For each of the studied sample, we determined $H_p(0)$ by extrapolating the temperature dependence of H_p to 0 K. Then with the appropriate geometrical factor, we obtained $H_{c1}(0)$ according to the Brandt relation in eq.4.3. Used geometrical corrections and the values of H_p and H_{c1} are summarized in tab.5.1. In the table, we also summarize the values of $H_{c2}(0)$ obtained from the heat capacity measurements on these samples realized by Dr. J. Kačmarčík *et al.*.

To prove that from the Hall probe magnetometry we obtain correct values of H_{c1}, we are going to perform a thermodynamic consistency check. We take the value of H_{c2} extrapolated to 0 K and from eq.2.1 we get the value of coherence length $\xi(0)$. From H_{c1} at 0 K we calculate through eq.2.6 and 2.8, the value of penetration depth $\lambda(0)$. From $\lambda(0)$ and $\xi(0)$, we calculate the thermodynamic critical field $H_c(0)$ according to

x	Label	T_c (K)	α_c	$\mu_0 H_p^c$ (0)[G]	$\mu_0 H_{c1}^c$ (0)[G]	$\mu_0 H_{c2}^c$ (0)[kG]	$\mu_0 H_c$ (0)[G]
0.052	D	2.3	-	-	-	5.0	-
0.061	C	2.8	4.3	14	60	5.5	335
0.064	B	3.2	4.5	18	80	7.0	429
0.075	G	4.1	2.3	50	115	9.5	631
0.084	A	3.8	3.8	30	114	7.5	546
0.086	E	3.5	5	21	105	5.5	457
0.092	F	3.0	3.1	30	95	4.5	392

Table 5.1: Table summarizing the data for 7 samples of Cu_xTiSe_2 with different copper doping x. T_c is the critical superconducting temperature, α_c is the geometrical correction in the c direction, $H_p^c(0)$ is the penetration field at zero temperature in c direction obtained by Hall probe magnetometry, $H_{c1}^c(0)$ is the lower critical magnetic field obtained from $H_p^c(0)$ by using eq.4.3, $H_{c2}^c(0)$ is the upper critical magnetic field obtained from AC calorimetry measurements [60] and $H_c(0)$ the thermodynamic critical field obtained from H_{c1} and H_{c2}.

equation 1.20. Then from the eq.1.24, we can relate $H_c(0)$ to the density of states at the Fermi level, $g(E_F)$, which is then used to calculate the value of Sommerfeld coefficient γ as

$$\gamma = \frac{\pi^2 k_B^2 \; g(E_F)}{3}. \tag{5.3}$$

By this way we deduced the value of Sommerfeld coefficient for sample A to be $\gamma \sim 6 \pm 2$ mJ mol^{-1}K^{-2}. This value is in a good agreement with the value obtained directly from the heat capacity measurements by Morosan *et al.* for a sample with similar doping, giving $\gamma \sim 4.5$ mJ mol^{-1}K^{-2} [2]. This consistency proves that the measurements give correct results.

Now we are going to analyse the evolution of the determined critical fields with T_c in various samples of Cu_xTiSe_2. As the coherence length is directly related to H_{c2} (eq.2.1), we expect

$$H_{c2} \propto \frac{1}{{\xi_0}^2} \sim \frac{\Delta^2}{{v_F}^2} \sim T_c^2, \tag{5.4}$$

where ξ_0 is the Pippard coherence length unaffected by the scattering effect. This equation can be used only in the clean limit, when the mean free path, l, is bigger than coherence length, $l >> \xi$. In dirty limit, the values of λ and ξ are affected by l:

$$\xi_0 = \frac{\xi^2}{0.731 \; l} \tag{5.5}$$

and

$$\lambda_L = \lambda\sqrt{\frac{1.33\ l}{\xi_0}}, \tag{5.6}$$

where λ_L is the London penetration depth in the clean limit. Taking into account these relations, for $H_{c2}(T_c)$ in the dirty limit we expect

$$H_{c2} \propto \frac{1}{\xi_0 l} \sim \frac{\Delta}{v_F l} \sim T_c. \tag{5.7}$$

Fig.5.43 displays the dependence of $H_{c2}(T_c)$ of the studied Cu_xTiSe_2 single crystals. For samples from the underdoped region, H_{c2} scales as T_c (dashed line), while for the overdoped samples it follows T_c^2 dependence. Therefore, according to the previous equations, the underdoped samples are in the dirty regime, while the samples from the overdoped part of the superconducting dome are in the clean limit.

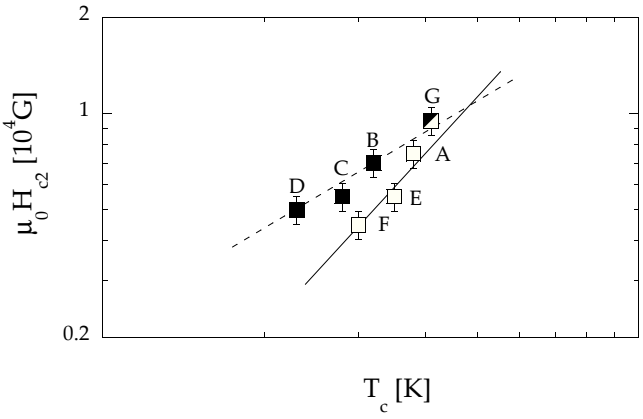

Figure 5.43: T_c dependencies of the upper critical field at zero temperature $H_{c2}(0)$ measured in the field oriented parallel with the c direction, for samples from the underdoped (full black squares) and overdoped region (white squares), and the optimally doped sample G. Dotted line shows $\sim T_c$ dependence and solid line T_c^2.

As a check, we compare the λ and ξ values extrapolated from H_{c1} and H_{c2}, to the values obtained by analysis of ARPES measurements by Dr. D. Evtushinsky and Dr. S. Borisenko on sample with copper doping $x = 0.07$. From ARPES, we deduce the values of London penetration depth and coherence length, which are unaffected by the mean free electron path, λ_L and ξ_0. Accounting for the Fermi velocity, shape of the Fermi surface and superconducting gap, ARPES measurements give $\lambda_L = 150\pm50$ nm and $\xi_0 = 40\pm8$ nm, [74]. The Hall probe magnetometry and heat capacity

measurements were not performed on the sample with concentration $x = 0.07$, so we interpolated the data between the samples B and G with x slightly above and below $x = 0.07$ to estimate λ and ξ for such a copper concentration. We get the values of $\lambda = 220$ nm and $\xi = 20$ nm Using the formulas 5.5 and 5.6, we can find two values for the mean free path. Both results give $l = 13.5$ nm, which confirms that this underdoped sample is in the dirty limit in agreement with our analysis of $H_{c2}(T_c)$ dependence for underdoped samples.

Fig.5.44 displays the dependencies of $H_{c1}(0)$ and $H_c(0)$ on the critical temperature. As H_{c1} is proportional to the penetration depth, in the dirty limit we expect for H_{c1}

$$H_{c1} \propto \frac{1}{\lambda} \sim \frac{l}{\lambda_L^2 \xi_0} \sim T_c, \tag{5.8}$$

while in the clean limit H_{c1} is independent of T_c. As $H_c \propto \sqrt{H_{c1} H_{c2}}$, then in both

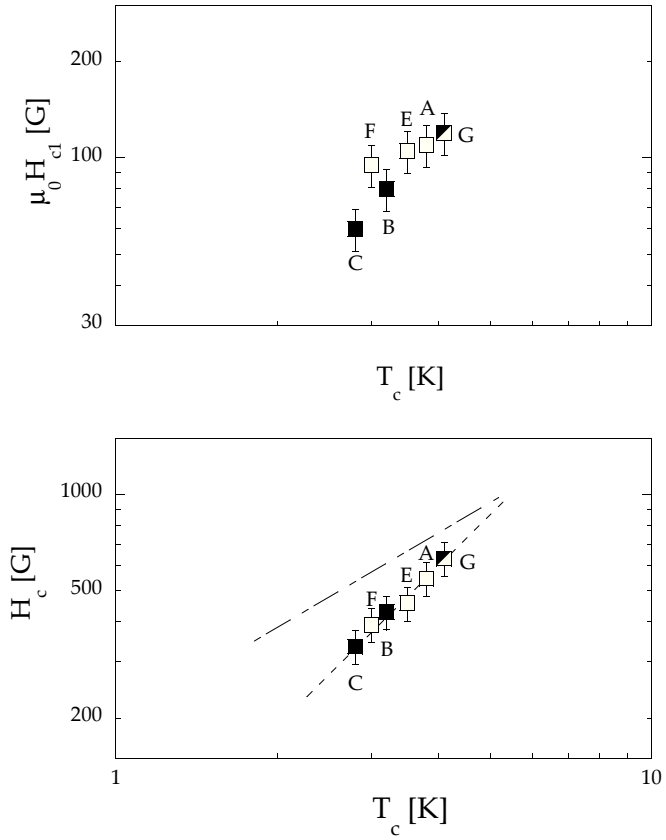

Figure 5.44: T_c dependencies of lower critical fields H_{c1} (*Top*) and thermodynamic critical fields H_c (*Bottom*), for samples from the underdoped (full black squares) and overdoped region (white squares), and the optimally doped sample G. Dotted-dashed line displays the standard dependence as T_c and dashed line corresponds to $T_c^{1.5}$.

clean and dirty limit

$$H_c \sim T_c. \tag{5.9}$$

Our results in Fig.5.44 however indicates that $H_c \sim T_c^{1.5}$ (dashed line). Such a T_c dependence of H_c has been reported in the iron based materials [75] and suggests the presence of strong pair breaking mechanism or the presence of quantum critical point near the end of the superconducting dome. However, the pair breaking effects can be ruled out, since they would lead to a powerlaw behaviour in the temperature dependence of penetration depth, in contrast to our measurements.

Chapter 6

Lock-in effect in Cu_xTiSe_2

In the following chapter, I am going to analyse the results obtained from local Hall probe magnetometry measurements for different orientations of the applied field. The scheme of the experimental set-up when the Hall probe is placed parallel to the sample ab-planes, is displayed in Fig.6.45.

Magnetic field H_a is applied at the angle θ_H counted from the ab planes of the sample. The Hall probe always detects only the magnetic field that is perpendicular to its surface. Thus, if in the experiment the orientation of the probe and sample is as shown in the Fig.6.45, the Hall probe effectively measures only the component of magnetic induction B parallel with the c direction $B^c = B \sin\theta_B$, where θ_B is the orientation of B relative to the ab planes.

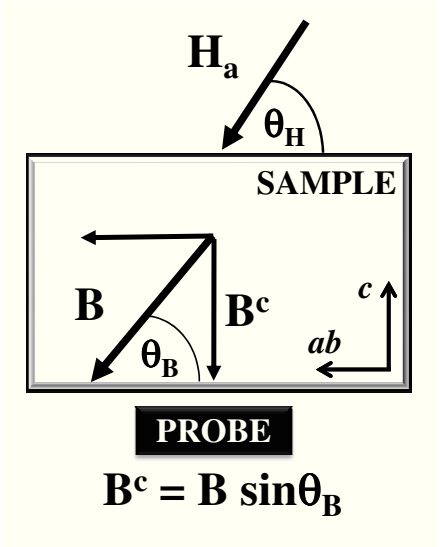

Figure 6.45: Scheme of the sample in magnetic field oriented by angle θ_H counted from the sample ab planes. In this set-up, the Hall probe below the sample detects the component of the field induction B in the c direction given as $B^c = B \sin\theta_B$.

The field dependence of B^c measured for different fixed field orientations θ_H is shown in Fig.6.46 on sample A, as an example. The data are scaled by $\sin\theta_H$, which for high enough magnetic fields is equal to $\sin\theta_B$. Then $B^c/\sin\theta_H = B^c/\sin\theta_B = B$ and all curves converge to the same curve corresponding to $B = \mu_0 H_a$.

When we compare the signals for different angles θ_H, we see that for large θ_H (e.g. $\theta_H = 57°$ displayed by black curve in Fig.6.46), B^c sharply increases when vortices enter the sample at $H_a = H_p$. However, when the orientation of applied magnetic field approaches the ab planes ($\theta_H \to 0$), the behaviour of $B^c(H_a)$ changes. When H_a reaches penetration field H_p, we see only a small increase in the signal, opposite to what is observed at higher angles. With $H_a > H_p$, the B^c signal remains close to zero until the applied field reaches a second characteristic field, called here H_k, when a sharp kink appears in the B^c signal. The significantly reduced value of B^c observed for $H_p < H_a < H_k$ suggests that vortices entering the sample are oriented along the ab planes and remains locked in this direction until the field reaches the value

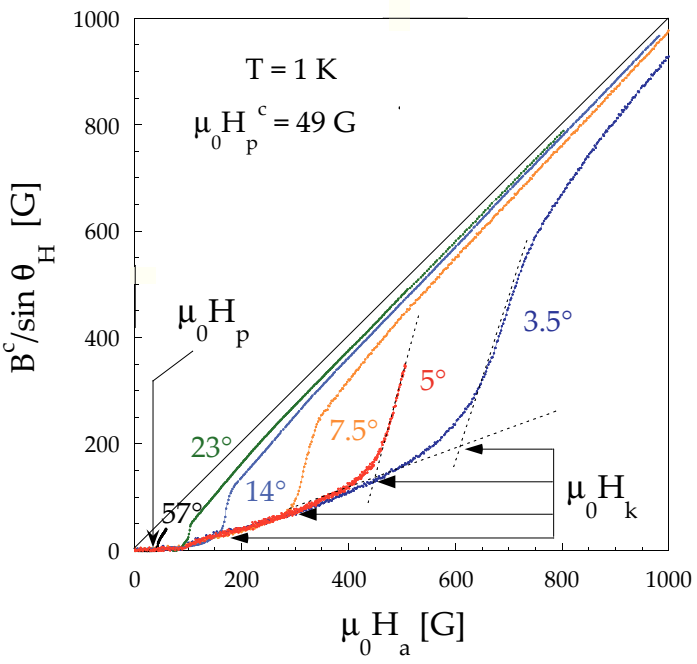

Figure 6.46: Magnetic field dependencies of B^c, the component of field induction in the sample parallel with the c direction, divided by $\sin\theta_H$, measured at different orientations of applied field θ_H (counted from the ab planes) in sample A at $T = 1$ K. H_p is indicated by the first increase of the signal, while at H_k the second sharper increase in the B^c signal can be observed. [76]

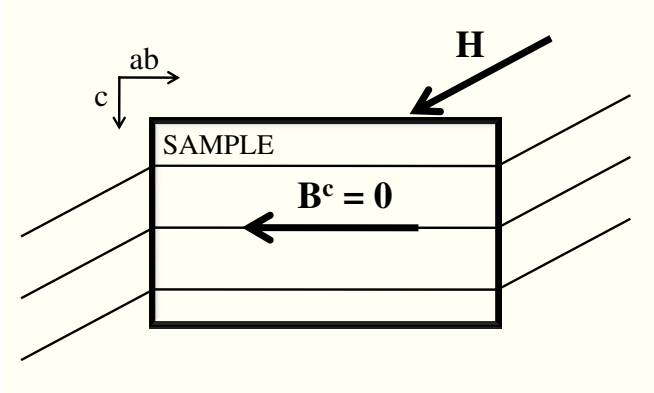

Figure 6.47: Scheme of the vortices locked along the *ab* planes in the sample.

of H_k. Vortices parallel to the planes leave the sample through the side and cannot be detected by the Hall probe located below the sample (see the sketch in Fig.6.47). The small non-zero B^c signal could be caused by the small distance between the probe and sample. It is also possible that not all of the vortices get locked along the planes and a small fraction of them remains tilted. When the field reaches H_k, vortices unlock from the parallel orientation and the B^c signal starts to increase rapidly.

Figure 6.48 displays the same data as Fig.6.46 but both the horizontal and vertical axis were multiplied by $\sin\theta_H$, therefore the plot displays B^c as function of $H_a \sin\theta_H$.

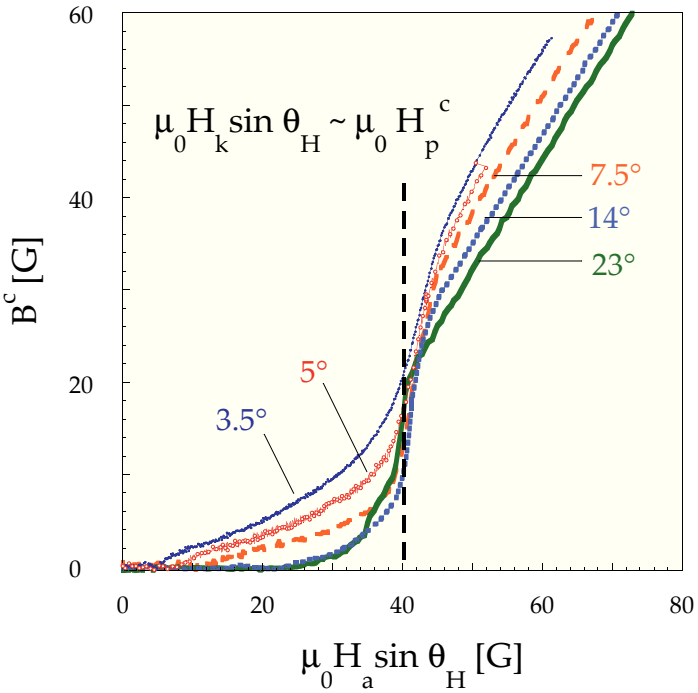

Figure 6.48: Curves from Fig.6.46 scaled by $\sin\theta_H$ showing that $\mu_0 H_k \sin\theta_H \sim 40$ G, which is close to the value of $\mu_0 H_p^c$ in the sample. [76]

In this representation, the field of the second upturn H_k scales by $\sin\theta_H$ for different angles, such as is expected for the lock-in effect (see chapter 2). From the data, you can also note that $\mu_0 H_k \sin\theta_H \sim 40$ G, which is very close to $\mu_0 H_p^c$ value in this case. This implies that, according to eq.2.15, the lock-in effect is extremely strong in this sample.

6.1 Field dependence of vortex orientation

To analyse the vortex orientation θ_B, both components of B are needed. As shown in the sketch in Fig.6.49, B^c was measured on the probe located below the sample and the B^{ab} component was obtained from a Hall probe located at the side of the sample with its surface parallel with the c direction. Figure 6.50 displays the field dependencies of the B^c and B^{ab} components of B divided by $\sin\theta_B$ and $\cos\theta_B$, respectively. The data were obtained from measurements on sample G for magnetic field applied at the orientation $\theta_H = 25°$. In this sample, H_p was angularly independent as the anisotropy was cancelled out by the geometrical effects (further details are mentioned in section 6.3). If the vortices would be aligned with the applied magnetic field, $\theta_B = \theta_H$, then

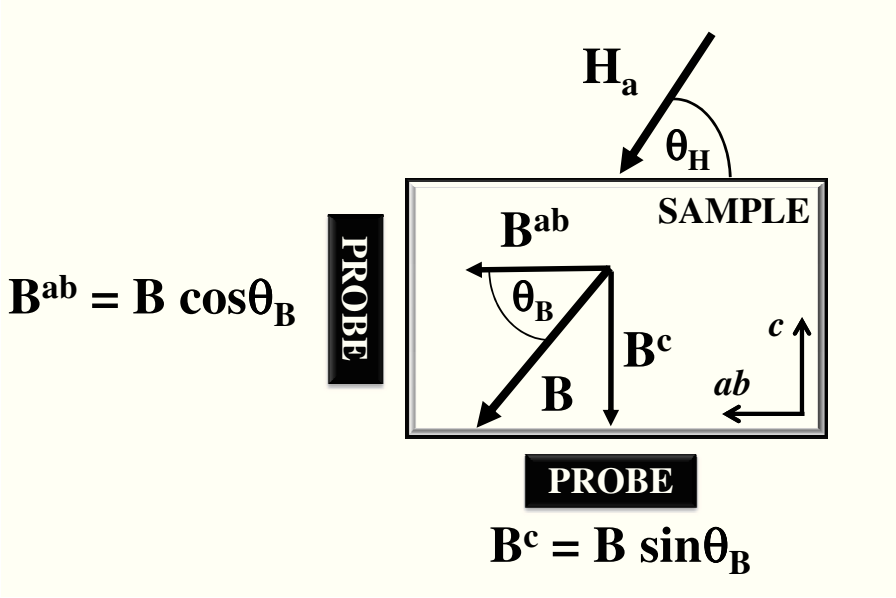

Figure 6.49: Scheme of the Hall probes versus sample configuration to measure both components of field induction B to obtain the information about the vortex orientation θ_B.

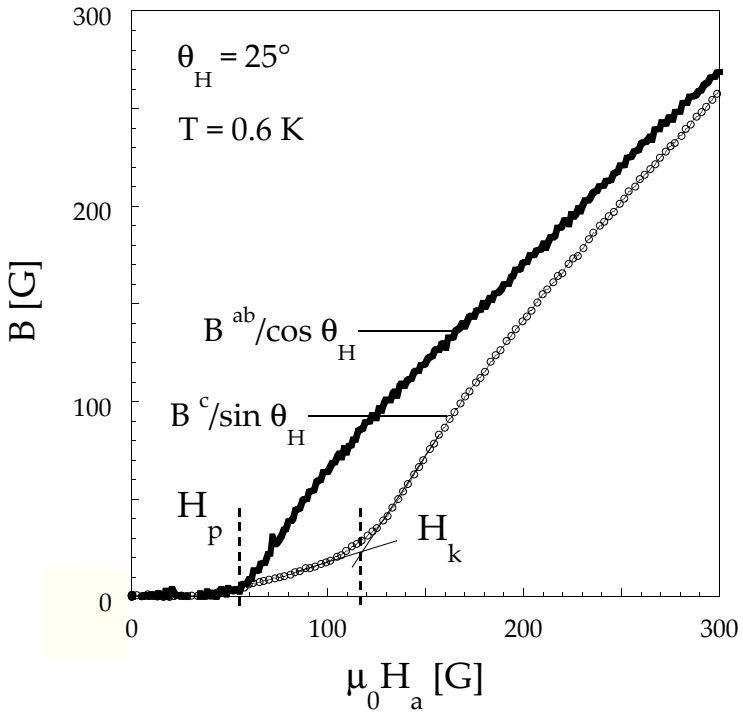

Figure 6.50: Magnetic field dependence of $B^{ab}/\cos\theta_H$ and $B^c/\sin\theta_H$ components of field induction in sample G obtained in magnetic field with orientation $\theta_H = 25°$ at temperature $T = 0.6$ K.

in this representation the two curves in Fig.6.50 would be identical as

$$\frac{B^{ab}}{\cos\theta_H} = \frac{B\cos\theta_B}{\cos\theta_H} = B = \frac{B\sin\theta_B}{\sin\theta_H} = \frac{B^c}{\sin\theta_H}. \tag{6.1}$$

This is obviously not the case. While $B^{ab}/\cos\theta_H$ increases sharply above H_p, signal $B^c/\sin\theta_H$ on the contrary, remains small. This clearly shows that the vortices that enter the sample at $H_a > H_p$ remain locked along the planes and exit the sample through the sides. As a result, we detect a sharp increase of the signal measured by the probe perpendicular to the planes, while we see much lower signal on the Hall probe below the sample.

By dividing the field dependencies of $B^{ab}/\cos\theta_H$ and $B^c/\sin\theta_H$, we obtain the information about the vortex orientation θ_B as

$$\frac{B^c/\sin\theta_H}{B^{ab}/\cos\theta_H} = \frac{B\sin\theta_B}{B\cos\theta_B}\cdot\frac{1}{\tan\theta_H} = \frac{\tan\theta_B}{\tan\theta_H}. \tag{6.2}$$

Figure 6.51 displays the field dependencies of $\tan\theta_B(H_a)/\tan\theta_H$, for certain angles of applied field θ_H and temperatures, obtained from measurements at sample G. The

small B^c signal for $H_a < H_k$ introduce significant errors into the field dependence of θ_B, therefore we present only the data for $H_a > H_k$. At the lowest fields, $\tan\theta_B/\tan\theta_H$ is small and increases as vortices unlock from the planes direction. For highest magnetic fields $\tan\theta_B/\tan\theta_H$ approaches 1, which means that vortices gradually align with the magnetic field and $\theta_B \to \theta_H$. For the data obtained at 70°, θ_B is approaching θ_H in the whole inspected range and for higher angles we could not observe the lock-in effect any more.

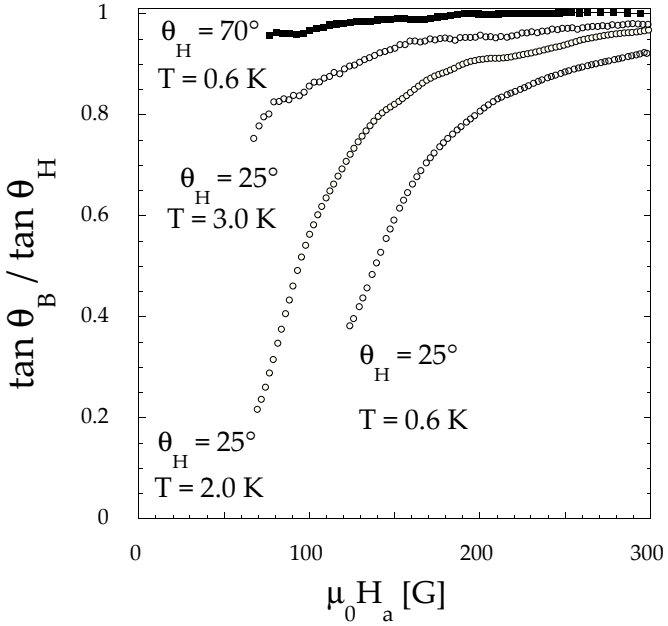

Figure 6.51: Field dependence of θ_B the orientation of vortices in the sample, for given temperatures T and orientations of the applied field θ_H. Open black points display the data measured at the same $\theta_H = 25°$ but at different temperatures. Full black points represent data at $\theta_H = 70°$.

6.2 Modified Blatter model

The presence of the lock-in effect in Cu_xTiSe_2 is unexpected. An intrinsic lock-in is usually observed in layered materials where normal and superconducting layers alternate. These compounds exhibit high anisotropy, which causes that the coherence length in the c direction is small compared to the interlayer distance and vortices may fit between the layers. This is however not the case for Cu_xTiSe_2. In this system, the anisotropy is small and with $\xi_c \sim 12$ nm and $d = 0.6$ nm, $\xi_c >> d$. Given that

in this system the values of κ and Γ do not fall into the range of values that would result in the observation of the two sets of crossing lattices mentioned in chapter 3, the intrinsic lock-in effect is not possible in this compound. This leads us to a conclusion that there must exist an additional layered structure parallel with ab planes where the superconductivity would be at least partially suppressed and vortices can get pinned. It was proposed in model by Blatter *et al.* in ref. [31] that in the presence of correlated defects, vortices create a staircase vortex structure. To use the model in our case, it had to be extended so that it could be used for any angle and anisotropic systems.

6.2.1 Isotropic case for arbitrary angle

At first, let us still consider the isotropic case but find the solution for an arbitrary orientation of magnetic field, thus excluding the approximation of small angles used by Blatter. In the model, Blatter begins by finding the energy of a staircase vortex, which orients parts of its core of length r in the plane, where its line tension ε_l is reduced by the value ε_P (see the sketch in Fig.6.52). The energy gain from the vortex segment trapped on the plane is balanced by the energy cost due to the elastic deformation of the vortex. The total energy is then given by

$$E(\theta_B, r) = r(\varepsilon_l - \varepsilon_P) + s\varepsilon_l - t\varepsilon_l, \tag{6.3}$$

where s and t are the lengths characterized in the scheme in Fig.6.52. By minimizing the energy function with respect to θ_B and setting it equal to zero, the optimal value for r is found as

$$r = \frac{d}{\tan\theta_B} - \frac{d}{\tan\theta_t}, \tag{6.4}$$

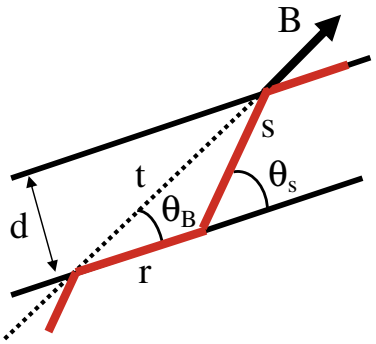

Figure 6.52: Scheme of a single vortex line accommodating to the layered structure where superconductivity is suppressed.

where

$$\tan\theta_t = \frac{\sqrt{2\varepsilon_l\varepsilon_P - \varepsilon_P^2}}{\varepsilon_l - \varepsilon_P}. \tag{6.5}$$

By inserting this expression for r back into 6.3, the resulting E function will depend only on θ_B

$$E(\theta_B) = \frac{d}{\tan\theta_B}(\varepsilon_l - \varepsilon_P) - \frac{d}{\sin\theta_B}\varepsilon_l + d\tan\theta_t(\varepsilon_l - \varepsilon_P). \tag{6.6}$$

Assuming small but finite density of vortices in the system equal to $B/(\phi_0 t)$, we obtain corresponding energy density $E' = EB/(\phi_0 t)$. The total density of the Gibbs energy of the system then comprises the magnetic field inside the vortices, the energy of the shielding supercurrents, the core deformation on the planes and the energy depending on the orientation of B in applied magnetic field:

$$\begin{aligned} g = \frac{B^2}{8\pi} + \frac{\phi_0 B\varepsilon_l}{2(4\pi\lambda)^2}\ln\left[\frac{H_{c2}^c}{\varepsilon_l B}\right] + \\ -\frac{B}{\phi_0}(\varepsilon_l - \varepsilon_P)\sin\theta_B - \frac{B}{\phi_0}\varepsilon_l + \frac{B}{\phi_0}(\varepsilon_l - \varepsilon_P)\sin\theta_B\tan\theta_t + \\ -\frac{BH}{4\pi}\cos\left(\theta_B - \theta_H\right) . \end{aligned} \tag{6.7}$$

By derivating g with respect to θ_B and setting $\partial g/\partial\theta_B = 0$, we find the minimum of g and the following solution for field dependence of vortex orientation θ_B:

$$\frac{\tan\theta_B}{\tan\theta_H} \approx \begin{cases} 0 & H < H_L \\ \dfrac{1 - \frac{H_L}{H}}{1 - \frac{H_L}{H}\frac{\tan\theta_H}{\tan\theta_t}} & H_L < H, \theta_H < \theta_t \quad (2) \\ 1 & \theta_t < \theta_H \end{cases} \tag{6.8}$$

where H_L is the critical lock-in field given as

$$H_L = \frac{4\pi}{\phi_0}\frac{\sqrt{2\varepsilon_l\varepsilon_P - \varepsilon_P^2}}{\sin\theta_H} \sim \frac{H_{c1}^c}{\sin\theta_H}\sqrt{2\frac{\varepsilon_p}{\varepsilon_l} - \frac{\varepsilon_p^2}{\varepsilon_l^2}} \tag{6.9}$$

This solution states that at given orientation of applied field θ_H, we observe vortices in the lock-in state ($\theta_B = 0°$) up to certain critical lock-in field H_L. For higher fields vortices unlock and create staircase structure which lasts until θ_B reaches a critical angle θ_t. Then vortices finally align with the applied field and $\theta_B = \theta_H$.

6.2.2 Anisotropic case

Let us now consider the effect of anisotropy in the model. The energy gain on the staircase structure changes from eq.6.3 to

$$E(\theta_B, \Gamma, r(\theta_s)) = r(\theta_s)(\varepsilon_l(0,\Gamma) - \varepsilon_P) + s\varepsilon_l(\theta_s,\Gamma) - t\varepsilon_l(\theta_B,\Gamma), \tag{6.10}$$

where we need to take into account that the vortex line tension ε_l is angularly dependent $\varepsilon_l(\theta) = \varepsilon_0\sqrt{\sin^2\theta + \Gamma^2\cos^2\theta}$ and $\varepsilon_0 = (\phi_0^2 \ln\kappa)/(4\pi\mu_0\lambda_{ab}^2)$ [24]. Finding the minimum of the function with respect to θ_B and the general solution for arbitrary anisotropy value is not trivial. We found the numerical solutions for certain values of anisotropy Γ and $\varepsilon_R = \Gamma\varepsilon_P/\varepsilon_l$. The solution are displayed in Fig.6.53, together with the analytical solution for isotropic case with $\Gamma = 1$ and $\varepsilon_R = 1/2$. As shown, for all the investigated cases, E can be very well described by a simple parabolic approximation

$$E(\theta_B, \Gamma, \varepsilon_R) \approx -\frac{1}{2}\,\varepsilon_l(\Gamma,\varepsilon_R)(\theta_B - \theta_t(\Gamma,\varepsilon_R))^2, \tag{6.11}$$

where parameter ε_l affects the shape of the parabola and θ_t defines the position of its maximum. Change of the parameters Γ and ε_R does not significantly affect the shape

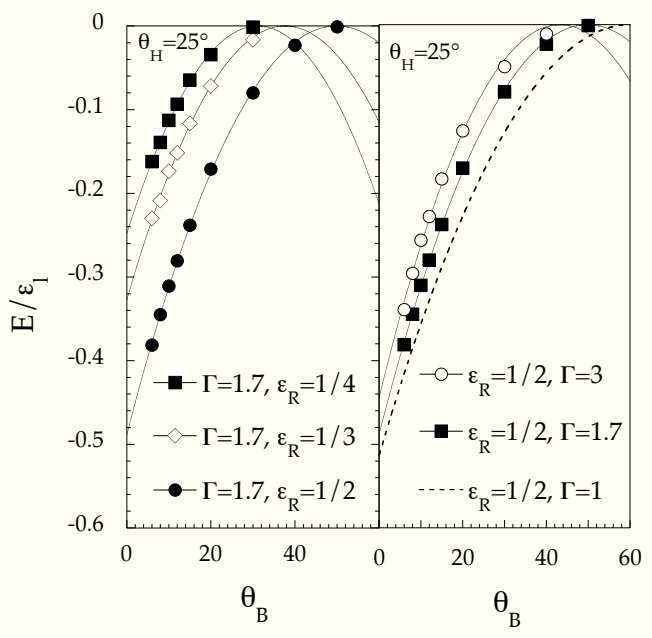

Figure 6.53: Angular dependence of the total energy of a vortex in a staircase structure $E(\theta_B)$ at constant $\theta_H = 25°$ for the indicated Γ and ε_R values (see text for details) (points). Dotted line corresponds to the analytical dependence for isotropic case (eq.6.6) and the solid lines represent the parabolic fits to the data (eq.6.11). [76]

of the parabola (and consequently ε_l), only the value of θ_t is shifting. The parabolic approximation, similar to one obtained by Blatter in [31], is thus valid also to some extent in the anisotropic case. This allows us to take the same solution for $\theta_B(H)$ as in the isotropic case in eq.6.8, however with H_L given as

$$H_L(\Gamma, \varepsilon_R) \approx \frac{H_{c1}^c}{\sin\theta_H} \cdot F(\Gamma, \varepsilon_R). \tag{6.12}$$

The strength of H_L now depends also on anisotropy through unknown function $\mathcal{F}$. However, as the numerical solutions showed, the small anisotropy in Cu_xTiSe_2 ($\Gamma = 1.7$) introduces only a minor shift into the θ_t values of around $1° - 2°$. Therefore $\mathcal{F}$ can be expected to be related mainly to ε_R giving the measure of how much is the superconductivity suppressed in the plane.

The influence of demagnetisation effect was also taken into account, since we only have the information about field we apply, H_a, and the field at the sample surface is unknown. To obtain the real magnetic field at the sample surface, we calculated the demagnetisation field depending on geometrical factors and magnetisation M for $\theta = 25°$. For the field H at the surface and its components in c and ab directions we get

$$\begin{aligned} H_c &= \alpha^c H_a \sin\theta_H - (\alpha^c - 1)B^c/\mu_0 \\ H_{ab} &= \alpha^{ab} H_a \cos\theta_H - (\alpha^{ab} - 1)B^c/\mu_0 \\ H &= \sqrt{H_{ab}^2 + H_c^2} \end{aligned} \tag{6.13}$$

where α^c is the geometrical corrections obtained from eq.4.3 for geometrical barriers and $\alpha^{ab} = \alpha_c/(1 + \alpha_c)$. In this approach we neglected the angular dependence of α as for θ_H not too far from 0° the deformation of the field lines around the sample changes very little from the one in magnetic field parallel with the c direction. The resulting field at the sample does not introduce qualitative changes into the model curves, therefore the effect of demagnetisation fields was neglected.

The data from Fig.6.51 were then fitted by the modified Blatter model (eq.6.8) and the data and the model curves (red lines) are displayed together in Fig.6.54. By changing the parameters H_L and θ_t, the model curves could very reasonably describe the data.

The parameters obtained from the fits and values of H_k and H_p directly determined from the measured curves were used to construct the phase diagram displayed in the Fig.6.55. The position of the points in the graph is defined by their amplitude

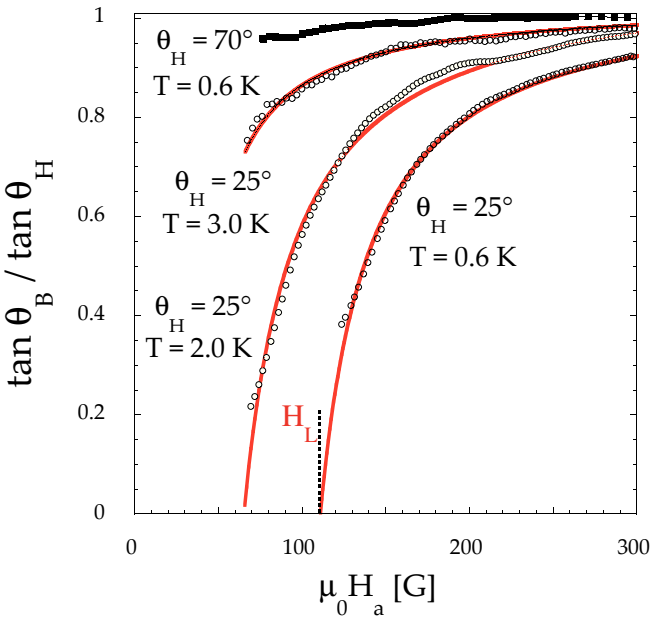

Figure 6.54: Data from Fig.6.51 displayed with the curves from the modified Blatter model (eq.6.8).

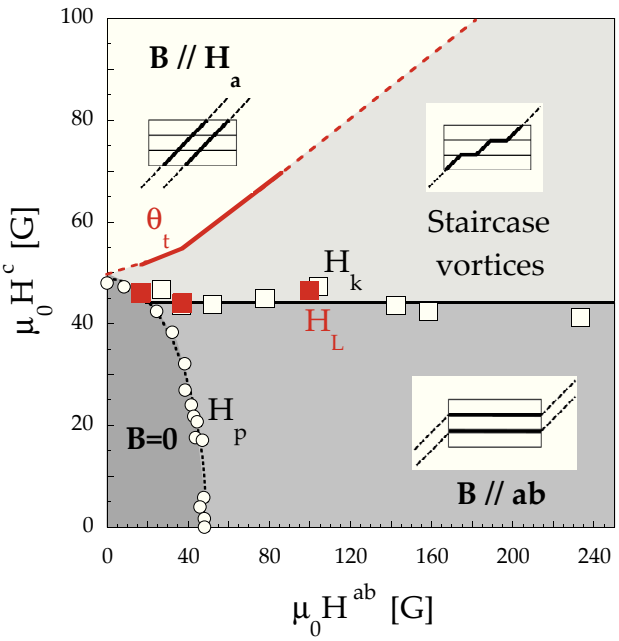

Figure 6.55: Phase diagram of the vortex structure as a function of field orientation and amplitude in $Cu_{0.075}TiSe_2$ (sample G) at $T = 0.6$ K. H_k and H_p values were obtained directly from the $B^c(\theta_H, H_a)$ curves, H_L and θ_t (red) are parameters obtained from fits to data using eq.6.8. [76]

and the angle of applied magnetic field at which there were obtained. The resulting phase diagram displays four different vortex structures, Meissner state, vortices being locked in the planes, staircase structure and tilted vortex lattice. The values of H_L obtained from the fits are in a good agreement with H_k determined as the field of the second increase in the $B(H_a, \theta_H)$ curves. The behaviour of H_L in this representation means that H_L scales as $\sin\theta_H$ and $H_L/\sin\theta_H \sim H_p^c$, similar to behaviour of H_k (see Fig.6.48).

6.3 Comparison on three different samples

The lock-in effect was studied on three samples of Cu_xTiSe_2, samples A, E and G that have different copper doping and geometry. From measurements at different angles, we obtained the angular dependencies of H_p and H_k. As the data for each of the samples displayed in Fig.6.56 show, $H_k(\theta_H)$ rapidly increases for field direction

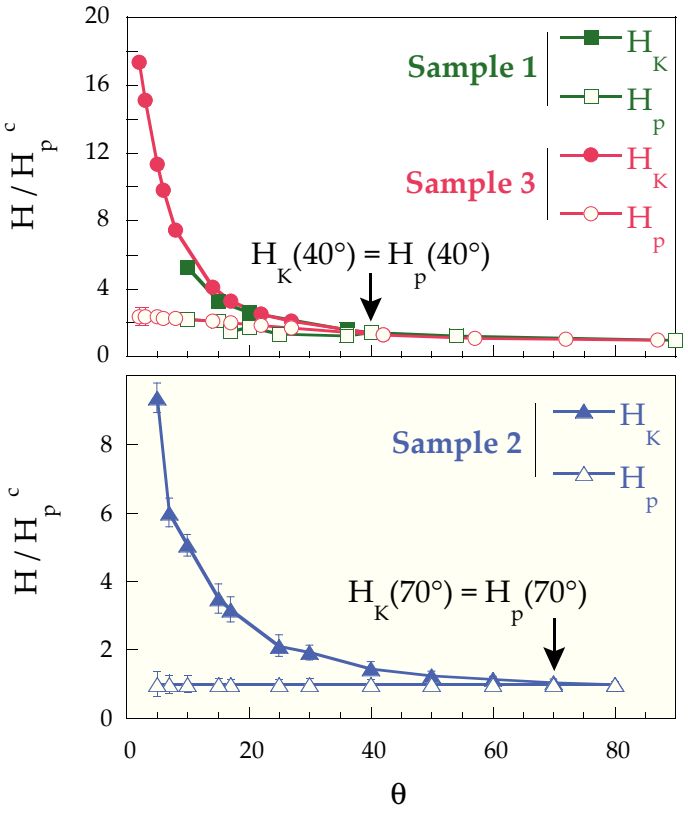

Figure 6.56: Angular dependencies of H_p and H_K obtained for three single crystals of Cu_xTiSe_2. Top panel is showing data for sample 1 and 3 with x =0.06 and 0.085, and bottom panel data for sample 2 with x=0.075.

approaching 0°, whereas $H_p(\theta_H)$ is only weakly angularly dependent. If the samples are compared to each other, one can notice that the threshold angle above which H_k can not be distinguished from H_p anymore, is much smaller for samples 1 and 3 ($\sim 40°$) than for sample 2 ($\sim 70°$).

To exclude the influence of sample geometry on the lock-in effect, the proper geometrical corrections for H_p and H_k had to be found. From the field profiles we know, that in applied field parallel with the c direction, the vortex penetration is affected by the geometrical barriers and by using the formula in eq.4.3 we found α_c correction in $H^c_{c1} = \alpha_c H^c_p$, depending only on the sample geometry (see tab.5.1). However, in different field orientations the deformation of field lines around the sample changes. In magnetic field oriented parallel with the ab planes, the deformation is small and also the geometrical effects loose their importance as for $2w/d >> 1$ in eq.4.3, $H_{c1} \to H_p$. It is not possible to determine the geometrical corrections for every angle only from the sample geometry but following [72], α can be reasonably well estimated by an elliptical approximation

$$\alpha(\theta_H) = \sqrt{(\alpha_c \sin\theta_H)^2 + (\frac{\alpha_c}{\alpha_c - 0.5}\cos\theta_H)^2}. \tag{6.14}$$

By using this α correction, we obtain the angular dependence of H_{c1} as

$$H_{c1}(\theta_H) = \alpha(\theta_H) H_p(\theta_H). \tag{6.15}$$

On the other hand, the critical lock-in field is limited only by the H^c_{c1} value [16], therefore to obtain geometry independent H_L from H_k, we need to take into account only the correction in the c-direction for the whole angular dependence, thus

$$H_L(\theta_H) = \alpha_c H_k(\theta_H). \tag{6.16}$$

Now we can conclude on the effect of geometry on the lock-in effect. Note that, the lock-in effect can only be observed if $H_k(\theta_H) > H_p(\theta_H)$. If we take into account equations 6.15 and 6.16, then from eq.2.14 describing the scaling of the critical lock-in field, we get

$$H_k(\theta_H) = \lambda \frac{H^c_p}{\sin\theta_H}. \tag{6.17}$$

Inserting this formula into the inequality $H_k(\theta_H) > H_p(\theta_H)$ and again using eq.6.15, we obtain

$$\sin\theta_H < \lambda \frac{H^c_{c1}}{H_{c1}(\theta_H)} \frac{\alpha(\theta_H)}{\alpha_c}. \tag{6.18}$$

By assuming that θ_H is reasonably close to the ab planes, from eq.6.14 we have $\alpha(\theta_H) = 1$ and the angular dependence of H_{c1} is changing very little, therefore $H_{c1}(\theta_H) \approx H_{c1}^{ab}$. Using these approximations in eq.6.18, we obtain

$$\sin\theta_H < \lambda\, \Gamma_{H_{c1}}/\alpha_c, \tag{6.19}$$

with $\Gamma_{H_{c1}} = H_{c1}^c/H_{c1}^{ab}$. If one takes $\lambda = 1$, $\Gamma_{H_{c1}} = 2$ and corresponding α_c values, the threshold angle for lock-in observation is then expected to be around 25° in sample 1 and 3 and $\sim$ 65° in sample 2, which is in fair agreement with our experimental values (see Fig.6.56). On the contrary, if one would assume an intrinsic lock-in effect in our samples, then λ would be on the order of $\sim d/\xi \sim 0.02$ (comparable with the $\lambda \sim 0.03$ for the twin boundaries in YBaCuO [77]) and, again introducing α^c values and $\Gamma \sim 1.7$, the lock-in effect would have been observed for over less than 1° from the ab-planes, in striking contrast with the experimental data.

Taking the appropriate geometrical factors, we obtain from $H_k(\theta)$ and $H_p(\theta)$ the geometry independent critical lock-in field $H_L(\theta_H)$ and the lower critical field $H_{c1}(\theta_H)$. All of this data are displayed in Fig.6.57 scaled to the value of H_{c1}^c. Despite different

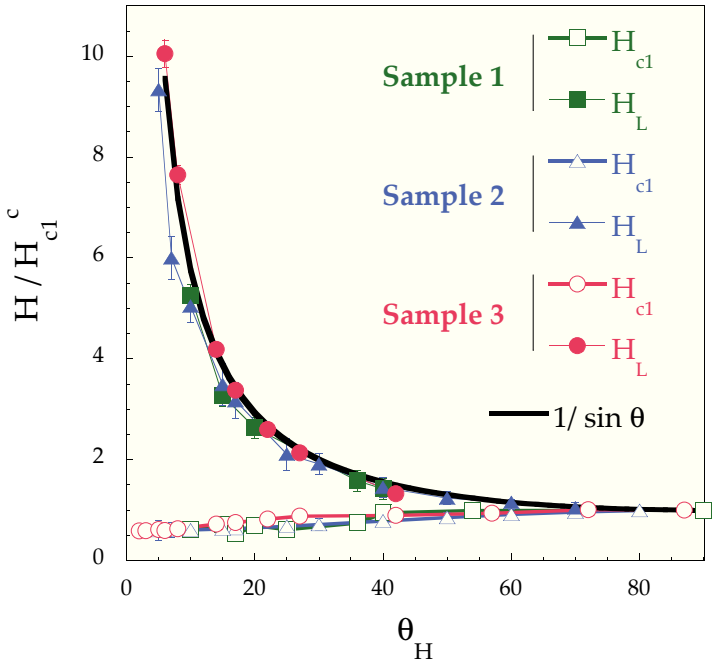

Figure 6.57: Angular dependencies of H_{c1} and H_L obtained by multiplying $H_p(\theta)$ and $H_K(\theta)$ with the appropriate geometrical factors (see text). All the data are scaled to H_{c1}^c. The thick black line is $1/\sin\theta$ line corresponding the strongest possible lock-in effect.

geometry and copper doping of the three samples, $H_{c1}(\theta_H)$ dependencies follow all the same behaviour with the anisotropy of lower critical field to be $\Gamma_{H_{c1}} = H_{c1}^{ab}/H_{c1}^{c} \sim 2$. This behaviour was expected, since the anisotropy of H_{c2} from the heat capacity measurements was found to be also independent of copper doping with value of $\Gamma_{H_{c2}} = 1.7$ [60]. The angular dependencies of H_L also collapse onto the same curve for all of the three samples. Moreover, they follow curve $1/\sin\theta_H$ (thick black line in Fig.6.57), which corresponds to the strongest possible lock-in effect with the strength $\lambda = 1$.

At the end of this chapter, let me comment on the temperature dependence of the lock-in effect. From the data displayed in Fig.6.54 for vortex orientation obtained at different temperatures, it could be assumed that the critical lock-in field shifts to smaller values with increasing temperature. This is reasonable, as H_L and H_k have to follow the same temperature dependence as H_{c1}^{c} or H_{p}^{c}. Figure 6.58 shows the field dependencies of B^c for field orientation $\theta_H = 15°$ at sample E, as an example. As shown, the initial (small) increase of B^c for $H_p(15°) \leq H_a \leq H_K(15°)$ is only

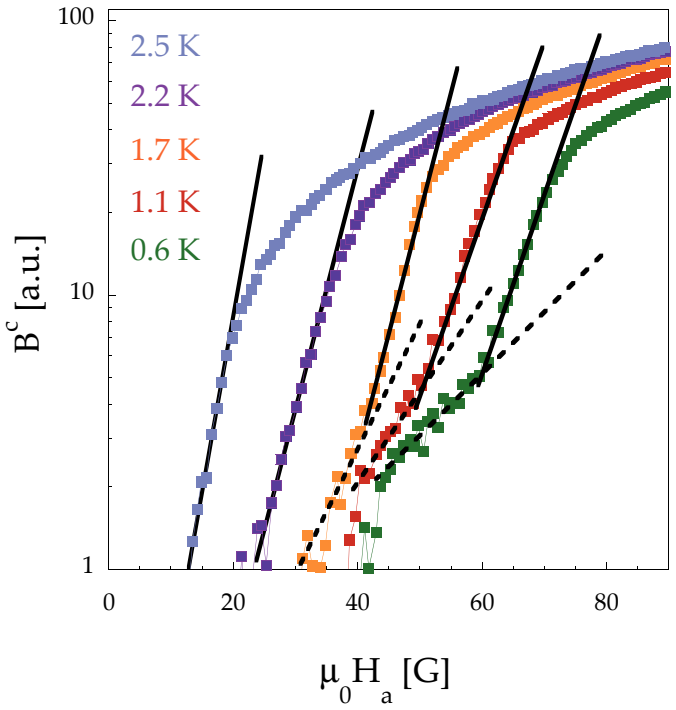

Figure 6.58: Field dependence of B^c at $\theta = 15°$ measured at the indicated temperatures in sample E. $H_k(15°)$ has been identified as the field corresponding to the fast increase in B^c (thick black lines). A small finite B^c increase for $H_a \geq H_p$ (dashed black lines) is visible only for temperatures $T \leq 1.7$ K.

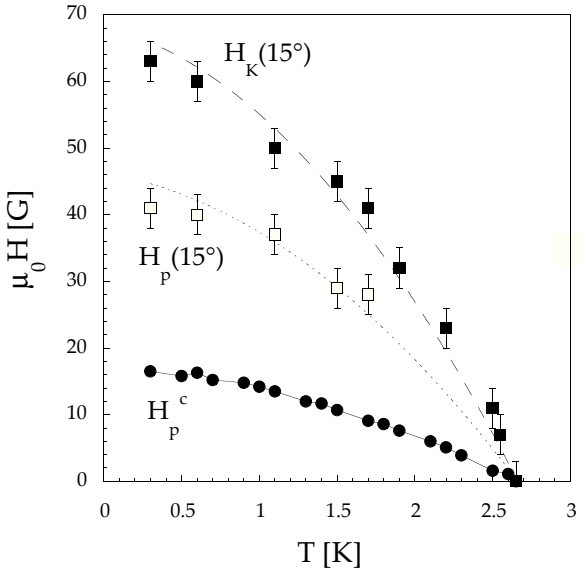

Figure 6.59: Temperature dependence od H_p^c (closed circles), $H_p(15°)$ (open squares) and $H_k(15°)$ (closed squares) obtained for sample E. The dotted and dashed line correspond to $H_p^c/\alpha(15°)$ and $H_p^c/\sin 15°$, respectively.

visible for $T \leq 1.7$ K and the penetration field $H_p(15°)$ could hence not be detected anymore above this temperature. Figure 6.59 displays the temperature dependencies of H_p^c, $H_p(15°)$ and $H_k(15°)$ (again for sample E as an example). The dotted line was constructed by multiplying the measured $H_p^c(T)$ data by $\alpha^c/\alpha(15°)$ confirming that $H_p^c\alpha^c/\alpha(15°) = H_{c1}^c/\alpha(15°) \sim H_p(15°)$ as for $\theta_H = 15°$ the value of $H_p(15°)$ is close to H_p^c. On the other hand, the dashed line in Fig.6.59 corresponds to $H_p^c/\sin(15°)$, clearly showing that the strong lock-in effect persists all the way up to T_c with $\lambda \sim 1$ on the entire temperature range.

6.4 Conclusion

The local Hall probe magnetometry measurements in various orientations of applied field revealed the presence of an unexpected lock-in effect in Cu_xTiSe_2 samples with different copper doping and geometry. As was already mentioned, the intrinsic lock-in effect is not possible in this system due to small values of anisotropy and Ginzburg-Landau parameter. Good agreement with the data was found using a model of Blatter, considering the effect of an additional layered structure, where superconductivity is suppressed, present in the material. The model was modified to be applicable for an

arbitrary angle and anisotropic superconductors. The strength of the lock-in effect was found to be extremely high and by investigating three samples with different copper content we also found that it is independent of the copper content. Our results therefore showed that in Cu_xTiSe_2 an additional layered structure exists, where superconductivity is strongly suppressed.

The origin of this structure remains unknown, however it could be related to the recent findings of Kogar *et al.* [4]. By X-ray measurements, they observed that charge density waves present in Cu_xTiSe_2 become incommensurate with the crystal lattice due to the appearance of domain walls or stacking faults in the system. Their periodicity in c direction of ~ 22 layers is in remarkable agreement with the coherence length in c direction. If the domain walls caused suppression of the superconducting order parameter, this structure could cause the appearance of the lock-in effect. Such a variation of the order parameter along the c direction, could also lead to the presence of two energy scales in the system and observation of two superconducting gaps in the energy spectrum (see Chapter 5). Kogar *et al.* observed that the incommensurate phase emerges at the same copper concentration as superconductivity in Cu_xTiSe_2, and persists to the highest concentrations without change in its critical temperature. Coincidentally, the strength of the lock-in effect and the presence of two gaps are also both doping independent. However, the origin of the lock-in effect and two energy gaps in Cu_xTiSe_2 still has to be clarified.

Summary of the results

In this work we studied the superconducting single crystals of Cu_xTiSe_2 with copper doping from $x = 0.052$ to $x = 0.092$, thus covering large part of the superconducting dome in the phase diagram. Miniature Hall probes were used to determine locally magnetic field induction B in the superconductor. From the spatial variation of B, we constructed the field profiles at certain applied magnetic fields oriented parallel with the c direction in the sample. The dome shape of the profiles confirmed high quality of the studied samples and their further analysis showed that geometrical barriers play the important role in the vortex penetration into the sample. Therefore, the proper place where to obtain relevant data for determination of the lower critical field H_{c1} was in the middle of the sample, where first vortices that overcome the geometrical barriers appeared. By performing the measurements at different temperatures, we obtained the temperature dependence of H_{c1}, which was found to have the same behaviour for all the studied samples. H_{c1} dependencies were then fitted using a model for the superfluid density, where the only fitting parameter is the coupling ratio, $2\Delta/(k_BT_c)$. We found the best agreement of the model with the data for two energy gap model with gap values $2\Delta_1/k_BT_c \sim 2.4$ and $2\Delta_2/k_BT_c \sim 3.7$ and similar weights. Despite that the presence of the smaller energy gap was proved also by tunnel diode oscillator technique [69], it was not observed in the heat capacity measurements. The simple electronic structure of Cu_xTiSe_2 does not suggest the second superconducting gap either, therefore we argue that its origin might not be related to the electronic structure.

Our local Hall probe magnetometry measurements in various orientations of applied field revealed the presence of another interesting phenomenon in Cu_xTiSe_2, an unexpected lock-in effect, when superconducting vortices became locked along the ab planes even for magnetic field oriented away from this direction. Due to small anisotropy and Ginzburg-Landau parameter values, the intrinsic lock-in effect is not possible in this system. In order to analyse our data we extended a model of Blatter

[31] to be used for arbitrary angles and anisotropic superconductor. We found a very good agreement between the data and this model. From the parameters obtained by fitting and those determined directly from the measured data, we constructed the phase diagram of vortex structure in Cu_xTiSe_2. The strength of the observed lock-in effect in Cu_xTiSe_2 was found to be extremely high and the comparison on samples with different doping showed that it is independent on the copper content. The origin of the lock-in effect in Cu_xTiSe_2 remains unknown but it might be related to the recent observation of charge density domain walls structure in this system.

Bibliography

[1] K. Rossnagel, On the origin of charge-density waves in select layered transition-metal dichalcogenides, Journal of Physics: Condensed Matter **23**, 213001 (2011). DOI: 10.1088/0953-8984/23/21/213001

[2] E. Morosan, H. W. Zandbergen, B. S. Dennis, J. W. G. Bos, Y. Onose, T. Klimczuk, A. P. Ramirez, N. P. Ong, R. J. Cava, Superconductivity in Cu_xTiSe_2, Nature Physics **2**, 544 (2006). DOI: 10.1038/nphys360

[3] H. Barath, M. Kim, J. F. Karpus, S. L. Cooper, P. Abbamonte, E. Fradkin, E. Morosan, R. J. Cava, Quantum and Classical Mode Softening Near the Charge-Density-Wave-Superconductor Transition of Cu_xTiSe_2, Physical Review Letters **100**, 106402 (2008). DOI: 10.1103/PhysRevLett.100.106402

[4] A. Kogar, G. A. de la Pena, Sangjun Lee, Y. Fang, S. X.-L. Sun, D. B. Lioi, G. Karapetrov, K. D. Finkelstein, J. P. C. Ruff, P. Abbamonte, S. Rosenkranz, Observation of a Charge Density Wave Incommensuration Near the Superconducting Dome in Cu_xTiSe_2, Physical Review Letters **118**, 027002 (2017). DOI: 10.1103/PhysRevLett.118.027002

[5] F. London, H. London, The Electromagnetic Equations of the Supraconductor, Proceedings of the Royal Society A: Mathematical, Physical and Engineering Sciences **149**, 71 (1935). DOI: 10.1098/rspa.1935.0048

[6] V. L. Ginzburg, L. D. Landau, To the Theory of Superconductivity, Zhurnal Eksperimentalnoi i Teoreticheskoi Fiziki **20**, 1064 (1950).

[7] E. Maxwell, Isotope Effect in the Superconductivity of Mercury, Physical Review **78**, 477 (1950). DOI: 10.1103/PhysRev.78.477

[8] J. Bardeen, L. N. Cooper, J. R. Schrieffer, Theory of superconductivity, Physical review **108**, 1175 (1957). DOI: 10.1103/PhysRev.108.1175

[9] M. Tinkham, Introduction to Superconductivity, second edition, Dover Publications, Inc., Mineola, New York, USA (2004), ISBN-13:978-0-486-43503-9 ISBN-10:0-486-43503-2

[10] A. Carrington, F. Manzano, Magnetic penetration depth of MgB_2, Physica C **385**, 205 (2003). DOI: 10.1016/S0921-4534(02)02319-5

[11] D. A. Wright, J. P. Emerson, B. F. Woodfield, J. E. Gordon, R. A. Fisher, N. E. Phillips, Low-Temperature Specific Heat of $YBa_2Cu_3O_{7-\delta}$, $0 \leq \delta \leq 0.2$: Evidence for d-Wave Pairing, Physical Review Letters **82**, 1550 (1999). DOI: 10.1103/PhysRevLett.82.1550

[12] F. Manzano, A. Carrington, N. E. Hussey, S. Lee, A. Yamamoto, S. Tajima, Exponential Temperature Dependence of the Penetration Depth in Single Crystal MgB_2, Physical Review Letters **88**, 047002 (2002). DOI: 10.1103/PhysRevLett.88.047002

[13] J. D. Fletcher, A. Carrington, P. Diener, P. Rodière, J. P. Brison, R. Prozorov, T. Olheiser, R. W. Giannetta, Penetration Depth Study of Superconducting Gap Structure of $2H$-$NbSe_2$, Physical Review Letters **98**, 057003 (2007). DOI: 10.1103/PhysRevLett.98.057003

[14] V. G. Kogan, Uniaxial superconducting particle in intermediate magnetic fields, Physical Review B **38**, 7049 (1988). DOI: 10.1103/PhysRevB.38.7049

[15] P. A. Mansky, P. M. Chaikin, R. C. Haddon, Vortex Lock-in state in a layered Superconductor, Physical Review Letters **70**, 1323 (1993). DOI: 10.1103/PhysRevLett.70.1323

[16] D. Feinberg, A. M. Ettouhami, The lock-in transition of vortices in layered superconductors, International Journal of Modern Physics B **7**, 2085 (1993). DOI: 10.1142/S0217979293002791

[17] Y. Nakamura, S. Uchida, Anisotropic transport properties of single-crystal $La_{2-x}Sr_xCuO_4$: Evidence for the dimensional crossover, Physical Review B **47**, 8369 (1993). DOI: 10.1103/PhysRevB.47.8369

[18] Z. X. Gao, E. Osquiguil, M. Maenhoudt, B. Wuyts, S. Libbrecht, Y. Bruynseraede, 3D-2D Dimensional Crossover in $YBa_2Cu_3O_7$ Films, Physical Review Letters **71**, 3210 (1993). DOI: 10.1103/PhysRevLett.71.3210

[19] C. S. L. Chun, G.-G. Zheng, J. L. Vicent, I. K. Schuller, Dimensional crossover in superlattice superconductors, Physical Review B **29**, 4915 (1984). DOI: 10.1103/PhysRevB.29.4915

[20] S. T. Ruggiero, T. W. Barbee, Jr., M. R. Beasley, Superconductivity in Quasi-Two-Dimensional Layered Composites, Physical Review Letters **45**, 1299 (1980). DOI: 10.1103/PhysRevLett.45.1299

[21] L. N. Bulaevskii, Macroscopical theory of layered superconductors, International Journal of Modern Physics B **4** 11, 1849 (1990). DOI: 10.1142/S0217979290000905

[22] J. R. Clem, Fundamentals of Vortices in the High-Temperature Superconductors, Superconductor Science and Technology **5**, S33 (1992). DOI: 10.1088/0953-2048/5/1S/006

[23] E. H. Brandt, Properties of the ideal Ginzburg-Landau vortex lattice, Physical Review B **68**, 054506 (2003). DOI: 10.1103/PhysRevB.68.054506

[24] A. Sudbø, E. H. Brandt, D. A. Huse, Multiple Coexisting Orientations of Flux Lines in Superconductors with Uniaxial Anisotropy, Physical Review Letters **71**, 1451 (1993). DOI: 10.1103/PhysRevLett.71.1451

[25] C. A. Bolle, P. L. Gammel, D. G. Grier, C. A. Murray, D. J. Bishop, D. B. Mitzi, A. Kapitulnik, Observation of a Commensurate Array of Flux Chains in Tilted Flux Lattices in Bi-Sr-Ca-Cu-O Single Crystals, Physical Review Letters **66**, 112 (1991). DOI: 10.1103/PhysRevLett.66.112

[26] D. Feinberg, Theory of the tilted vortex lattice in Josephson-coupled layered superconductors, Physica C **194**, 126 (1992). DOI: 10.1016/0921-4534(92)90680-B

[27] L. N. Bulaevskii, M. Ledvij, V. G. Kogan, Vortices in layered superconductors with Josephson coupling, Physical Review B **46**, 366 (1992). DOI: 10.1103/PhysRevB.46.366

[28] W. K. Kwok, U. Welp, V. M. Vinokur, S. Fleshler, J. Downey, G. W. Crabtree, Direct Observation of Intrinsic Pinning by Layered Structure in Single-Crystal $Yba_2Cu_3O_{7-\delta}$, Physical Review Letters **67**, 390 (1991). DOI: 10.1103/PhysRevLett.67.390

[29] L. N. Bulaevskii, Anomalous behaviour of torque at high angles in high-temperature superconductors, Physical Review B **44**, 910 (1991). DOI: 10.1103/PhysRevB.44.910

[30] D. E. Farrell, J. P. Rice, D. M. Ginsberg, J. Z. Liu, Experimental Evidence of a Dimensional Crossover in $Y_1Ba_2Cu_3O_{7-\delta}$, Physical Review Letters **64**, 1573 (1990). DOI: 10.1103/PhysRevLett.64.1573

[31] G. Blatter, M. V. Feigel'man, V. B. Geshkenbein, A. I. Larkin, V. M. Vinokur, Vortices in high-temperature superconductors, Reviews of Modern Physics **66**, 1125 (1994). DOI: 10.1103/RevModPhys.66.1125

[32] G. J. Dolan, G. V. Chandrashekhar, T. R. Dinger, C. Feild, F. Holtzberg, Vortex Structure in $YBa_2Cu_3O_7$ and Evidence for Intrinsic Pinning, Physical Review Letters **62**, 827 (1989). DOI: 10.1103/PhysRevLett.62.827

[33] M. D. Johannes, I. I. Mazin, Fermi surface nesting and the origin of charge density waves in metals, Physical Review B **77**, 165135 (2008). DOI: 10.1103/PhysRevB.77.165135

[34] H. P.Hughes, Structural distortion in $TiSe_2$ and related materials - a possible Jahn-Teller effect?, Journal of Physics C: Solid State Physics, **10**, L319 (1997). DOI: 10.1088/0022-3719/10/11/009

[35] T. E. Kidd, T. Miller, M. Y. Chou, T.-C. Chiang, Electron-Hole Coupling and the Charge Density Wave Transition in $TiSe_2$, Physical Review Letters **88**, 226402. DOI: 10.1103/PhysRevLett.88.226402

[36] N. F. Mott, The Transition to the Metallic State, Philosophical Magazine **6**, 287 (1961). DOI: 10.1080/14786436108243318

[37] C. Monney, C. Battaglia, H. Cercellier, P. Aebi, H. Beck, Exciton Condensation Driving the Periodic Lattice Distortion of $1T$-$TiSe_2$, Physical Review Letters **106**, 106404 (2011). DOI: 10.1103/PhysRevLett.106.106404

[38] Y. Wakisaka, T. Sudayama, K. Takubo, T. Mizokawa, N. L.Saini, M. Arita, H. Namatame, M. Taniguchi, N. Katayama, M. Nohara, H. Takagi, Photoemission Spectroscopy of Ta_2NiSe_5, Journal of Superconductivity and Novel Magnetism **25**, 1231 (2012). DOI: 10.1007/s10948-012-1526-0

[39] R. A. Klemm, Pristine and intercalated transition metal dichalcogenide superconductors, Physica C **514**, 86 (2015). DOI: 10.1016/j.physc.2015.02.023

[40] E. Boaknin, M. A. Tanatar, J. Paglione, D. Hawthorn, F. Ronning, R. W. Hill, M. Sutherland, L. Taillefer, J. Sonier, S. M. Hayden, J. W. Brill, Heat Conduction in the Vortex State of $NbSe_2$: Evidence for Multiband Superconductivity, Physical Review Letters **90**, 117003 (2003). DOI: 10.1103/PhysRevLett.90.117003

[41] T. Yokoya, T. Kiss, A. Chainani, S. Shin, M. Nohara, H. Takagi, Fermi Surface Sheet-Dependent Superconductivity in $2H$-$NbSe_2$, Science **294**, 2518 (2001). DOI: 10.1126/science.1065068

[42] D. E.Moncton, J. D. Axe, F. J. DiSalvo, Study of Superlattice Formation in $2H$-$NbSe_2$ and $2H$-$TaSe_2$ by Neutron Scattering, Physical Review Letters **34**, 734 (1975). DOI: 10.1103/PhysRevLett.34.734

[43] S. V. Borisenko, A. A. Kordyuk, V. B. Zabalotnyy, D. S. Inosov, D. Evtushinsky, B. Büchner, A. N. Yaresko, A. Varykhalov, R. Follath, W. Eberhardt, L. Patthey, H. Berger, Two Energy Gaps and Fermi-Surface "Arcs" in $NbSe_2$, Physical Review Letters **102**, 166402 (2009). DOI: 10.1103/PhysRevLett.102.166402

[44] T. F. Smith, L. E. Delong, A. R. Moodenbough, T. H. Geballe, R. E. Schwall, Superconductivity of $NbSe_2$ to 140 kbar, Journal of Physics C: Solid State Physics **5**, L230 (1972). DOI: 10.1088/0022-3719/5/16/008

[45] M. Leroux, I. Errea, M. Le Tacon, S.-M. Souliou, G. Garbarino, L. Cario, A. Bosak, F. Mauri, M. Calandra, P. Rodière, Strong anharmonicity induces quantum melting of charge density wave in $2H$-$NbSe_2$ under pressure, Physical Review B **92**, 140303(R) (2015). DOI: 10.1103/PhysRevB.92.140303.

[46] M. Leroux, M. Le Tacon, M. Calandra, L. Cario, M-A. Méasson, P.Diener, E. Borrisenko, A. Bosak, P. Rodière, Anharmonic suppression of charge density waves in $2H$-NbS_2, Physical Review B **86**, 155125 (2012). DOI: 10.1103/PhysRevB.86.155125

[47] B. Sipos, A. F. Kusmartseva, A. Akrap, H. Berger, L. Forró, E. Tutiš, From Mott state to superconductivity in $1T$-TaS_2, Nature Materials **7**, 960 (2008). DOI: 10.1038/nmat2318

[48] Y. Liu, R. Ang, W. J. Lu, W. H. Song, L. J. Li, Y. P. Sun, Superconductivity induced by Se-doping in layered charge-density-wave system $1T$-$TaS_{2-x}Se_x$, Applied Physics Letters **102**, 192602 (2013). DOI: 10.1063/1.4805003

[49] D. S. Inosov, V. B. Zabolotnyy, D. V. Evtushinsky, A. A. Kordyuk, B. Büchner, R. Follath, H. Berger, S. V. Borisenko, Fermi surface nesting in several transition metal dichalcogenides, New Journal of Physics **10**, 125027 (2008). DOI: 10.1088/1367-2630/10/12/125027

[50] H. Mutka, Superconductivity in irradiated charge-density-wave compounds $2H$-$NbSe_2$, $2H$-TaS_2, and $2H$-$TaSe_2$, Physical Review B **28**, 2855 (1983). DOI: 10.1103/PhysRevB.28.2855

[51] F. J. Di Salvo, D. E. Moncton, J. V. Waszczak, Electronic properties and snperlattice formation in the semimetal $TiSe_2$, Physical Review B **14**, 4321 (1976). DOI: 10.1103/PhysRevB.14.4321

[52] H. Cercellier, C. Monney, F. Clerc, C. Battaglia, L. Despont, M. G. Garnier, H. Beck, P. Aebi, L. Patthey, H. Berger a L. Forró, Evidence for an Excitonic Insulator Phase in $1T$-$TiSe_2$, Physical Review Letters **99**, 146403 (2007). DOI: 10.1103/PhysRevLett.99.146403

[53] J. van Wezel, P. Nahai-Williamson, S. S. Saxena, Exciton-phonon-driven charge density wave in $TiSe_2$, Physical Review B **81**, 165109 (2010). DOI: 10.1103/PhysRevB.81.165109

[54] A. F. Kusmartseva, B. Sipos, H. Berger, L. Forró, E. Tutiš, Pressure Induced Superconductivity in Pristine $1T$-$TiSe_2$, Physical Review Letters **103**, 236401 (2009). DOI: 10.1103/PhysRevLett.103.236401

[55] J. F. Zhao, H. W. Ou, G. Wu, B. P. Xie, Y. Zhang, D. W. Shen, J. Wei, L. X. Yang, J. K. Dong, M. Arita, H. Namatame, M. Taniguchi, X. H. Chen, D. L. Feng, Evolution of the Electronic Structure of $1T$-Cu_xTiSe_2, Physical Review Letters **99**, 146401 (2007). DOI: 10.1103/PhysRevLett.99.146401

[56] M. Monteverde, J. Lorenzana, P. Monceau, M. Núñez-Regueiro, Quantum critical point and superconducting dome in the pressure phase diagram of o-TaS_3, Physical Review B **88**, 180504(R) (2013). DOI: 10.1103/PhysRevB.88.180504

[57] X. L. Wu, C. M. Lieber, Hexagonal Domain-Like Charge Density Wave Phase of TaS_2 Determined by Scanning Tunneling Microscopy, Science **243**, 1703 (1989). DOI: 10.1126/science.243.4899.1703

[58] S. Y. Li, G. Wu, X. H. Chen, L. Taillefer, Single-Gap s-Wave Superconductivity near the Charge-Density-Wave Quantum Critical Point in Cu_xTiSe_2, Physical Review Letters **99**, 107001 (2007). DOI: 10.1103/PhysRevLett.99.107001

[59] B. Batlogg, R. J. Cava, L. W. Rupp Jr., G. P. Espinosa, J. J. Krajewski, W. F. Peck Jr., A. S. Cooper, Superconductivity in Bi-O and Sb-O perovskites, Physica C **162-164**, 1393 (1989). DOI: 10.1016/0921-4534(89)90748-X

[60] J. Kačmarčík, Z. Pribulová, V. Paľuchová, P. Szabó, P. Husaníková, G. Karapetrov, P. Samuely, Heat capacity of single-crystal Cu_xTiSe_2 superconductors, Physical Review B **88**, 020507(R) (2013). DOI: 10.1103/PhysRevB.88.020507

[61] J. Kačmarčík, Z. Pribulová, C. Marcenat, T. Klein, P. Rodière, L. Cario, P. Samuely, Specific heat measurements of a superconducting NbS_2 single crystal in an external magnetic field: Energy gap structure, Physical Review B **82**, 014518 (2010). DOI: 10.1103/PhysRevB.82.014518

[62] L. Lyard, P. Samuely, P. Szabo, T. Klein, C. Marcenat, L. Paulius, K. H. P. Kim, C. U. Jung, H. -S. Lee, B. Kang, S. Choi, S. -I. Lee, J. Marcus, S. Blanchard, A. G. M. Jansen, U. Welp, G. Karapetrov, W. K. Kwok, Anisotropy of the upper critical field and critical current in single crystal MgB_2, Physical Review B **66** 180502(R) (2002). DOI: 10.1103/PhysRevB.66.180502

[63] A. D. Hillier, P. Manuel, D. T. Adroja, J. W. Taylor, A. K. Azad, J. T. S. Irvine, Probing the superconducting ground state near the charge density wave phase transition in $Cu_{0.06}TiSe_2$, Physical Review B **81**, 092507 (2010). DOI: 10.1103/PhysRevB.81.092507

[64] M. Zaberchik, K. Chashka, L. Patlgan, A. Maniv, C. Baines, P. King, A. Kanigel, Possible evidence of a two-gap structure for the Cu_xTiSe_2 superconductor, Physical Review B **81**, 220505(R) (2010). DOI: 10.1103/PhysRevB.81.220505

[65] E. H. Brandt, Geometric barrier and current string in type-II superconductors obtained from continuum electrodynamics, Physical Review B **59**, 3369 (1999). DOI: 10.1103/PhysRevB.59.3369

[66] E. Zeldov, A. I. Larkin, V. B. Geshkenbein, M. Konczykowski, D. Majer, B. Khaykovich, V. M. Vinokur, H. Shtrikman, Geometrical Barriers in High-Temperature Superconductors, Physical Review Letters **73**, 1428 (1994). DOI: 10.1103/PhysRevLett.73.1428

[67] C. P. Bean, J. D. Livingston, Surface barrier in type-II superconductors, Physical Review Letters **12**, 14 (1964). DOI: 10.1103/PhysRevLett.12.14

[68] E. H. Brandt, G. P. Mikitik, E. Zeldov, Two Regimes of Vortex Penetration into Platelet-Shaped Type-II Superconductors, Journal of Experimental and Theoretical Physics **117**, 439 (2013). DOI: 10.1134/S1063776113110010

[69] Z. Pribulová, Z. Medvecká, J. Kačmarčík, V. Komanický, T. Klein, P. Rodière, F. Levy-Bertrand, B. Michon, C. Marcenat, P. Husaníková, V. Cambel, J. Šoltýs, G. Karapetrov, S. Borisenko, D. Evtushinsky, H. Berger, P. Samuely, Magnetic and thermodynamic properties of Cu_xTiSe_2 single crystals, Physical Review B **95**, 174512 (2017). DOI: 10.1103/PhysRevB.95.174512

[70] C. S. Oglesby, E. Bucher, C. Kloc, H. Hohl, Growth of faceted niobium diselenide, Journal of Crystal Growth **137**, 289 (1994). DOI: 10.1016/0022-0248(94)91287-4

[71] Z. Pribulová, Z. Medvecká, J. Kačmarčík, V. Komanický, T. Klein, P. Husaníková, V. Cambel, J. Šoltýs, G. Karapetrov, P. Samuely, Local Magnetometry of $Cu_{0.064}TiSe_2$, Acta Physica Polonica A **126**, 370 (2014). DOI: 10.12693/APhysPolA.126.370

[72] L. Lyard, T. Klein, J. Marcus, R. Brusetti, C. Marcenat, M. Konczykowski, V. Mosser, K. H. Kim, B. W. Kang, H. S. Lee, S. I. Lee, Geometrical barriers and lower critical field in MgB_2 single crystals, Physical Review B **70**, 180504(R) (2004). DOI: 10.1103/PhysRevB.70.180504

[73] F. Levy-Bertrand, B. Michon, J. Marcus, C. Marcenat, J.Kačmarčík, T. Klein, H. Cercellier, Puzzling evidence for surface superconductivity in the layered dichalcogenide $Cu_{10\%}TiSe_2$, Physica C **523**, 19 (2016). DOI: 10.1016/j.physc.2016.02.004

[74] D. V. Evtushinsky, D. S. Inosov, V. B. Zabolotnyy, M. S. Viazovska, R. Khasanov, A. Amato, H.-H. Klauss, H. Luetkens, Ch. Niedermayer, G. L. Sun, V. Hinkov, C. T. Lin, A. Varykhalov, A. Koitzsch, M. Knupfer, B. Büchner, A. A. Kordyuk, S. V. Borisenko, Momentum-resolved superconducting gap in the bulk of

$Ba_{1-x}K_xFe_2As_2$ from combined ARPES and μSR measurements, New Journal of Physics **11**, 055069 (2009). DOI: 10.1088/1367-2630/11/5/055069

[75] P. Rodière, T. Klein, L. Lemberger, K. Hasselbach, A. Demuer, J. Kačmarčík, Z. S. Wang, H. Q. Luo, X. Y. Lu, H. H. Wen, F. Gucmann, C. Marcenat, Scaling of the physical properties in $Ba(Fe,Ni)_2As_2$ single crystals: Evidence for quantum fluctuations, Physical Review B **85**, 214506 (2012). DOI: 10.1103/PhysRevB.85.214506

[76] Z. Medvecká, T. Klein, V. Cambel, J. Šoltýs, G. Karapetrov, F. Levy-Bertrand, B. Michon, C. Marcenat, Z. Pribulová, P. Samuely, Observation of a transverse Meissner effect in Cu_xTiSe_2 single crystals, Physical Review B **93**, 100501(R) (2016). DOI: 10.1103/PhysRevB.93.100501

[77] G. Blatter, J. Rhyner, V. M. Vinokur, Vortex pinning by twin boundaries in copper oxide superconductors, Physical Review B **43**, 7826 (1991). DOI: 10.1103/PhysRevB.43.7826; A. A. Zhukov, G. K. Perkins, J. V. Thomas, A. D. Caplin, H. Küpfer, T. Wolf, Direct observation of tilted vortex structures induced by twin boundaries in $YBa_2Cu_3O_y$ single crystals, Physical Review B **56**, 3481 (1997). DOI: 10.1103/PhysRevB.56.3481

List of publications

Magnetic and thermodynamic properties of Cu_xTiSe_2 single crystals.
Z. Pribulová, Z. Medvecká, J. Kačmarčík, V. Komanický, T. Klein, P. Rodière, F. Levy-Bertrand, B. Michon, C. Marcenat, P. Husaníková, V. Cambel, J. Šoltýs, G. Karapetrov, S. Borisenko, D. Evtushinsky, H. Berger, P. Samuely,
Physical Review B **95**, 174512 (2017). DOI: 10.1103/PhysRevB.95.174512

Observation of a transverse Meissner effect in Cu_xTiSe_2 single crystals.
Z. Medvecká, T. Klein, V. Cambel, J. Šoltýs, G. Karapetrov, F. Levy-Bertrand, B. Michon, C. Marcenat, Z. Pribulová, P. Samuely,
Physical Review B **93**, 100501(R) (2016). DOI: 10.1103/PhysRevB.93.100501

Local Magnetometry of $Cu_{0.064}TiSe_2$.
Z. Pribulová, Z. Medvecká, J. Kačmarčík, V. Komanický, T. Klein, P. Husaníková, V. Cambel, J. Šoltýs, G. Karapetrov, P. Samuely,
Acta Physica Polonica A **126**, 370 (2014). DOI: 10.12693/APhysPolA.126.370

Comparison of the lock-in effect in different Cu_xTiSe_2 single crystals.
Z. Medvecká, T. Klein, V. Cambel, J. Šoltýs, G. Karapetrov, F. Levy-Bertrand, B. Michon, Z. Pribulová, P. Samuely,
- under consideration in Physical Review B

List of conferences and courses

September 26^{th} - October 3^{rd}, 2016

Cryocourse 2016, *Espoo, Finland*

- School and Workshop in Cryogenics and Quantum Engineering

- participant

September 3^{rd} - 7^{th}, 2016

Nano-SC 2016, *Garmisch-Partenkirchen, Germany*

- Nano confined superconductors and their application

- poster presentation: Observation of lock-in effect in Cu_xTiSe_2 via local Hall probe magnetometry

June 13^{th} - 17^{th}, 2016

CSMAG'16, *Košice, Slovakia*

- 16^{th} Czech and Slovak Conference on Magnetism

- poster presentation: Comparison of lock-in effect in different Cu_xTiSe_2 single crystals

August 23^{rd} - August 28^{th}, 2015

M^2S 2015, Geneva, Switzerland

- Materials and Mechanisms if Superconductivity

- poster presentation: Lock-in effect in Cu_xTiSe_2 single crystals

September 21^{st} - 26^{th}, 2013

VORTEX VIII

- Eighth international conference on vortex matter in nanostructured superconductors

- poster presentation: Local Magnetometry of Cu_xTiSe_2

June 17^{th} - 21^{st}, 2013

CSMAG'13, *Košice, Slovakia*

- 15^{th} Czech and Slovak Conference on Magnetism

- poster presentation: Local magnetometry of Cu_xTiSe_2

Résumé de la thèse

Introduction

Dans de nombreux systèmes non conventionnels, la supraconductivité apparaît au voisinage d'une autre instabilité magnétique ou électronique et l'interaction entre la supraconductivité et ces autres états ordonnés est au centre de la recherche en physique du solide moderne. Cu_xTiSe_2 appartient à la famille des dichlorogénures de métaux de transition, caractérisés par la présence de supraconductivité et d'une onde de densité de charge (Charge Density Wave - CDW) [1]. Comme le montre le diagramme de phase électronique de Cu_xTiSe_2 (*température versus dopage en cuivre*) [2], la CDW est présente dans $1T$-$TiSe_2$ (au dessous de $\sim$ 200 K) mais semble disparaître progressivement lorsque le dopage en cuivre augmente, cédant la place à un dôme supraconducteur. Ce diagramme indique que l'état CDW pourrait alors disparaître complètement pour une concentration en cuivre, pour laquelle la température critique de la supraconductivité est maximale, définissant l'emplacement d'un point critique quantique pour la CDW [3]. Cependant, de récentes mesures de diffraction de rayons X [4] ont montré que ce n'était pas le cas. Ils ont observé que des parois du domaine et/ou des défauts d'empilement apparaissent et que l'état CDW devient incommensurable mais persiste sous le dôme supraconducteur, et ce jusqu'à la concentration en cuivre la plus élevée. La périodicité de cette structure est très proche de la longueur de cohérence (ξ_c) et la concomitance de la supraconductivité et de l'état CDW suggère que cette dernière pourrait affecter la supraconductivité dans Cu_xTiSe_2.

Au cours de ce travail, je présenterai les résultats de mesures d'aimantation locales à sonde de Hall effectuées sur des monocristaux de Cu_xTiSe_2 pour différentes teneurs en cuivre. Tout d'abord, nous avons construit les profils de champ magnétique pour déterminer l'entrée des premiers vortex dans l'échantillon. Ces profils ont permis de déterminer le champ critique inférieur, H_{c1}(T). En utilisant les résultats de mesures de chaleur spécifique précédemment effectuées sur ces échantillons, nous avons obtenu les dépendances en dopage des deux champs critiques et donc des longueurs fondamentale, λ et ξ. Dans un second temps, je présenterai les résultats de mesures d'aimantation locale obtenues pour différentes orientations du champ magnétique appliqué. Ces mesures ont révélé la présence d'un effet dit de lock-in, conformes au modèle de Blatter, qui a été modifié pour pouvoir être appliqué dans notre cas. Ces effets de lock-in ont été comparées sur trois échantillons de teneur en cuivre différentes.

1. Cu_xTiSe_2

Cu_xTiSe_2 est obtenu par intercalation de cuivre entre les couches de $1T$-$TiSe_2$, qui appartient au groupe des dichlorogénures de métaux de transition (Transition Metal Dichalcogenides - TMD). Les TMD sont caractérisés par une structure complexe et un caractère quasi 2-dimensionnel. En fonction de leur composition, ils peuvent être des semi-conducteurs (par exemple MoS_2, WS_2), semimétalliques (par exemple WTe_2, $TiSe_2$) ou de "bons" métaux (par exemple NbS_2, VSe_2). À basses températures, certains d'entre eux deviennent supraconducteurs, avec des propriétés similaires à celles des autres supraconducteurs non conventionnels (voir la référence [1] pour une revue). Par exemple, certains d'entre eux sont des supraconducteurs à gaps multiples (comme MgB_2) et d'autres présentent un "pseudogap" semblable à celui observé dans les pnictides ou les cuprates.

La plupart des TMD présentent à la fois une onde de densité de charges (CDW) et une phase supraconductrice (SC). Les CDW sont des modulations longitudinales, périodiques de la densité électronique qui peut s'accompagner d'une distorsion du réseau atomique. R. E. Peierls a été le premier à prédire l'existence des CDW, lorsqu'il a découvert une instabilité dans la configuration électronique des métaux unidimensionnels. Considérons le cas d'un matériau avec une bande de conduction à moitié remplie. Lors de la transition de Peierls, une certaine énergie est dépensée pour déplacer les ions de leur position d'équilibre et la constante de réseau passe de a à $2a$. Les limites de la première zone de Brillouin passent alors de $k = \pi/a$ à $k = \pi/2a$ et les électrons de conduction de vecteur d'onde $k \sim \pi/2a$ (demi-remplissage) diffusent alors sur les bords de la première zone de Brillouin. Cette diffusion entraîne l'ouverture d'un gap au niveau de Fermi ainsi que le ramollissement des modes de phonons pour $q = \pi/a$. Les électrons de conduction se décalent vers des niveaux énergétiques plus faibles stabilisant la nouvelle structure. La supraconductivité coexiste habituellement avec une CDW incommensurable (ICDW) pour laquelle le vecteur d'onde caractéristique de la CDW n'est pas un multiple entier du vecteur d'onde de réseau cristallin. La coexistence de la supraconductivité avec une phase CDW proportionnelle (CCDW) est elle relativement rare.

Morosan *et al.* ont effectué une étude complète sur des échantillons polycristallins de Cu_xTiSe_2 [2]. À partir de mesures de résistivité et de susceptibilité magnétique, ils ont déterminé les températures de transition vers la CDW et l'état supraconducteur sur différents échantillons. Le diagramme de phase électronique $T(x)$ correspondant est présenté en Fig.1. En augmentant la concentration en cuivre, l'état CDW diminue et pour $x \geq 0.04$ la phase supraconductrice se développe. La température critique maximale $T_c = 4.15$ K est atteinte pour $x = 0.08$. Au-dessus de cette concentration, T_c diminue et crée un dôme dans le diagramme de phase. La limite de solubilité du cuivre est atteinte pour $x = 0.11$ lorsque l'expansion de la cellule élémentaire s'arrête et que les constantes de réseau deviennent stables. Le dopage optimal pour la supraconductivité est donc $x = 0.08$ (température critique maximale). À cette concentration, Morosan *et al.* n'ont plus observé l'état CDW, ce qui a initialement suggéré que la suppression de la CDW pourrait être liée au développement de la phase SC. Par ailleurs, certains affirment que le dôme SC pourrait être le résultat direct du dopage. T_c augmente dans un premier temps car le cuivre donne des électrons à la bande de conduction, mais lorsque la concentration en cuivre est supérieure à $x > 0.08$, les effets de diffusion deviennent plus importants et T_c

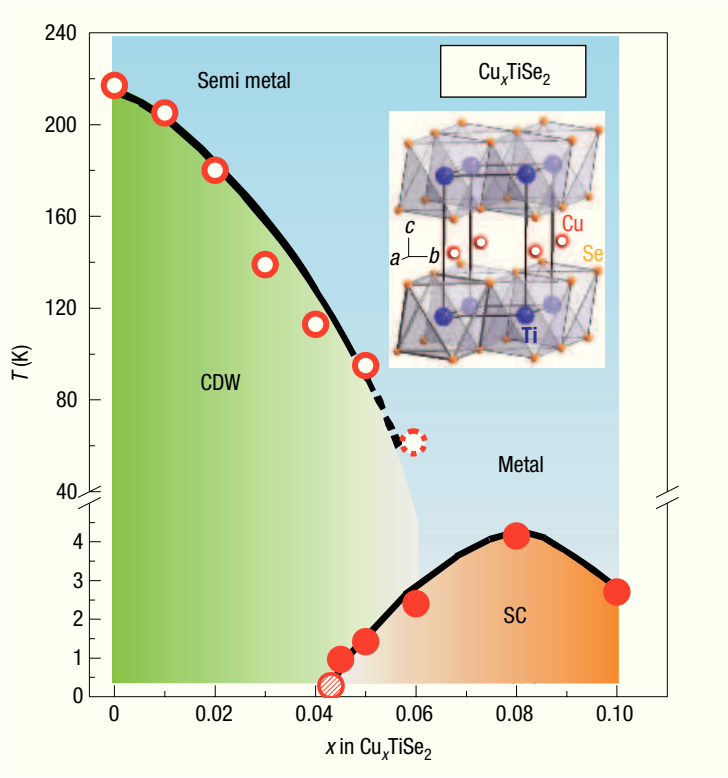

Figure 1: Diagramme de phase électronique de Cu_xTiSe_2 (température en fonction du dopage en cuivre x). Insert: Structure schématique du cristal. [2]

diminue. Cependant, la supraconductivité peut également être introduite dans $1T$-$TiSe_2$ en appliquant une pression hydrostatique [5], ce qui entraîne également l'existence d'un dôme SC mais qui ne peut pas être expliqué par un désordre induit par le dopage.

D'autres relient l'existence du dôme SC à la présence d'un point critique quantique (QCP) où une transition de phase à 0 K (pour la CDW) devrait se produire [3]. En effet, il est tentant de penser que $T_{CDW}(x)$ pourrait s'annuler quelque part autour de $x = 0.08$ et le QCP se trouverait alors à proximité du dopage optimal, au centre du dôme SC. Les expériences récentes de Kogar *et al.* [4], ont cependant réfuté la présence d'un QCP dans ce système. Le groupe a étudié la commensurabilité de l'état CDW par diffraction de rayons X et contrairement à ce qui était attendu auparavant, ils ont constaté que l'état CDW n'est pas supprimé pour un dopage élevé en cuivre, mais que les pics de diffraction de la CDW se décale légèrement pour $x > 0.05$ (lorsque la supraconductivité émerge), montrant que l'état CDW devient incommensurable avec le réseau cristallin (ce décalage correspond à $\sim$ 20 cellules unités). À partir de ces résultats, ils ont construit un nouveau diagramme de phase présenté en Fig.2, qui montre que la phase CDW incommensurable est présente au-dessus de tout le dôme supraconducteur, sa température critique T_{CDW} étant presque constante avec le dopage en cuivre. L'existence de la phase incommensurable dans Cu_xTiSe_2 a été attribuée à la présence de parois de domaines ou à des défauts d'empilement le long de la direction c, déjà connus pour provoquer une légère incommensurabilité dans le vecteur CDW dans $1T$-TaS_2 [6]. Il est intéressant de noter que la périodicité de la structure correspond à la longueur de cohérence de la phase supraconductrice dans la direction c.

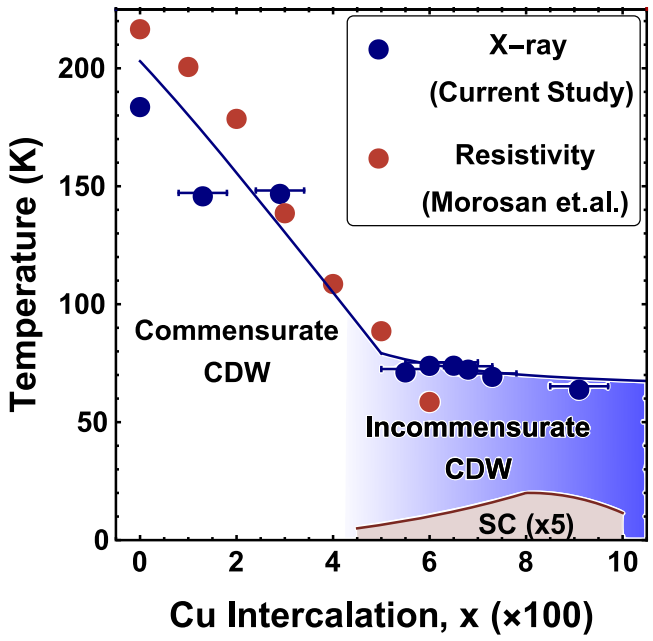

Figure 2: Diagramme de phase électronique pour Cu_xTiSe_2 (en fonction du contenu en cuivre x) montrant la coexistence d'une onde de densité de charge incommensurable et de la supraconductivité. [4]

Malgré sa structure électronique relativement simple, la nature de la supraconductivité dans Cu_xTiSe_2 reste incertaine. Certaines études indiquent qu'il s'agit simplement d'un supraconducteur standard (s-wave) tandis que d'autres suggèrent un comportement non trivial dans l'état supraconducteur. Les mesures de conductivité thermique, κ effectuées par le groupe de Li *et al.* [7] appartiennent à la première catégorie. Ils ont mesuré un cristal légèrement sous-dopé ($Cu_{0.06}TiSe_2$) jusqu'à environ 50 mK, permettant d'obtenir avec précision son terme électronique (linéaire) κ_0. Ils ont alors montré l'absence de terme linéaire résiduel, ($\kappa_0/T \sim 0$ pour $T \to 0$), ce qui est un signe clair d'une supraconductivité classique avec un gap totalement ouvert. En effet dans le cas des supraconducteurs non conventionnels présentant des nœuds dans le gap, les quasi-particules des parties non détruites de la surface de Fermi contribuent à la conductivité thermique et κ_0/T est alors non nulle. Ils ont également obtenu la dépendance en champ de κ_0/T dans $Cu_{0.06}TiSe_2$ et l'ont comparé à des données similaires pour le supraconducteur d-wave Tl2201, des supraconducteurs s-wave (Nb et InBi) et le supraconducteur multibande s-wave $NbSe_2$. lIs en ont conclu que $Cu_{0.06}TiSe_2$ est très probablement (comme InBi) un supraconducteur s-wave sale.

Les mesures de chaleur spécifique effectuées par Morosan *et al.* [2] sur un échantillon à dopage optimal plaident également en faveur d'une supraconductivité conventionnelle. De l'extrapolation de la chaleur spécifique sous champ fort à 0 K, ils ont obtenu une valeur du coefficient de Sommerfeld $\gamma = 4.3$ mJ mol^{-1}K^{-2} et ont alors déterminé l'amplitude du saut de chaleur spécifique à $T = T_c$ pour H=0 : $\Delta C/\gamma T_c = 1.68$, ce qui est légèrement supérieur au rapport à 1.49 attendu dans la limite de couplage faible (théorie BCS) pour un supraconducteur classique s-wave.

Par ailleurs, des mesures de chaleur spécifique pour différents dopages ont également été effectuées par Kačmarčík *et al.* [9]. La figure 3-*Gauche* montre la dépendance en température (renormalisée à T_c) de la différence entre la chaleur spécifique C_s du supraconducteur et celle C_n de l'état normal ($\Delta C/T = C_s/T - C_n/T$) pour quatre échantillons avec des teneurs en cuivre différentes. Toutes les courbes suivent le même comportement sans aucune différence significative dans leur dépendance en température. De plus, la dépendance en température de $C_{es}/\gamma_n T$ (figure 3-*droite*) peut être décrite par la théorie BCS avec un seul paramètre ajustable : $2\Delta/k_B T_c$, où Δ est le gap à 0 K et k_B la constante de Boltzmann. Le meilleur accord entre les données et le modèle a été trouvé pour un gap unique $2\Delta/k_B T_c = 3.7$, légèrement supérieur à la valeur 3.52 attendue dans la théorie BCS. La figure montre également les données obtenues dans le supraconducteur à deux gaps NbS_2 (symboles noirs pleins). Bien que la hauteur du saut de chaleur spécifique soit la même pour les deux matériaux,le comportement global est assez différent, principalement aux températures les plus basses (pour NbS_2, la capacité calorifique commence à augmenter pour des températures plus basses en raison de la présence d'un gap plus faible).

Enfin, des expériences de Muon Spin Rotation (μSR) sur des échantillons de Cu_xTiSe_2 de différentes concentrations en cuivre ont été effectués par le groupe de Zaberchik *et al.*

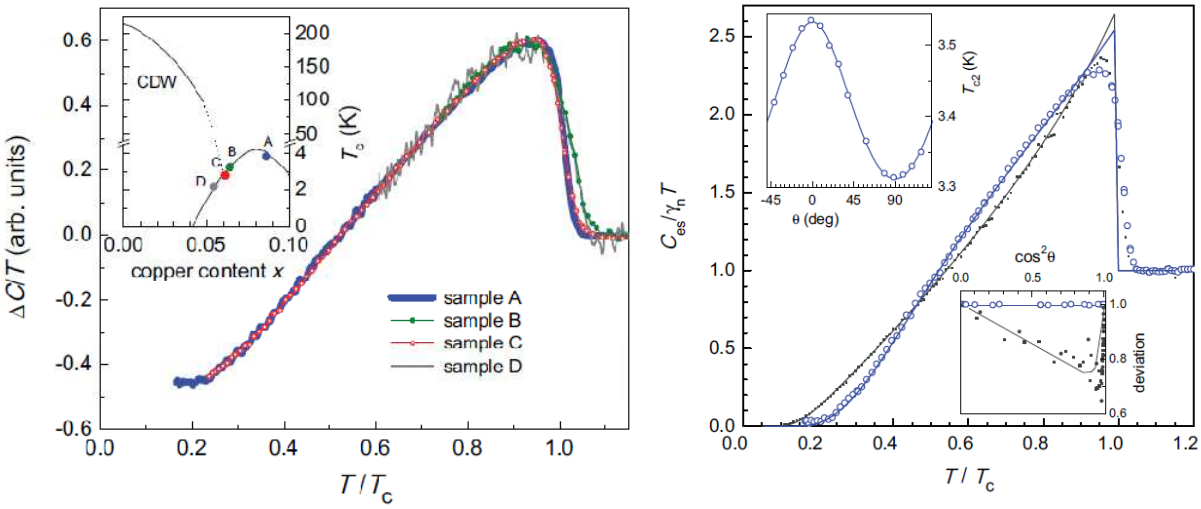

Figure 3: *Gauche* - Dépendance en température de $\Delta C/T$ (voir texte) pour quatre échantillons de Cu_xTiSe_2 avec des taux de dopages en cuivre différents, dans une échelle de température normalisée à T_c. L'encart montre le diagramme de phase obtenu dans ref.[2] (lignes), avec les quatre échantillons mesurés par Kačmarčík *et al.* (cercles complets). *Droite* - Chaleur spécifique électronique dans état supraconducteur pour $Cu_{0.086}TiSe_2$ (cercles bleus) et courbe théorique pour un seul gap (α-model pour $2\Delta/k_B T_c = 3.7$, ligne épaisse) et les données pour NbS_2 (points noirs) [10] avec le modèle correspondant à deux gaps (ligne mince). L'insert supérieur montre la dépendance angulaire de T_c pour $Cu_{0.086}TiSe_2$ (cercles bleus) et l'insert inférieure montre l'écart au modèle anisotrope de GL pour un supraconducteur *s*-wave par rapport à cet écart obtenu pour NbS_2 (points noirs). [9]

[11]. Pour les trois échantillons étudiés (de sous-dopés à dopage optimal), ils ont observé que la surface de Fermi est entièrement gappée. En outre, ils ont déterminé la dépendance en température de la longueur de pénétration λ et ont montré que $\lambda(T)$ pouvait être décrit par une courbe théorique pour un supraconducteur s-wave classique avec $2\Delta/k_BT_c = 3.52$ pour le taux de dopage optimal mais que les données des échantillons sous-dopés s'ajustent mieux aux courbes théoriques pour des rapports de couplage plus petits, $2\Delta/k_BT_c = 3$ et 2.8 pour $x = 0.057$ et $x = 0.044$.

2. Magnétométrie à sonde de Hall

Le champ magnétique a une forte influence sur la supraconductivité et la réponse d'un échantillon au champ magnétique fournit une information importante sur ses propriétés supraconductrices. Le champ magnétique pénètre dans un supraconducteur de type II sous la forme de vortex dont le flux magnétique est quantifié. Ces objets peuvent expérimenter diverses interactions dans l'échantillon et leur distribution n'est pas homogène. Mesurer uniquement la valeur moyenne (globale) de l'induction n'est en général pas suffisant et peut conduire à des erreurs significatives sur la détermination des grandeurs caractéristiques, il faut recourir à des mesures localesdu champ magnétique.

La magnétométrie à sonde locale utilise des sondes de Hall miniatures situées à proximité immédiate de l'échantillon. S'il existe une induction B normale à la surface de la sonde non nul, alors en présence un courant I, une tension Hall, V_{Hall}, est générée à travers la sonde. Un paramètre important caractérisant une sonde de Hall est sa sensibilité s définie comme $s = \Delta V_{Hall}/(I\mu_0\Delta H) = [\Omega\ /\ \mathrm{T}]$, où ΔV_{Hall} est la variation de la tension de Hall induite dans la sonde par une modification du champ magnétique ΔH. Pour pouvoir utiliser aisément une sonde de Hall dans une expérience, il est important que la dépendance en champ magnétique de la tension de Hall soit une fonction linéaire, i.e. que sa sensibilité soit indépendant du champ. Dans ce cas, il est possible de relier simplement la tension de Hall mesurée au champ magnétique local par le biais du coefficient s.

Les données de la Fig.4-*Gauche* montrent un exemple de mesure obtenue sur une sonde de Hall située sous un supraconducteur. Pour les champs magnétiques les plus faible, l'échantillon est dans l'état de Meissner et se comporte comme un diamagnetique parfait expulsant totalement le champ magnétique. Le signal sur la sonde de Hall devrait être nul mais on observe néanmoins une petite augmentation linéaire, causée par une distance non nulle entre l'échantillon et la sonde. Après avoir retiré cette première partie linéaire et l'offset en champ nul, on obtient l'induction $B(H_a)$, présenté en Fig.4-*Droite*. Lorsque le champ appliqué atteint le champ de pénétration H_p, B commence à entrer dans le supraconducteur et la sonde de Hall située en dessous de l'échantillon détecte le champ de ces premiers vortex : une augmentation nette apparaît dans le signal $B(H_a)$. À partir de la zone active de la sonde S, nous pouvons recalculer la quantité de flux magnétique traversant la sonde ($\phi = B \cdot S$) et comme chaque vortex contient exactement un quantum de flux magnétique, $\phi_0 = 2.0678 \cdot 10^{-15}$ Tm^2, B peut être directement lié au nombre de vortex enregistrés par la sonde, $N = \phi/\phi_0$. Une augmentation de 1 G en B équivaut à 5 vortex pour $S = 100\ \mu$m^2. Pour un champ magnétique croissant, de plus en plus de vortex entrent dans l'échantillon jusqu'à ce que le supraconducteur

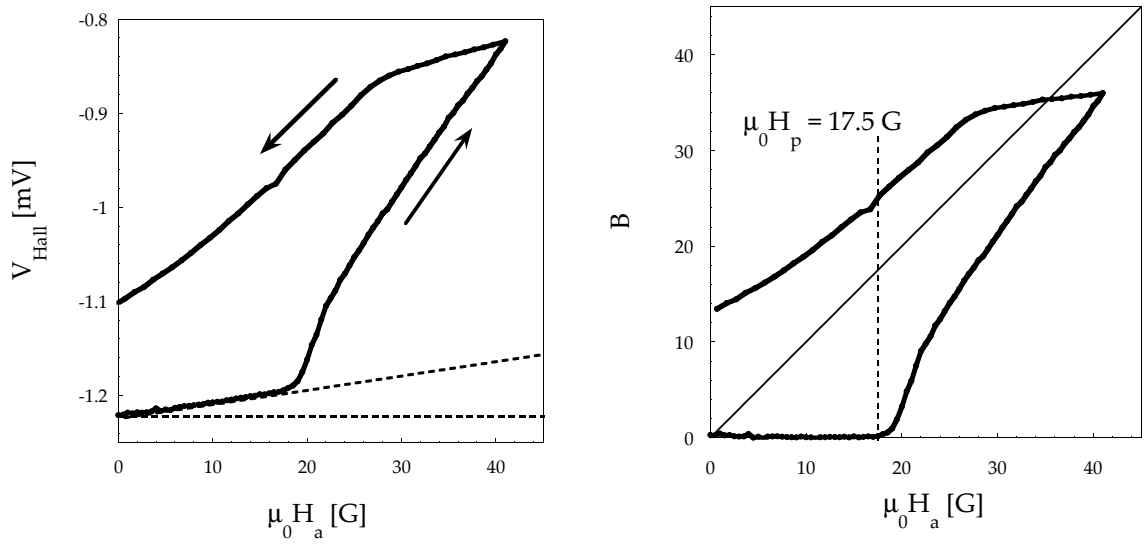

Figure 4: *Gauche* - Dépendance en champ de V_{Hall} mesurée par la sonde de Hall placée sous un échantillon supraconducteur ($I = 50$ μA). Le signal montre un offset à $H_a = 0$ et une petite augmentation linéaire du signal due à une distance non nulle entre l'échantillon et la sonde. *Droite* - La courbe noire montre les données du panneau de *Gauche* après avoir supprimé la première augmentation linéaire et l'offset. La ligne noire fine représente le signal $B = \mu_0 H_a$.

passe dans l'état normal pour le champ critique supérieur H_{c2}. Au delà de cette valeur, l'induction dans l'échantillon est égale au champ appliqué et la courbe $B(H_a)$ se confond avec la ligne droite $B = \mu_0 H_a$. Nous avons utilisé ici 7 sondes de Hall en ligne avec leurs centres séparés de 25 ou 35 μm. Cette ligne des sondes de Hall nous permet d'étudier la distribution du champ magnétique dans l'échantillon supraconducteur, et comme nous le verrons, de déterminer correctement la valeur du champ critique inférieur H_{c1}.

3. Résultats I.

3.1 Les profils de champ magnétique

Au cours de cette thèse j'ai effectué des mesures sur des monocristaux de Cu_xTiSe_2 présentant des teneurs en cuivre, x différentes, déterminées par spectroscopie de rayons X (EDX). Les températures critiques de la transition supraconductrice, T_c ont été obtenues à partir de mesures de chaleur spécifique et les valeurs de x et T_c ont été reportées sur la Fig.5-*Gauche* construite sur les bases du diagramme de phase obtenu par Morosan *et al.* [2]. Les échantillons étudiés allaient donc de sous-dopés à sur-dopés ($0.04 < x < 0.1$), ce qui nous a permis d'étudier l'état supraconducteur sur une grande partie du dôme supraconducteur. Les échantillons ont été préparés par transport d'iode [12], par trois groupes de recherche différents. Les échantillons A, B, C et D ont été préparés dans le groupe de Goran Karapetrov de l'Université Drexel à Philadelphie, les échantillons E et F par Helmuth Berger de l'Ecole Polytechnique Fédérale à Lausanne, et l'échantillon F

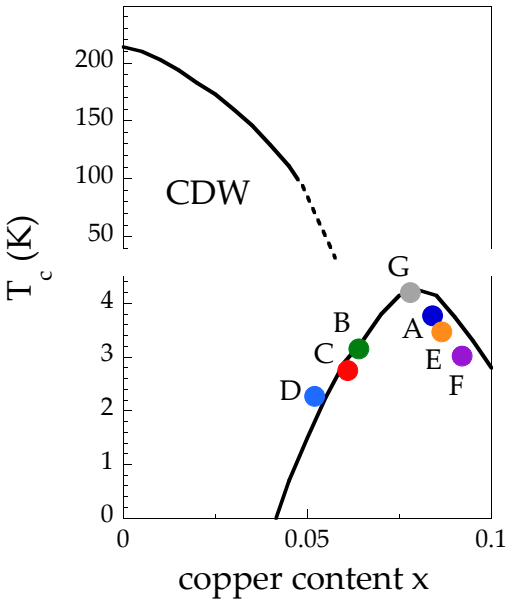

x	Label	T_c (K)
0.052	D	2.3
0.061	C	2.8
0.064	B	3.2
0.075	G	4.1
0.084	A	3.8
0.086	E	3.5
0.092	F	3.0

Figure 5: *Gauche* - Diagramme de phase de Cu_xTiSe_2 montrant des températures critiques de transition vers l'état supraconducteur T_c en fonction de la teneur en cuivre x pour les échantillons étudiés dans ce travail (cercles complets colorés) [13]. La ligne noire représente les résultats obtenus par Morosan *et al.* in [2]. *Droite* - Tableau résumant les valeurs de x et T_c obtenues pour tous les échantillons.

par Florence Lévy-Bertrand et Bastien Michon de l'Institut Néel à Grenoble.

La figure 6-*Gauche* montre l'image en microscope électronique à balayage (Scanning Electron Microscopy - SEM) de l'échantillon B de dimension × largeur × épaisseur = $250 \times 250 \times 50$ μm^3. La ligne rouge représente la ligne selon laquelle nous avons obtenu les profils de champ présentés en figure 6-*Droite* (pour $T = 1.6$ K, soit environ 50% de la température critique, l'échantillon a été déplacé trois fois le long de la ligne de sondes pour pouvoir obtenir le profil complet). Le centre de l'échantillon est situé à la position $X = 0$ et ses arêtes sont proches de $X = -3$ et $X = 3$. Pour les champs magnétiques les plus bas (voir les données pour 10 G en Fig.6-*Droite*), l'échantillon était dans l'état Meissner et aucun champ n'a été détecté mais pour $H_a > 17.5$ G, la figure montre que les vortex entrent et, et en l'absence de piégeage, se concentrent au centre pour former un profil en dôme dont l'amplitude croit avec le champ appliqué. La forme de ce profil magnétique nous indique directement l'endroit où les premiers vortex s'accumulent dans l'échantillon, et donc auquel il conviendra de mesurer le champ de pénétration H_p. Si au contraire, le piégeage avait été fort, les vortex seraient restés piégés proche des bords et, pour des champs appliqués de plus en plus élevés, les vortex se seraient piégés sur d'autres sites jusqu'à finalement atteindre progressivement le centre de l'échantillon créant un profil en forme de lettre "V". Il aurait alors été préférable de mesurer H_p proche des bords.

Le profil en forme de dôme de l'échantillon B indique donc que le piégeage dans cet échantillon est faible et que H_p doit être déterminé à partir des sondes de Hall situées proche du centre de l'échantillon. Néanmoins, le profil de champ obtenu lorsque H a été

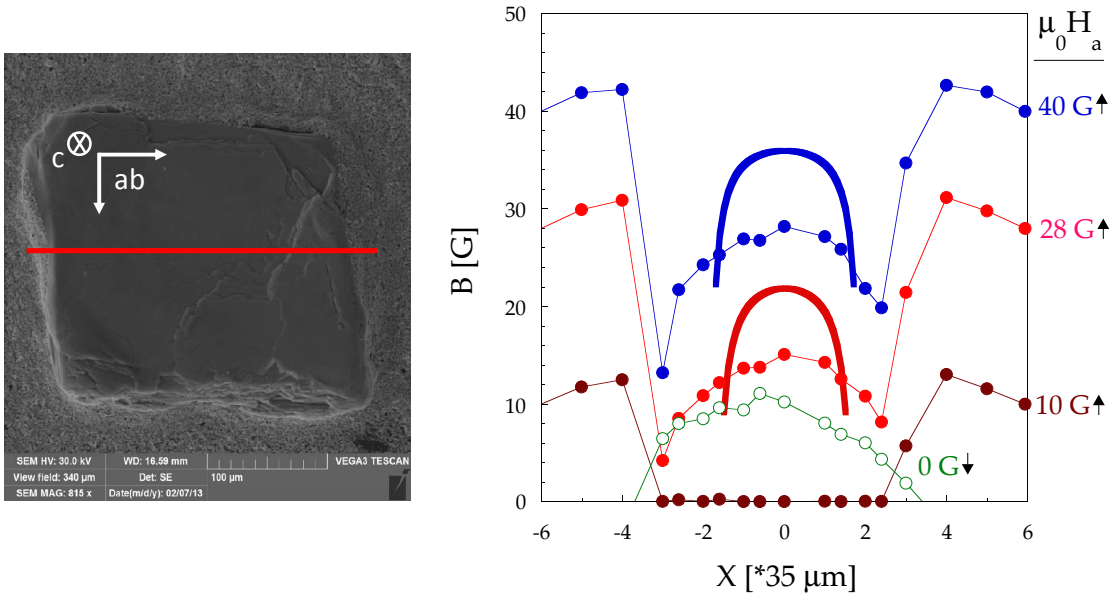

Figure 6: *Gauche* - Image SEM de l'échantillon B. La ligne rouge indique la ligne le long de laquelle les profils de champ magnétique ont été mesurés. *Droite* - Profils de champ magnétique $B(X)$ de $Cu_{0.064}TiSe_2$ (échantillon B). Les cercles pleins correspondent aux données mesurées en champ magnétique croissant et les cercles vides montrent les données obtenues lorsque le champ a été ramené à zéro [14]. Les lignes fines reliant les points sont des guides pour les yeux. et les lignes épaisses montrent les profils calculés à partir du modèle proposé par Zeldov *et. al* [15] en présence de barrières géométriques (sans piégeage).

ramené à 0 G (cercles vides en Fig.6-*Droite*) montre que certains vortex sont restés piégés dans l'échantillon et que le piégeage est donc non nul. La valeur rémanente de B au centre, de l'ordre de 10 G, correspond à une densité de courant critique $J_c \sim H/d \sim 650$ A/cm^2 (ou d est la demi-largeur de l'échantillon, soit 125 μm), ce qui est une valeur similaire à celle obtenue dans les monocristaux de haute qualité de MgB_2 [16] pour lesquels J_c est particulièrement faible.

En ce qui concerne les mesures en champ magnétique, il est important de prendre en compte les effets de désaimantation associés à la déformation des lignes du champ autour du supraconducteur. Pour des échantillons de section rectangulaire, comme c'est le cas ici, la déformation est plus significative sur les coins de l'échantillon. Le champ local à la surface y atteint la valeur critique H_{c1} en premier et les lignes de champ commencent donc à entrer dans le supraconducteur par ces coins. Pour un champ croissant, les vortex s'étendent alors de plus en plus loin des coins vers le centre de l'échantillon et la partie équatoriale. Lorsque les segments supérieures et inférieures des vortex se rencontrent à mi-hauteur, le premier vortex entier pénétré enfin dans l'échantillon. Cette valeur du champ appliqué, est appelée champ de pénétration H_p. Les coins de l'échantillon servent de barrières géométriques pour les vortex et Zeldov *et al.* [15] puis Brandt [17] ont étudié

ce cas en détail et ont montré que H_p peut être alors lié à H_{c1} selon :

$$H_{c1} = \frac{H_p}{\tanh\sqrt{\beta\dfrac{d}{2w}}}\,, \tag{1}$$

où $d/2w$ est le rapport épaisseur sur largeur de la section transversale de l'échantillon et le paramètre β est compris entre 0.36, si la troisième dimension de l'échantillon est beaucoup plus grande que d ou $2w$, et $\beta = 0.67$ si l'échantillon est un disque plat [17]. Négliger ces barrières géométriques entraîne une surestimation importante de H_{c1}, en particulier pour $d/2w << 1$.

La pénétration des vortex dans l'échantillon peut également être affectée par leur interaction attractive avec la surface. En effet, C. P. Bean et J. D. Livingston ont montré que la surface de l'échantillon elle-même pouvait créer une barrière empêchant l'entrée des vortex [18]. Le super-courant circule toujours tangentiellement à la surface et sa composante normale doit être nulle. Pour remplir cette condition pendant l'entrée du vortex, on peut alors imaginer qu'un vortex virtuel apparaît en dehors de l'échantillon avec une circulation opposée. En conséquence, le vortex réel est attiré par son image miroir et ne peut pas entrer dans l'échantillon. Plus la surface est lisse, plus l'image miroir est "claire", et plus forte sera cette barrière appelée barrière de Bean-Livingston (BLB). Si toutefois la rugosité de la surface est comparable à la longueur de pénétration λ, alors l'image est "floue" et la BLB devient non pertinente. Bean et Livingston ont montré que le vortex passe cette barrière de surface uniquement lorsque le champ magnétique atteint le champ critique thermodynamique H_c et le champ de pénétration H_p n'est donc plus relié dans ce cas à H_{c1} mais à H_c.

Il est donc indispensable de savoir si les BLB jouent un rôle important dans la pénétration du vortex ou si elles peuvent être négligées. Brandt *et al.* [19] ont montré que si la BLB est négligeable alors les vortex commencent par rentrer par les coins dès les faibles valeurs de H (comme discuté ci-dessus) mais que si ces BLB sont fortes, alors le champ magnétique ne peut entrer dans ces coins que lorsque H atteint H_c et comme $H_c >> H_{c1}$, les barrières géométriques sont alors non pertinentes et le vortex "saute" directement au centre de l'échantillon. La principale différence entre ces deux scénarios est donc que, dans le cas des barrière géométriques, le champ apparaît dans les coins avant que le vortex ne pénètre alors que cet "effet de coin" n'existe pas pour les BLB. Une étude détaillé des profils dans l'échantillon E ($x = 0.086$ et $T_c = 3.5$ K) nous a donné la réponse à cette question.

Sa longueur et sa largeur sont de 400×1000 μm^2, mais son épaisseur varie de ≈ 50 μm du côté gauche à ≈ 30 μm au bord droit de l'échantillon. Les profils de champ ont la encore été construits à partir de trois profils partiels (Fig.7-*Gauche*). Lorsque le champ dépasse H_p, un dôme, similaire à celui observé dans l'échantillon B, apparaît dans la distribution de champ $B(X)$. Cependant, dans ce cas, le maximum du dôme est légèrement décalé vers la droite par rapport au centre de l'échantillon (vers $X = 11$) du fait de la variation d'épaisseur (le côté droit de l'échantillon est légèrement plus fin que le côté gauche). La différence d'épaisseur conduit en effet à une distribution non uniforme des courants de Meissner et la position d'équilibre pour les vortex se déplace vers la partie droite. Les

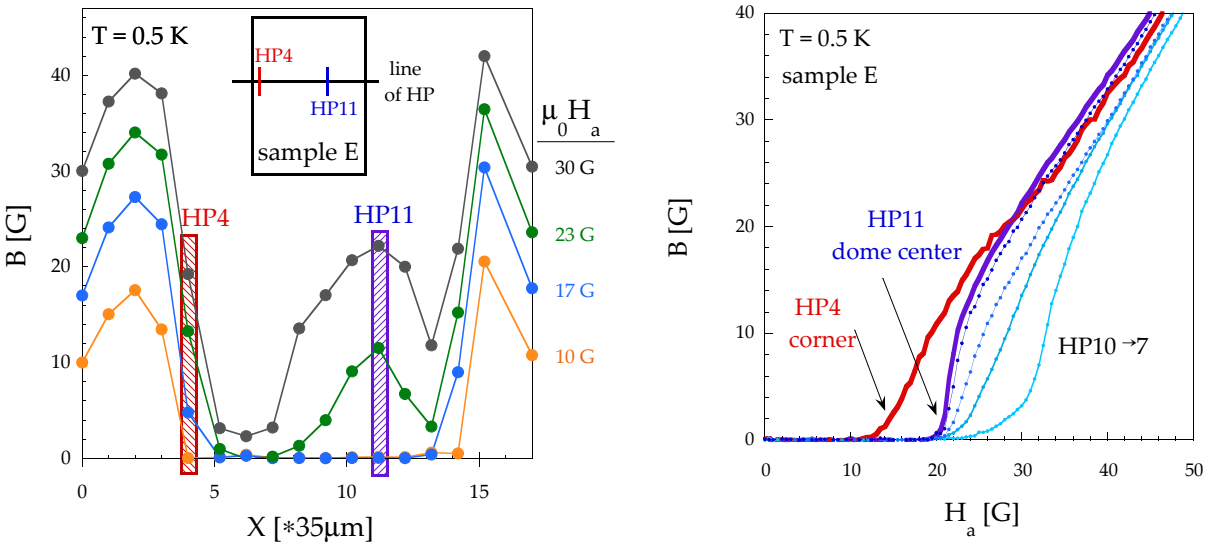

Figure 7: *Gauche* - Profils de champ magnétique mesurés à $T = 0.5$ K dans et autour de l'échantillon E pour un champ croissant. La boîte rouge et bleue marque l'évolution du signal B près du bord (HP4) et au centre du dôme (HP11). *Inser* - Croquis de la position de la sonde par rapport à l'échantillon. *Droite* - $B(H_a)$ dépendances mesurées par des sondes à différentes positions sous l'échantillon à $T = 0.5$ K. La ligne épaisse rouge a été mesurée près du bord de l'échantillon et une courbe bleue épaisse a été obtenue sur la sonde située au centre du dôme dans le profil de champ magnétique (voir les positions de la boîte rouge et bleue dans le panneau *Gauche*). [13]

profils de champ montrent également que sur les bords de l'échantillon (positions 4, 5 et 14) un champ B non nul apparaît avant la formation du dôme. Si nous comparons les courbes $B(H_a)$ obtenues sur les différentes sondes (Fig.7-*Droite*), nous voyons que $B(H_a)$ commence à augmenter au niveau de la sonde située près du bord de l'échantillon (HP4) bien plus tôt que sur les sondes situées au centre (proche du maximum du dôme, HP11 par exemple). Cette pénétration partielle du champ dans les coins prouve que les barrières de Bean-Livingston sont donc négligeables dans notre cas et le champ de pénétration H_p (déterminé au niveau de la sonde HP11) peut donc être relié au champ critique inférieur H_{c1} via l'équation 1. Des profils de champ ont été construits pour tous les monocristaux étudiés. Nous avons constaté que le piégeage était faible dans tous les échantillons et que le processus de pénétration du champ était dominé par les barrières géométriques dans tous les cas.

3.2 Dépendance en température de H_p

Les échantillons ont tout d'abord été refroidis en champ nul jusqu'à la température voulue. On augmente alors le champ extérieur jusqu'à observer l'augmentation rapide de B pour $H = H_p(T)$. Les dépendances en température de $H_p(T)$ mesurées sur six échantillons de dopage en cuivre différents sont comparées en Fig.8 (les valeurs de $H_p(T)$ ont été normalisées à $H_p(0)$ et la températures à T_c). Comme le montre la figure nous

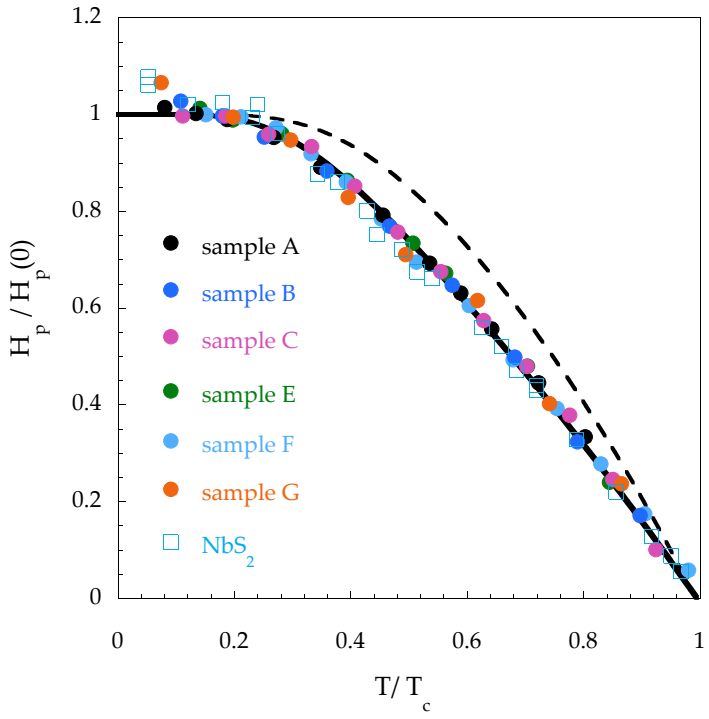

Figure 8: Dépendances en température de $H_p(T)/H_p(0)$ pour 6 échantillons de Cu_xTiSe_2 avec différents dtaux de dopage en cuivre. La courbe pointillée noire montre la courbe théorique pour $2\Delta/k_BT_c = 3.7$ (limite propre). Comme le montre la figure nos données ne suivent pas ce comportement mais sont mieux décrites avec un modèle à deux gaps avec $\Delta_1/k_BT_c \sim 2.4$ et $\Delta_2/k_BT_c \sim 3.7$. [13].

avons constaté que toutes les données suivent le même comportement sur toute la gamme de température, indépendamment du dopage en cuivre.

En présence de barrières géométriques, H_p peut être converti en H_{c1} via un facteur dépendant uniquement de la géométrie de l'échantillon (voir Eq.1), et les dépendances de température de H_p et H_{c1} sont donc identiques. Cette dépendances est très proche de celle de la densité superfluide ($H_{c1} \sim 1/\lambda^2$) et ne dépend donc que du rapport de couplage $2\Delta/k_BT_c$ [20]. La ligne pointillée en Fig.8 montre le comportement attendu pour la valeur de $2\Delta/k_BT_c \sim 3.7$ obtenue en chaleur spécifique. Comme on peut le voir, un décalage important est observé entre cette courbe théorique et les mesures et un bien meilleur accord entre théorie et données est obtenu pour un ajustement à deux gaps, l'un avec $2\Delta_1/k_BT_c = 3.7$ et le second $2\Delta_2/\kappa_BT_c = 2.4$.

La présence d'un petit gap a également été confirmée par des mesures de densité superfluide par TDO (Tunnel Diode Oscillator), effectuées par P. Rodière de Insitut Néel à Grenoble [13]. La technique TDO consiste à mesurer la fréquence de résonance d'un circuit entourant l'échantillon supraconducteur introduit dans une bobine d'inductance L, polarisée par un oscillateur à diode tunnel. La variation de la longueur de pénétration induit un décalage de la fréquence de résonance, qui peut être directement relié à λ (via une constante d'étalonnage). Ils ont obtenu une dépendance de $\lambda(T)$, qui peut être bien décrite par une loi exponentielle standard attestant de la présence d'un gap

supraconducteur complètement ouvert. Dans l'échantillon A, le rapport de couplage a été estimé à $2\Delta/k_BT_c \sim 2.4$ et des rapports similaires ont été obtenus pour les échantillons B ($2\Delta/k_BT_c \sim 2.5$), C ($2\Delta/k_BT_c \sim 2.8$) et G ($2\Delta/k_BT_c \sim 2.4$). Ces mesures TDO ont été effectuées uniquement à des températures très basses pour lesquelles seul le petit gap joue un rôle. Dans une certaine mesure, l'observation d'un petit gap est en accord avec les mesures de μSR de Zaberchik *et. al* [11] qui ont également indiqué la présence de 2 gaps, mais uniquement dans les échantillons sous-dopés. A l'inverse, nous avons observé que les deux gaps sont présents dans tous les échantillons étudiés de la région sous-dopée à la région sur-dopée.

Cependant, ces observations de petits gaps sont en contraste avec les résultats des mesures de chaleur spécifique effectuées sur nos échantillons par J. Kačmarčík *et al.* [9]. La principale différence entre les deux techniques est que le TDO sonde la surface de l'échantillon tandis que la calorimétrie AC mesure la capacité calorifique du volume. Cependant, cela ne peut pas expliquer la différence observée puisque les deux gaps ont également été observés par nos mesures à sonde de Hall pour lesquels la distribution du champ dans tout le volume a été prise en compte. Une autre raison pour ce désaccord pourrait être la sensibilité directionnelle des différentes techniques. En effet, les mesures magnétiques sont sensibles à la structure du gap dans le plan *ab* (pour $H\|c$) alors que chaleur spécifique sonde toutes les directions dans l'espace. Une autre différence notoire est que les mesures TDO et Hall sont plus sensibles aux bandes électroniques légères (comme $1/\lambda^2 \propto 1/m^*$), alors que la capacité calorifique est plus sensible aux bandes d'électrons lourds ($\gamma \propto m^*$). Pour assurer la cohérence entre ces mesures, la masse effective devrait changer de manière significative sur la surface de Fermi. Cependant, une étude de la surface de Fermi par des mesures de spectroscopie photoémission résolue en angle (Angle-Resolved Photoemission Spectroscopy - ARPES) ne valide pas cette hypothèse [21]. Curieusement, la dépendance en température de H_p est également très similaire à celle précédemment observée dans d'autres dichlorogénogènes $NbSe_2$ ou NbS_2. Cependant, dans ces systèmes, la présence de deux gaps a là été confirmée par toutes techniques expérimentales (mesures magnétiques, spectroscopie tunnel et chaleur spécifique) et a été reliée à la présence de deux feuillets différents sur la surface de Fermi.

3.3 Champs critiques

Pour chacun des échantillons étudiés, nous avons déterminé $H_p(0)$ en extrapolant la dépendance en température de H_p à 0 K et converti cette valeur en $H_{c1}(0)$ à partir du facteur géométrique approprié. Les corrections géométriques utilisées, les valeurs de H_p et H_{c1} ainsi que les valeurs de $H_{c2}(0)$ obtenues par J. Kačmarčík *et al.* à partir des mesures de chaleur spécifique ont été reportées dans le tableau 1.

Comme

$$\mu_0 H_{c2}(0) = \phi_0/(2\pi\xi(0)^2), \tag{2}$$

$$\mu_0 H_{c1(0)} = \frac{\phi_0}{4\pi\lambda(0)^2}[\ln\kappa + \alpha(\kappa)], \tag{3}$$

$$\alpha(\kappa) = 0.5 + \frac{1+\ln 2}{2\kappa - \sqrt{2} + 2}, \tag{4}$$

x	Label	T_c (K)	α_c	$\mu_0 H_p^c$ (0)[G]	$\mu_0 H_{c1}^c$ (0)[G]	$\mu_0 H_{c2}^c$ (0)[kG]	$\mu_0 H_c$ (0)[G]
0.052	D	2.3	-	-	-	5.0	-
0.061	C	2.8	4.3	14	60	5.5	335
0.064	B	3.2	4.5	18	80	7.0	429
0.075	G	4.1	2.3	50	115	9.5	631
0.084	A	3.8	3.8	30	114	7.5	546
0.086	E	3.5	5	21	105	5.5	457
0.092	F	3.0	3.1	30	95	4.5	392

Table 1

où $\kappa = \lambda(0)/\xi(0)$. Il est possible de déterminer $\lambda(0)$ et $\xi(0)$ à partir des champs critiques, puis de calculer le champ critique thermodynamique

$$H_c(0) = \phi_0/(\mu_0 2\pi\sqrt{2}\lambda(0)\xi(0)).$$

Comme par ailleurs, $H_c(0) \sim \Delta_0\sqrt{g(E_F)/\mu_0}$, où $g(E_F)$ est la densité des états au niveau de Fermi, il est possible de recalculer le coefficient de Sommerfeld de $\gamma = \pi^2 k_B^2\ g(E_F)/3$. On trouve pour l'échantillon A $\gamma \sim 6 \pm 2$ mJ mol^{-1}K^{-2} en bon accord avec la valeur obtenue directement par Morosan *et al.* à partir des mesures de chaleur spécifique pour un échantillon de dopage similaire ($\gamma \sim 4.5$ mJ mol^{-1}K^{-2} [2]). Cette cohérence thermodynamique montre que nos mesures donnent les bonnes valeurs de champs et donc des longueurs caractéristiques.

Comme la longueur de cohérence est directement reliée à H_{c2}, on s'attend à ce que :

$$H_{c2} \propto \frac{1}{{\xi_0}^2} \sim \frac{\Delta^2}{{v_F}^2} \sim T_c^2, \tag{5}$$

en limite propre et, les valeurs de λ et ξ étant affectées par l comme suit en limite sale :

$$\xi_0 = \frac{\xi^2}{0.731\ l} \tag{6}$$

et

$$\lambda_L = \lambda\sqrt{\frac{1.33\ l}{\xi_0}}, \tag{7}$$

(où λ_L est ici la profondeur de pénétration de London), on s'attend cette fois à ce que :

$$H_{c2} \propto \frac{1}{\xi_0 l} \sim \frac{\Delta}{v_F l} \sim T_c. \tag{8}$$

La figure 9-*Haut* montre la dépendance de $H_{c2}(T_c)$ des cristaux étudiés. Pour les échantillons sous-dopés, H_{c2} varie bien linéairement en T_c (ligne pointillée), alors que pour les échantillons sur-dopés, il suit une dépendance en T_c^2. Par conséquent, selon

les équations précédentes, les échantillons sous-dopés seraient en limite sale, tandis que les échantillons sur-dopés du dôme supraconducteur serait propres. λ_L et ξ_0 peuvent être obtenues à partir de mesures d'ARPES (et des calculs de D. Evtushinsky et S. Borisenko). Pour $x = 0.07$ on obtient $\lambda_L = 150 \pm 50$ nm et $\xi_0 = 40 \pm 8$ nm [22]. Nous n'avons pas

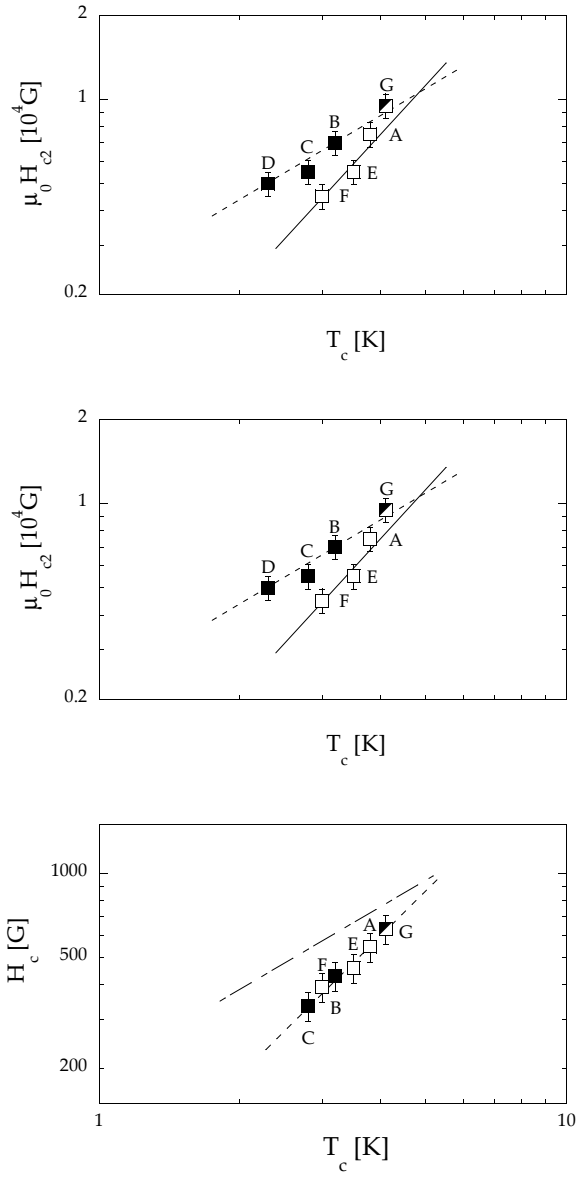

Figure 9: T_c dépendances du champ critique supérieur H_{c2} ($Haut$), du champ critique inférieure H_{c1} ($Milieu$) et du champ critique thermodynamique H_c (Bas) (à $T = 0$ et pour $H \| c$), pour les échantillons sous-dopés (carrés noirs pleins) et sur-dopés (carrés blancs) et l'échantillon G en dopage optimal. La ligne en pointillé dans le panneau $Haut$ correspond à une dépendance linéaire et la ligne continue à T_c^2. Dans le panneau Bas, la ligne pointillée indique la dépendance standard comme T_c, tandis que la ligne pointillée correspond à $T_c^{1.5}$ [13].

effectué de mesures pour cette concentration mais avons néanmoins pu interpoler nos données entre les échantillons B et G afin d'estimer $\lambda = 220$ nm et $\xi = 20$ nm. En utilisant les formules 6 et 7, nous pouvons calculer deux valeurs pour le libre parcours moyen et dans les deux cas on trouve $l = 13.5$ nm, ce qui confirme que cet échantillon sous-dopé est bien sale en accord avec notre analyse de la dépendance en T_c de H_{c2}.

Les figures 9-*Milieu* et *Bas* montrent elles les dépendances de $H_{c1}(0)$ et $H_c(0)$ en fonction de la température critique. En limite sale on s'attend dans ce cas à trouver :

$$H_{c1} \propto \frac{1}{\lambda} \sim \frac{l}{\lambda_L^2 \xi_0} \sim T_c, \tag{9}$$

tandis qu'en limite propre H_{c1} est indépendant de T_c. Finalement, comme $H_c \propto \sqrt{H_{c1} H_{c2}}$, on obtient $H_c \sim T_c$ dans les deux limites. Nos résultats indiquent cependant que $H_c \sim T_c^{1.5}$ (ligne pointillée dans la Fig.9-*Bas*). Une telle dépendance en T_c de H_c a été reportée dans les pnictides à base de fer [23] et suggère la présence d'un mécanisme de brisure de paires ou celle d'un point critique quantique. Les effets de brisure de paires peuvent être exclus, car ils conduiraient à un comportement en loi de puissance de T pour la profondeur de pénétration, en clair désaccord avec nos mesures.

4. Résultats II.

4.1 Effet de lock-in dans Cu_xTiSe_2

Dans ce chapitre nous allons analyser les résultats de magnétométrie à sonde de Hall obtenus pour un champ magnétique tourné d'un angle θ_H par rapport au plan ab de l'échantillon. La sonde de Hall détecte toujours uniquement le champ magnétique perpendiculaire à sa surface. Ainsi, si la sonde est située en dessous de l'échantillon parallèlement à ces plans ab, elle ne mesure que la composante de l'induction magnétique B parallèle à la direction c, $B^c = B \sin\theta_B$, où θ_B est l'orientation de B par rapport aux plans ab. La dépendance en champ magnétique de B^c mesurée pour différentes orientations θ_H du champ H est présentée en Fig.10-*Gauche* pour l'échantillon A, à titre d'exemple. Pour les champs magnétiques suffisamment élevés $\sin\theta_B = sin\theta_H$ et, $B^c/\sin\theta_H = B^c/\sin\theta_B = B$; toutes les courbes convergent alors vers la même courbe correspondant à $B = \mu_0 H_a$.

En comparant les signaux pour différents angles θ_H, on peut tout d'abord remarquer que pour les grandes valeurs de θ_H (par exemple $\theta_H = 57°$, courbe noire en Fig.10-*Gauche*) B^c augmente brusquement quand les vortex entrent l'échantillon à $H_a = H_p$. Mais, lorsque l'orientation du champ magnétique s'approche des plans ab ($\theta_H \to 0$), le comportement de $B^c(H_a)$ change radicalement. Quand H_a atteint le champ de pénétration H_p, on observe uniquement une faible augmentation du signal (contrairement à ce qui est observé aux angles plus élevés). Pour $H_a > H_p$, le signe B^c reste faible jusqu'à ce que le champ appliqué atteigne un deuxième champ caractéristique, appelé ici H_k, pour lequel une forte augmentation de B^c apparaît enfin. La valeur considérablement réduite de B^c observée pour $H_p < H_a < H_k$ suggère que les vortex entrant dans l'échantillon restent orientés parallèlement à ab et restent donc "verrouillés" dans cette direction jusqu'à ce que le champ atteigne H_k (on parle de lock-in). La valeur non nulle de B^c peut être

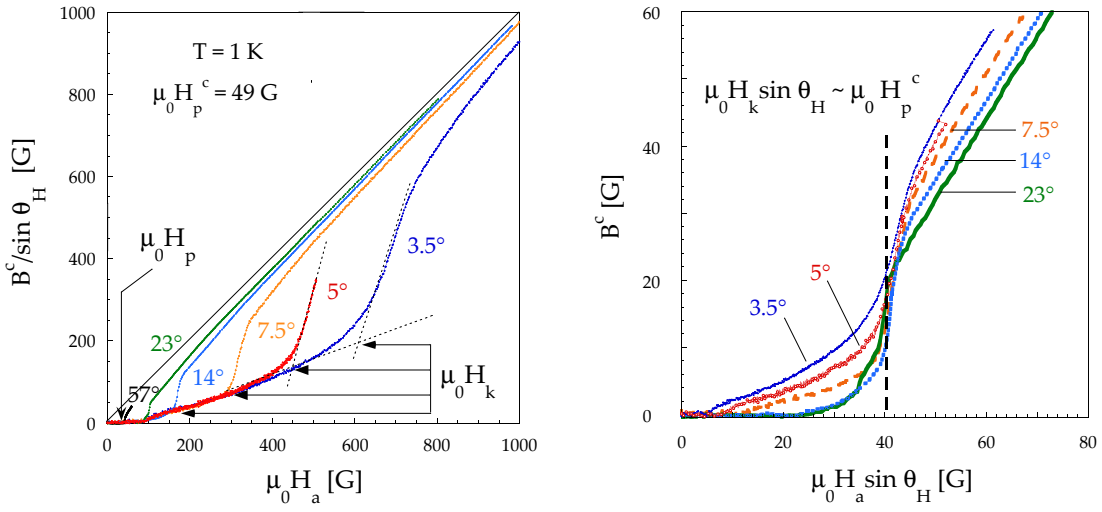

Figure 10: *Gauche* - Dépendances en champ magnétique de B^c, la composante de l'induction parallèle à la direction c (divisé ici par $\sin\theta_H$), mesuré pour différentes orientations du champ appliqué θ_H (compté à partir des plans ab, $T = 1$ K). H_p est détecté par la première augmentation du signal, tandis qu'à H_k, une deuxième augmentation plus nette de B^c peut être observée. *Droite* - Courbes du panneau *Guache* mis à l'échelle par $\sin\theta_H$ montrant que $\mu_0 H_k \sin\theta_H \sim 40$ G, proche de la valeur de $\mu_0 H_p^c$ dans cet échantillon. [24]

causée par la faible distance entre la sonde et l'échantillon. Il est également possible que tous les vortex ne soient pas "verrouillés" parallèlement aux plans et qu'une petite partie d'entre eux s'inclinent selon H. Lorsque le champ atteint H_k, les vortex se débloquent et le signal B^c augmente rapidement.

D'après [25], pour un angle donné, l'amplitude maximale du champ de lock-in H_L est donnée par le champ critique inférieur dans la direction c, de sorte que $H_L \sin\theta_H < H_{c1}^c$ i.e.

$$H_L = \lambda H_{c1}^c / \sin\theta_H, \tag{10}$$

où le paramètre λ définit la force du lock-in variant de 0 pour aucun effet à 1 pour l'effet le plus fort. Des mesures de couple magnétique dans YBCO ont ainsi été interprétées comme étant dues au lock-in [27] avec, dans ce cas, $\lambda \sim 0.5$. La figure 10-*Droite* montre les mêmes données que la figure 10-*Gauche* mais les axes horizontal et vertical ont ici été multipliés par $\sin\theta_H$ afin de montrer que H_k varie bien comme $1/\sin\theta_H$, comme prévu pour l'effet de lock-in [25]. On peut également noter que $\mu_0 H_k \sin\theta_H \sim 40$ G, soit une valeur très proche de $\mu_0 H_p^c$ montrant que l'effet de lock-in est extrêmement fort dans cet échantillon ($\lambda \sim 1$).

Pour analyser l'orientation θ_B des vortex, les deux composantes de B sont nécessaires. Comme le montre le schéma de la Fig.11-*Gauche*, B^c a été mesuré sur une sonde située sous l'échantillon et la composante B^{ab} a été obtenue à partir d'une sonde située sur le côté de l'échantillon (avec sa surface parallèle à la direction c). La figure 11-*Droite* montre les dépendances en champ magnétique de B^c et B^{ab} (divisées respectivement par $\sin\theta_B$ et

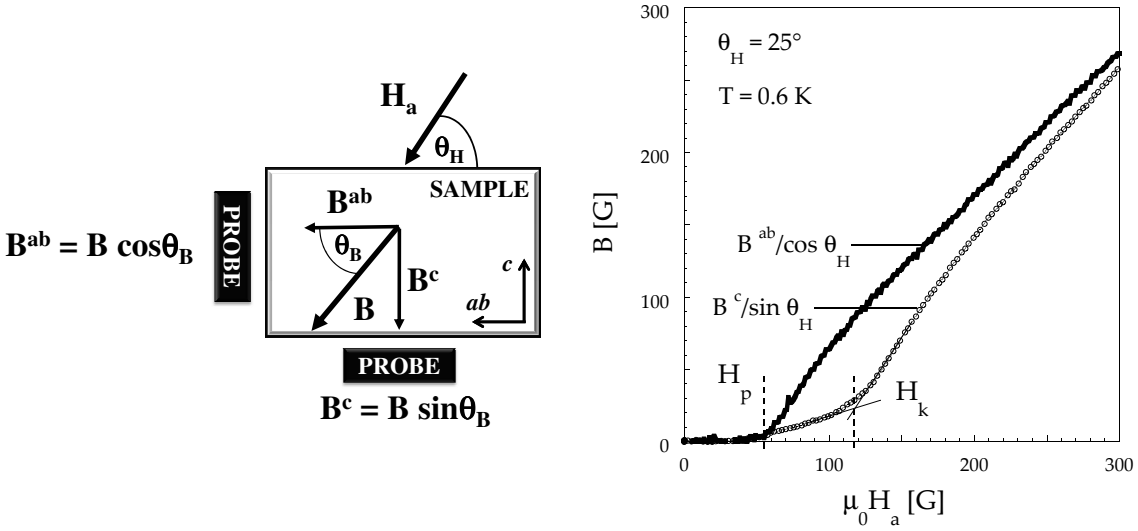

Figure 11: *Gauche* - Schéma du positionnement des sondes de Hall permettant de mesurer les deux composantes de l'induction magnétique B afin d'obtenir les informations sur l'orientation du vortex, θ_B. *Droite* - Dépendances en champ de $B^{ab}/\cos\theta_H$ et $B^c/\sin\theta_H$ pour $\theta_H = 25°$ (pour $T = 0.6$ K).

$\cos\theta_B$) obtenue dans l'échantillon G pour $\theta_H = 25°$. Il s'avère que dans cet échantillon, H_p ne dépend que très peu de θ_H car l'anisotropie de H_{c1} se trouve être totalement compensée par les effets géométriques. Si les vortex étaient alignés avec le champ appliqué, $\theta_B = \theta_H$, les deux courbes de la Fig.11-*Droite* seraient identiques car on aurait :

$$\frac{B^{ab}}{\cos\theta_H} = \frac{B\cos\theta_B}{\cos\theta_H} = B = \frac{B\sin\theta_B}{\sin\theta_H} = \frac{B^c}{\sin\theta_H}, \tag{11}$$

ce qui n'est clairement pas le cas. Alors que $B^{ab}/\cos\theta_H$ augmente nettement au-dessus de H_p, $B^c/\sin\theta_H$ reste faible. Cela montre clairement que les vortex qui entrent dans l'échantillon pour $H_a > H_p$ restent verrouillés le long des plans. En conséquence de quoi, une forte augmentation du signal est mesuré par la sonde perpendiculaire aux plans, alors que le signal reste beaucoup plus faible sur la sonde de Hall située sous l'échantillon.

En divisant ces deux dépendances, on peut alors obtenir des informations sur l'orientation des vortex : $(B^c/\sin\theta_H)/(B^{ab}/\cos\theta_H) = \tan\theta_B/\tan\theta_H$. La figure 12 montre les dépendances en champ de $\tan\theta_B(H_a)/\tan\theta_H$, pour certains angles du champ appliqué θ_H (aux températures indiquées). Le signal faible de B^c pour $H_a < H_k$ induit des erreurs importantes dans la dépendance de θ_B pour les faibles valeurs de H_a et nous ne présentons donc ici que les données pour $H_a > H_k$. Pour les champs les plus faibles, $\tan\theta_B/\tan\theta_H$ est faible et augmente lorsque les vortex se débloquent progressivement. Pour les champs magnétiques les plus élevés, ce rapport tend vers 1, indiquant que les vortex s'alignent progressivement avec le champ extérieur et $\theta_B \to \theta_H$. Pour $\theta_H \geq 70°$, θ_B est proche de θ_H sur toute la gamme de température étudiée, sans signe de lock-in.

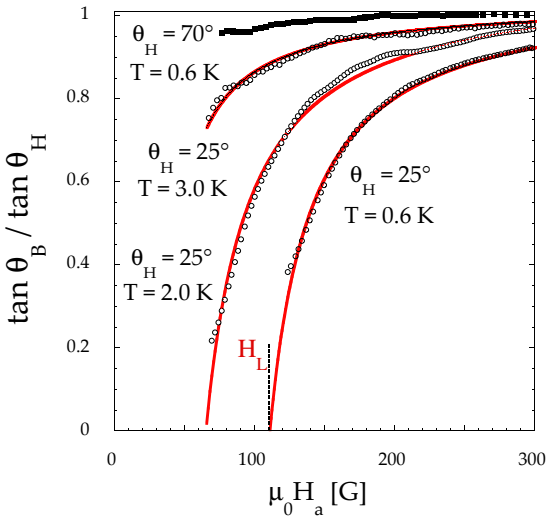

Figure 12: Dépendance en champ de l'orientation des vortex (θ_B) dans l'échantillon, pour les températures T indiquées et les orientations du champ appliqué θ_H. Les points noirs ouvert correspondent aux données mesurées au même $\theta_H = 25°$ mais pour différentes températures et les points pleins représentent les données à $\theta_H = 70°$. Les lignes rouges sont des ajustements au modèle décrit dans le texte [24].

4.2 Modèle Blatter modifié

La présence de lock-in dans Cu_xTiSe_2 est inattendue. Cet effet peut tout d'abord résulter d'un piégeage intrinsèque [26] dans les matériaux lamellaires pour lesquels des couches de phases normales et supraconductrices alternent. Ces composés présentent alors une anisotropie élevée, car la longueur de cohérence dans la direction c est faible par rapport à la distance interplans et les vortex peuvent se placer entre les couches supraconductrices. Ce n'est cependant pas le cas de Cu_xTiSe_2 pour lequel l'anisotropie est faible avec $\xi_c \sim 12$ nm et $d = 0.6$ nm, $\xi_c >> d$. On peut également exclure dans ce cas l'existence de deux réseaux de vortex croisés proposée par Sudbo *et al.* [28]. Cela nous amène à conclure qu'il doit exister une structure de piégeage supplémentaire, extrinsèque, parallèle aux plans ab, et au cœur de laquelle la supraconductivité serait au moins partiellement détruite. De telles structures ont été prises en compte dans le modèle de Blatter *et. al.* [29] décrit ci-dessous.

Nous avons étendu le modèle pour prendre en compte les spécificités de notre composé en considérant tout d'abord comme Blatter *et al.* le cas isotrope, mais avec une orientation arbitraire du champ i.e. au delà de l'approximation des petits angles utilisée dans [29]. Dans leur modèle, Blatter *et al.* commencent par calculer l'énergie d'un vortex qui adopterait une structure en escalier, afin de placer des parties de son cœur de longueur r dans le plan (voir le schéma de la Fig.13), car sa tension de ligne ε_l y est réduite de ε_P. Le gain en énergie du segment de vortex piégé est contre balancé par le coût en énergie dû à la déformation élastique du vortex et l'énergie totale est donnée par :

$$E(\theta_B, r) = r(\varepsilon_l - \varepsilon_P) + s\varepsilon_l - t\varepsilon_l, \tag{12}$$

où s et t sont les longueurs caractéristiques du schéma de la Fig.13. En minimisant

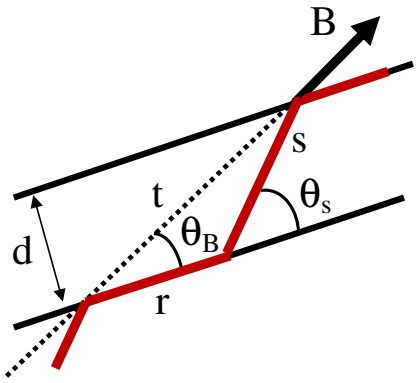

Figure 13: Schéma d'une ligne de vortex s'adaptant à la structure en couches dans laquelle la supraconductivité est partiellement détruite.

l'énergie par rapport à θ_B, on trouve :

$$r = \frac{d}{\tan\theta_B} - \frac{d}{\tan\theta_t}, \tag{13}$$

où

$$\tan\theta_t = \frac{\sqrt{2\varepsilon_l\varepsilon_P - \varepsilon_P^2}}{\varepsilon_l - \varepsilon_P}. \tag{14}$$

Et en insérant cette expression dans eq.12, on obtient alors la fonctionnelle suivante pour $E(\theta_B)$:

$$E(\theta_B) = \frac{d}{\tan\theta_B}(\varepsilon_l - \varepsilon_P) - \frac{d}{\sin\theta_B}\varepsilon_l + d\tan\theta_t(\varepsilon_l - \varepsilon_P). \tag{15}$$

En supposant enfin une densité faible mais finie de vortex dans le système égale à $B/(\phi_0 t)$, on obtient la densité d'énergie correspondante $E' = EB/(\phi_0 t)$. La densité totale de l'énergie de Gibbs du système comprend alors le champ magnétique à l'intérieur des vortex, l'énergie des super-courants, la déformation du vortex que l'on vient de calculer et l'énergie du champ magnétique appliqué, soit :

$$\begin{aligned} g = \frac{B^2}{8\pi} + \frac{\phi_0 B\varepsilon_l}{2(4\pi\lambda)^2}\ln\left[\frac{H_{c2}^c}{\varepsilon_l B}\right] + \\ -\frac{B}{\phi_0}(\varepsilon_l - \varepsilon_P)\sin\theta_B - \frac{B}{\phi_0}\varepsilon_l + \frac{B}{\phi_0}(\varepsilon_l - \varepsilon_P)\sin\theta_B\tan\theta_t + \\ -\frac{BH}{4\pi}\cos\left(\theta_B - \theta_H\right) . \end{aligned} \tag{16}$$

En minimisant g par rapport à θ_B, on trouve finalement la solution suivante pour la dépendance en champ de l'orientation des vortex :

$$\frac{\tan\theta_B}{\tan\theta_H} \approx \begin{cases} 0 & H < H_L \\ \dfrac{1 - \frac{H_L}{H}}{1 - \frac{H_L}{H}\frac{\tan\theta_H}{\tan\theta_t}} & H_L < H, \theta_H < \theta_t \quad (2) \\ 1 & \theta_t < \theta_H \end{cases} \tag{17}$$

où H_L est le champ de lock-in donné par :

$$H_L = \frac{4\pi}{\phi_0}\frac{\sqrt{2\varepsilon_l\varepsilon_P - \varepsilon_P^2}}{\sin\theta_H} \sim \frac{H_{c1}^c}{\sin\theta_H}\sqrt{2\frac{\varepsilon_p}{\varepsilon_l} - \frac{\varepsilon_p^2}{\varepsilon_l^2}} \tag{18}$$

Cette solution indique que, pour une orientation donnée du champ appliqué θ_H, on observe des vortex dans la configuration de lock-in ($\theta_B = 0°$) jusqu'à H_L. Pour les champs supérieurs, les vortex se "déverrouillent" et créent une structure en escalier jusqu'à ce que θ_B atteigne l'angle critique θ_t au delà duquel les vortex s'alignent alors sur le champ appliqué et $\theta_B = \theta_H$.

Examinons maintenant l'effet de l'anisotropie sur le modèle. Le gain en énergie sur la structure en escalier devient :

$$E(\theta_B, \Gamma, r(\theta_s)) = r(\theta_s)(\varepsilon_l(0,\Gamma) - \varepsilon_P) + s\varepsilon_l(\theta_s,\Gamma) - t\varepsilon_l(\theta_B,\Gamma), \tag{19}$$

où nous devons prendre en compte le fait que la tension de la ligne est

$$\varepsilon_l(\theta) = \varepsilon_0\sqrt{\sin^2\theta + \Gamma^2\cos^2\theta}$$

et $\varepsilon_0 = (\phi_0^2 \ln\kappa)/(4\pi\mu_0\lambda_{ab}^2)$ [28]. Trouver le minimum de la fonctionnelle par rapport à θ_B et la solution générale pour une anisotropie arbitraire n'est alors plus trivial. À partir de solutions numériques pour certaines valeurs de cet anisotropie Γ et $\varepsilon_R = \Gamma\varepsilon_P/\varepsilon_l$, nous avons constaté que dans tous les cas étudiés, E peut cependant être très bien décrit par une simple approximation parabolique :

$$E(\theta_B, \Gamma, \varepsilon_R) \approx -\frac{1}{2}\,\varepsilon_l(\Gamma,\varepsilon_R)(\theta_B - \theta_t(\Gamma,\varepsilon_R))^2, \tag{20}$$

où ε_l défini la courbure de la parabole et θ_t la position de son minimum. Cette approximation parabolique est également une excellente approximation du cas anisotrope (et correspond à la limite petits angles obtenue par Blatter *et al.* [29]), ce qui nous permet de prendre la même solution pour $\theta_B(H)$ que dans le cas isotrope (équation 17), mais avec H_L donné cette fois par :

$$H_L(\Gamma,\varepsilon_R) \approx \frac{H_{c1}^c}{\sin\theta_H}\cdot\mathcal{F}(\Gamma,\varepsilon_R). \tag{21}$$

H_L dépend désormais de l'anisotropie par le biais la fonction $\mathcal{F}$ (non analytique). Cependant, les solutions numériques montrent que la faible anisotropie de Cu_xTiSe_2 ($\Gamma = 1.7$) n'introduit qu'un changement mineur dans les valeurs de θ_t (environ $1° - 2°$) et $\mathcal{F}$ dépend principalement de ε_R.

Finalement il est nécessaire de prendre en compte les effets de déaimantation pour relier le champ appliqué au champ H à la surface de l'échantillon. Pour $\theta = 25°$, on a :

$$H_c = \alpha^c H_a \sin\theta_H - (\alpha^c - 1)B^c/\mu_0,$$

$$H_{ab} = \alpha^{ab} H_a \cos\theta_H - (\alpha^{ab} - 1)B^c/\mu_0,$$

$$H = \sqrt{H_{ab}^2 + H_c^2}, \tag{22}$$

où α^c est la correction géométrique obtenue à partir de l'équation 1 pour les barrières géométriques et $\alpha^{ab} \sim \alpha_c/(1+\alpha_c)$ (en négligeant ici la dépendance angulaire de α pour $\theta_H \sim 0$). Ce modèle a été utilisé pour "fitter" la dépendance en champ de l'orientation du vortex dans la Fig.12 (lignes rouges avec H_L et θ_t comme paramètres ajustables. Les paramètres obtenus ainsi que les valeurs de H_k et H_p ont été utilisés pour construire le diagramme de phase de la Fig.14. Ce diagramme fait apparaitre quatre structures de vortex différentes: l'état de Meissner, les vortex "verrouillés" dans les plans (lock-in), la structure en escalier et le réseau de vortex incliné (on peut noter que les valeurs de H_L obtenues à partir des ajustements sont en bon accord avec les H_k précédemment déterminés).

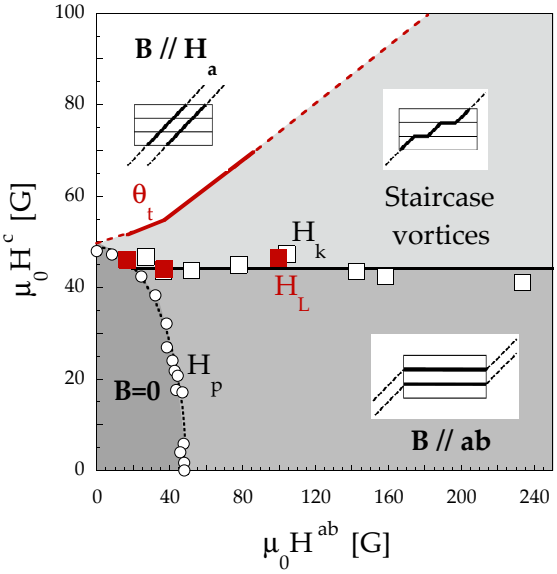

Figure 14: Diagramme de phase de la structure des vortex en fonction de l'orientation et de l'amplitude du champ dans $Cu_{0.075}TiSe_2$ (échantillon G) à $T = 0.6$ K. Les valeurs de H_k et H_p ont été obtenues directement à partir des courbes $B^c(\theta_H, H_a)$, et H_L et θ_t (rouge) sont les paramètres issues du modèle (voir texte et [24]).

4.3 Comparaison de l'effet de lock-in sur trois échantillons

L'effet de lock-in a été étudié sur trois échantillons : A, E et G, notés respectivement 1, 2 et 3 par la suite. Comme le montre la Fig.15, pour chacun d'eux $H_k(\theta_H)$ augmente rapidement pour $\theta \to 0°$, alors que $H_p(\theta_H)$ ne dépend que faiblement de θ. On peut remarquer que l'angle de seuil au-dessus duquel H_k ne peut plus être distingué de H_p, est beaucoup plus petit pour les échantillons 1 et 3 ($\sim 40°$) que pour échantillon 2 ($\sim 70°$).

Pour exclure toute influence de la géométrie sur l'effet de lock-in, il faut introduire les corrections géométriques appropriées pour H_p et H_k. Pour $H \| c$, $H_{c1}^c = \alpha_c H_p^c$, où α_c ne dépend que de la géométrie de l'échantillon (voir le tableau 1). Cependant, pour autres orientations du champ magnétique, la déformation des lignes de champ autour de

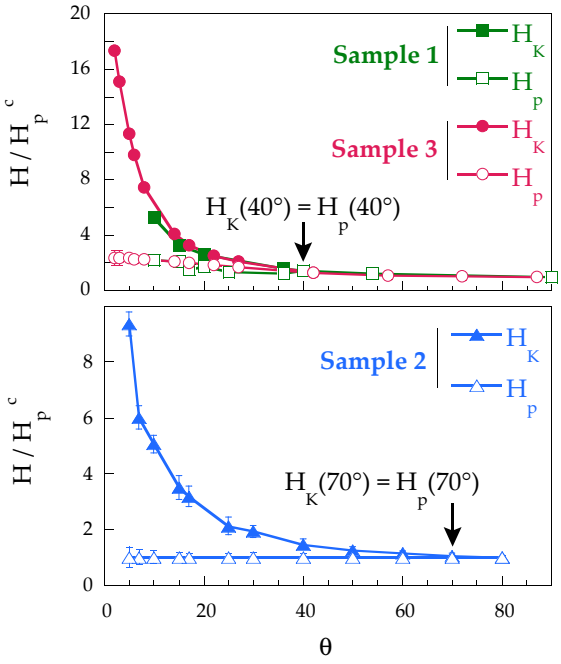

Figure 15: Dépendances angulaires de H_p et H_K obtenues pour trois monocristaux de Cu_xTiSe_2 pour $x = 0.06$ (échantillons 1), $x = 0.085$ (échantillons 3) et $x = 0.075$ (échantillons 2)

l'échantillon change. Pour $H\|ab$, cette déformation est par exemple faible et $H_{c1} \to H_p$. Il n'est pas possible de déterminer aisément les corrections géométriques pour chaque angle mais il a été montré dans MgB_2 [16], que α peut être raisonnablement bien estimé par une approximation elliptique :

$$\alpha(\theta_H) = \sqrt{(\alpha_c \sin\theta_H)^2 + (\frac{\alpha_c}{\alpha_c - 0.5}\cos\theta_H)^2}. \tag{23}$$

$$H_{c1}(\theta_H) = \alpha(\theta_H) H_p(\theta_H). \tag{24}$$

D'autre part, le champ critique pour le lock-in est limité uniquement par H_{c1}^c [25] : $H_L(\theta_H) = \alpha_c H_k(\theta_H)$ et comme cet effet ne peut être observé que si $H_k(\theta_H) > H_p(\theta_H)$ il ne sera visible que pour $\sin\theta_H < \lambda\ \Gamma_{H_{c1}}/\alpha_c$ avec $\Gamma_{H_{c1}} = H_{c1}^c/H_{c1}^{ab} \sim 2$ (en supposant ici que pour les faibles valeurs de θ, $\alpha(\theta_H) \sim 1$ et $H_{c1}(\theta_H) \approx H_{c1}^{ab}$). Comme $\lambda \sim 1$, on ne s'attend à l'observer que pour $\theta_H < 25°$ dans 1 et 3, et $< 65°$ dans l'échantillon 2, en bon accord avec les valeurs expérimentales (Fig.15). Notons que dans le cas d'un lock-in intrinsèque $\lambda \sim d/\xi$ soit ici ~ 0.02 [25] (comparable à $\lambda \sim 0.03$ pour les macles dans YBaCuO) et l'effet de lock-in n'aurait été observé que sur $\sim 1°$.

En introduisant ces facteurs géométriques, nous pouvons finalement convertir $H_k(\theta)$ et $H_p(\theta)$ en $H_L(\theta_H)$ et $H_{c1}(\theta_H)$. Comme le montre la Fig.16 (renormalisée à la valeur de H_{c1}^c) les trois courbes se superposent et la dépendance angulaire de H_{c1} peut directement être reliée à l'anisotropie du système $\Gamma_{H_{c1}} = H_{c1}^{ab}/H_{c1}^c \sim 2$ [9]. La dépendance angulaire de H_L suit quand à elle la courbe $1/\sin\theta_H$ (ligne noire en Fig.16) avec $\lambda \sim 1$ c.a.d. l'effet le plus fort que l'on puisse observer.

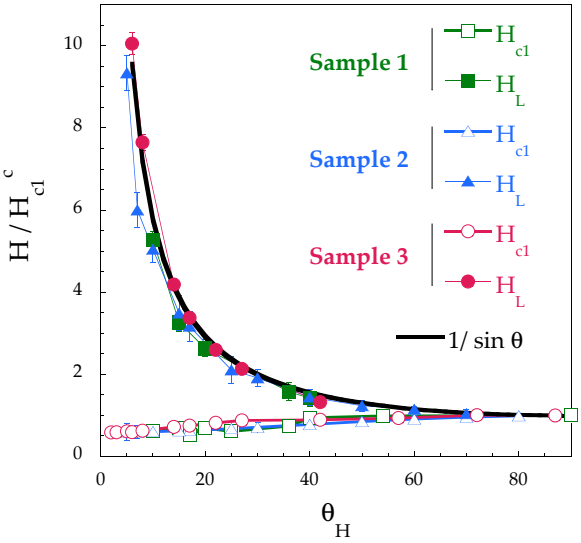

Figure 16: Dépendances angulaires de H_{c1} et H_L obtenues en multipliant $H_p(\theta)$ et $H_k(\theta)$ par les facteurs géométriques appropriés (voir texte). La ligne noire correspond à $1/\sin\theta$.

Pour finir, permettez-moi de commenter la dépendance en température de l'effet de lock-in. La Figure 17-*Gauche* montre les dépendances en champ de B^c pour $\theta_H = 15°$

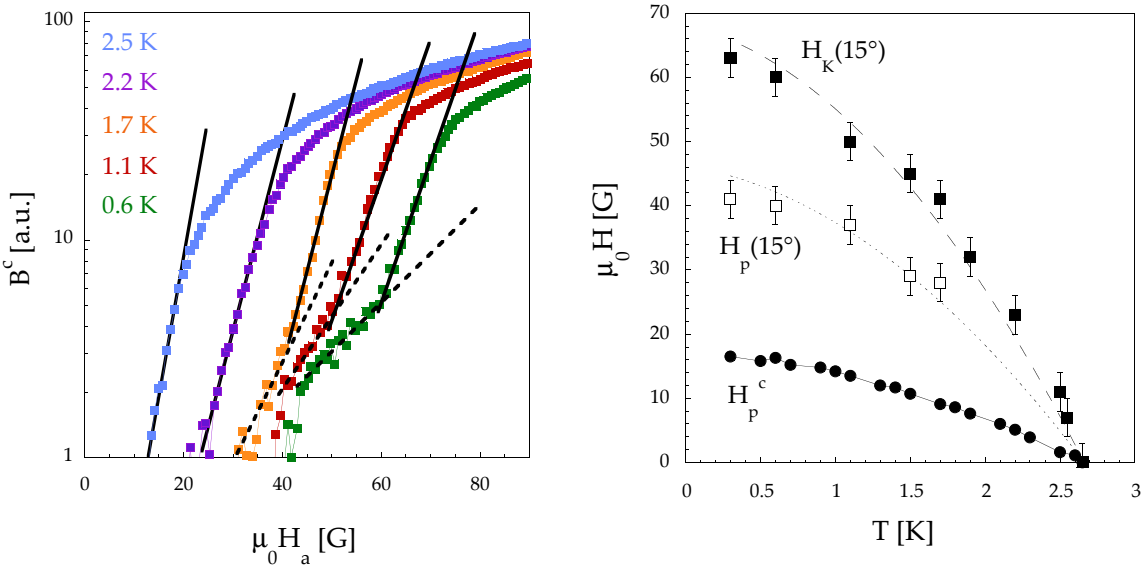

Figure 17: *Gauche* - Dépendance de champ de B^c à $\theta = 15°$ mesurée aux températures indiquées dans l'échantillon E. $H_k(15°)$ est le champ marquant l'augmentation rapide de B^c (lignes noires) et une faible augmentation de B^c est observée pour $H_a \geq H_p$ (lignes pointillées) pour $T \leq 1.7$ K. *Droite* - dépendance en température de H_p^c (cercles pleins), $H_p(15°)$ (carrés vides) et $H_k(15°)$ (carrés pleins). Les lignes pointillées et discontinues correspondent respectivement à $H_p^c/\alpha(15°)$ et $H_p^c/\sin 15°$.

(pour l'échantillon E à titre d'exemple). Comme indiqué par les lignes noires pointillées, la faible augmentation initiale de B^c pour $H_p(15°) \leq H_a$ n'est visible que pour $T \leq 1.7$ K et $H_p(15°)$ ne peut donc plus être mesuré au-dessus de cette température. La forte augmentation de B pour $H = H_k$ est quand à elle visible sur toute la gamme de température. La Figure 17-*Droite* montre les dépendances en température obtenues pour H_p^c, $H_p(15°)$ et $H_k(15°)$. La ligne pointillée a été construite en multipliant $H_p^c(T)$ par $\alpha^c/\alpha(15°)$ confirmant que $H_p^c\alpha^c/\alpha(15°) = H_{c1}^c/\alpha(15°) \sim H_p(15°)$ et la ligne discontinue correspond à $H_p^c/\sin(15°)$, montrant clairement que l'effet de lock-in persiste jusqu'à T_c avec $\lambda \sim 1$ sur toute la gamme de température.

Conclusion

Dans ce travail, nous avons étudié des monocristaux supraconducteurs de Cu_xTiSe_2 pour des dopages en cuivre x variant de $x = 0.052$ à $x = 0.092$, couvrant ainsi une grande partie du dôme supraconducteur dans le diagramme de phase. Des sondes de Hall miniatures ont été utilisées pour déterminer l'induction locale B dans le supraconducteur. À partir de la variation spatiale de B, nous avons reconstruit les profils magnétiques pour certaines valeurs du champ magnétique appliqué. La forme en dôme des profils a confirmé la grande qualité des échantillons étudiés et leur analyse a montré que les barrières géométriques jouent un rôle important dans la pénétration du flux. En effectuant des mesures à différentes températures, nous avons obtenu la dépendance en température de H_{c1}, qui s'est avérée être la même pour tous les échantillons étudiés. $H_{c1}(T)$ a été ajustée en utilisant un modèle à deux gaps pour la densité de superfluide avec $2\Delta_1/k_BT_c \sim 2.4$ et $2\Delta_2/k_BT_c \sim 3.7$. L'existence d'un petit gap énergétique a également été prouvée par des mesures TDO [13], mais ce petit gap n'a pas été observé dans les mesures de la chaleur spécifique.

Les mesures magnétiques locales effectuées pour différentes orientations du champ appliqué ont révélé la présence d'un effet de lock-in inattendu dans Cu_xTiSe_2. Un bon accord avec les données a été trouvé en supposant l'existence d'une structure de piegege en couches dans laquelle la supraconductivité est fortement affaiblie. Nous avons montré que cet effet de lock-in est extrêmement fort dans tous les échantillons mesurés. La nature de cette structure reste inconnue, mais elle pourrait être liée à l'observation récente de parois de domaines et/ou de défauts d'empilement dans la phase onde de densité de charge [4]. Leur périodicité ($\|c$) de l'ordre ~ 20 couches est en remarquable accord avec la longueur de cohérence ($\|c$). Une modulation importante du paramètre d'ordre dans la direction c pourrait également conduire à la présence de deux échelles d'énergie dans le système et à l'observation de deux gaps supraconducteurs. Kogar *et al.* ont observé que la phase incommensurable émerge à la même concentration en cuivre que la supraconductivité et persiste aux concentrations les plus élevées sans changement dans sa température critique. La force de l'effet de lock-in et la présence de deux gaps sont également indépendantes du dopage mais le lien direct entre ces effets reste à être démontré.

Résumé en Anglais

The subject of this work was a detailed study of superconducting Cu_xTiSe_2. Samples with various copper content x, from underdoped to overdoped regions of the phase diagram, were investigated by local Hall probe magnetometry. At first, we constructed the magnetic field profiles in the samples to determine when the first vortices penetrate into the sample. The observed dome-like shape of the profiles indicated that pinning is very small and that the vortex penetration is primarily governed by geometrical barriers, hence enabling us to determine the lower critical field, H_{c1}. A good agreement between theory and the $H_{c1}(T)$ data was obtained by using a model with two energy gaps, even though the origin of the smaller energy gap in Cu_xTiSe_2 cannot be related to its electronic structure. Combining those measurements with heat capacity measurements previously performed on these samples, we obtained a non trivial condensation energy. Moreover, measurements performed for various orientations of the magnetic field revealed the presence of a lock-in effect in Cu_xTiSe_2, when superconducting vortices are trapped along a layered structure even for tilted magnetic fields. The orientation of the vortices was experimentally determined and could be well described by a model considering the presence of an additional layered structure in which superconductivity is at least partially suppressed. The lock-in effect was analysed in three different samples and we have shown that the strength of the lock-in is independent of the copper doping, even though this effect can be masked by strong demagnetisation effects in very thin samples. The strength of this lock-in effect indicates that the superconductivity is strongly suppressed on certain layered structure. The nature of this "extrinsic" pinning structure is still unknown but might be related to the recent observation of charge density waves domain walls, which may induce strong variations of the superconducting order parameter.

References

[1] K. Rossnagel, J. Phys.: Condens. Matter **23**, 213001 (2011).

[2] E. Morosan et al., Nat. Phys. **2**, 544 (2006).

[3] H. Barath et al., Phys. Rev. Lett. **100**, 106402 (2008).

[4] A. Kogar et al., Phys. Rev. Lett. **118**, 027002 (2017).

[5] A. F. Kusmartseva et al., Phys. Rev. Lett. **103**, 236401 (2009).

[6] X. L. Wu et al., Science **243**, 1703 (1989).

[7] S. Y. Li et al., Phys. Rev. Lett. **99**, 107001 (2007).

[8] B. Batlogg, Phys. C **162-164**, 1393 (1989).

[9] J. Kačmarčík et al., Phys. Rev. B **88**, 020507(R) (2013).

[10] J. Kačmarčík et al., Phys. Rev. B **82**, 014518 (2010).

[11] M. Zaberchik et al., Phys. Rev. B **81**, 220505(R) (2010).

[12] C. S. Oglesby et al., J. Cryst. Growth **137**, 289 (1994).

[13] Z. Pribulová et al., Phys. Rev. B **95**, 174512 (2017).

[14] Z. Pribulová et al., Ac. Phys. Pol. A **126**, 370 (2014).

[15] E. Zeldov et al., Phys. Rev. Lett. **73**, 1428 (1994).

[16] L. Lyard et al., Phys. Rev. B **70**, 180504(R) (2004)

[17] E. H. Brandt, Phys. Rev. B **59**, 3369 (1999).

[18] C. P. Bean, J. D. Livingston, Phys. Rev. Lett. **12**, 14 (1964).

[19] E. H. Brandt et al., J. of Exp. and Theor. Phys. **117**, 439 (2013).

[20] M. Tinkham, Introduction to Superconductivity, second edition, Dover Publications, Inc., Mineola, New York, USA (2004), ISBN-13:978-0-486-43503-9 ISBN-10:0-486-43503-2

[21] J. F. Zhao et al., Phys. Rev. Lett. **99**, 146401 (2007).

[22] D. V. Evtushinsky et al., New J. Phys. **11**, 055069 (2009).

[23] P. Rodière et al., Phys. Rev. B **85**, 214506 (2012).

[24] Z. Medvecká et al., Phys. Rev. B **93**, 100501(R) (2016).

[25] D. Feinberg, A. M. Ettouhami, Int. J. Mod. Phys. B **7**, 2085 (1993).

[26] W. K. Kwok et al., Phys. Rev. Lett. **67**, 390 (1991).

[27] L. N. Bulaevskii, Phys. Rev. B **44**, 910 (1991); D. E. Farrell et al., Phys. Rev. Lett. **64**, 1573 (1990).

[28] A. Sudbøet al., Phys. Rev. Lett. **71**, 1451 (1993).

[29] G. Blatter et al., Rev. Mod. Phys. **66**, 1125 (1994).